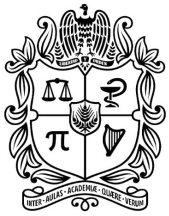

UNIVERSIDAD
NACIONAL
DE COLOMBIA

Prediction of the Occurrence of Flares in the Solar Cycle 24 from the Evolution of Magnetic Polarity Barycenters in Active Regions

Natalia Granados Hernández

Universidad Nacional de Colombia

Facultad de Ciencias, Observatorio Astronómico Nacional
Bogota, Colombia
2021

Prediction of the Occurrence of Flares in the Solar Cycle 24 from the Evolution of Magnetic Polarity Barycenters in Active Regions

Natalia Granados Hernández

Thesis presented as requirement to apply for Title of:
Master in Sciences - Astronomy

Director:
Prof. Santiago Vargas Domínguez, PhD
Co-Director:
Prof. Domenico Bonaccini Calia, PhD

Research branch:
Solar Astrophysics
Research Group:
Group of Solar Astrophysics (GoSA)

Universidad Nacional de Colombia
Facultad de Ciencias, Observatorio Astronómico Nacional
Bogota, Colombia
2021

To my mother, my partner, friend, confidant and greatest support.

Acknowledgements

I would like to thank the Group of Solar Astrophysics (GoSA)for welcoming me and showing me how exiting and awesome it is to study the Sun. Likewise, I would like to recognize the guidance of Professor Santiago Vargas for his advice in the execution of this work together with Professor Domenico Bonaccini Calia, who allowed me to participate in this big project of space weather, and the National Astronomical Observatory of Colombia for giving me the possibility to support and create novel investigations.

I am also grateful to the National University of Colombia, in which I was able to develop myself as a researcher and for allowing me to continue my scientific research.

Finally, I want to thank my family, my father Joselín Granados and my aunt Graciela Torres (Chela), who supported me all these years with my career and always without a doubt wished me the best, who without their help it would have not been possible to complete my studies, for this, I am completely grateful. Finally but not least important, the most special person in my life, my mother, María Beatriz Hernández, who shaped me as a person in life, my best friend, partner, greatest support and the most incredible, strong and spectacular person that I know.

Abstract

Title: Prediction of the Occurrence of Flares in the Solar Cycle 24 from the Evolution of Magnetic Polarity Barycenters in Active Regions.

Solar bipolar active regions and the processes that occur in them have been studied and analyzed for decades, generating many types of models and characterizations for the occurrence of different eruptive events that take place in the solar photosphere. Within these regions, the most characteristic explosive events are solar flares, which are big bursts of energy release, that depending on its magnitude, can represent negative effects on Earth and the technology developed by humans. For this reason, over the years, scientists have tried to predict the occurrence of these events. This work main target is the construction of a model that allows predicting the occurrence of solar flares, analyzing variables of importance in bipolar active regions such as their longitudinal magnetic field, areas of their umbra and the distance between the barycenters of the sunspots involved with opposite polarities. Variations on these parameters have demonstrated to be relevant for the occurrence of flaring events. Data processing is applied on HMI/SHARPs magnetograms and the method of the Weighted Horizontal Magnetic Gradient WG_M (Korsos 2015,2016) is used, finding a temporal relationship between the maximum of this variable (WG_M^{max}) and the moment of the occurrence of the flare (WG_M^{flare}), in a sample of 102 active regions of different GOES class.

Keywords: Space Weather, Bipolar Active Region, Flare, Prediction, Sunspots.

Resumen

Título: Predicción de la ocurrencia de fulguraciones en el ciclo solar 24 a partir de la evolución de los baricentros de polaridad magnética en regiones activas.

Las regiones activas solares bipolares y los procesos que ocurren en ellas han sido estudiados y analizados durante décadas, generando muchos tipos de modelos y caracterizaciones para la ocurrencia de diferentes eventos eruptivos que tienen lugar en la fotosfera solar. Dentro de estas regiones, los eventos explosivos más característicos son las fulguraciones solares, que son grandes ráfagas de liberación de energía, que dependiendo de su magnitud, pueden representar efectos negativos sobre la Tierra y la tecnología desarrollada por los humanos. Por esta razón, a lo largo de los años, los científicos han tratado de predecir la ocurrencia de estos eventos. El objetivo principal de este trabajo es la construcción de un modelo que permita predecir la ocurrencia de erupciones solares, analizando variables de importancia en regiones activas bipolares como su campo magnético longitudinal, áreas de su umbra y la distancia entre los baricentros de las manchas solares involucradas de polaridad opuesta. Las variaciones de estos parámetros han demostrado ser relevantes para la ocurrencia de eventos eruptivos. Se aplica procesamiento de datos sobre magnetogramas HMI/SHARPs y se utiliza el método del Gradiente Horizontal Magnético Ponderado WG_M (Korsos 2015,2016), encontrando una relación temporal entre el máximo de esta variable (WG_M^{max}) y su valor al momento de la ocurrencia de la fulguración (WG_M^{flare}), en una muestra de 102 regiones activas de diferente clase GOES.

Palabras Clave: Clima Espacial, Región Activa Bipolar, Fulguración, Predicción, Manchas Solares.

Contents

Introduction

The Sun is constantly emitting charged particles (solar wind). When these are directed towards the Earth, they enter the Earth's magnetosphere, defined as the region of space around the Earth that is connected by our magnetic field. Most of particles coming from the Sun are deflected around the edges of the Earth, but others are trapped in magnetic field lines and enter through the poles, since that is where these field lines converge. Among the effects that these particles can cause is the excitation of the gas molecules in the upper atmosphere (ionosphere) causing the Northern Lights or Southern Lights to shine. In particular, if the Sun sends out a large amount of charged particles in the form of an explosion, the emitted radiation could be detected around 8 minutes after the event, but the mass particles will reach approximately 1 to 3 days later and they will collide with the magnetosphere, stirring up the activity of the ionosphere.

Among the most studied explosive events that generate the aforementioned effects are **Solar Flares** and Coronal Mass Ejections (CME). GOES X class flares accompanied by the ejection of solar particles, can generate adversities on Earth such as geomagnetic storms, damage or shut down communications or global positioning satellites, endanger astronauts on space missions, and even shut down power grids. This is due to the interaction of the solar ejected particles with the ionosphere generating electrical currents of great intensity, the interruption of the propagation of radio waves (among others) or the vulnerability that space satellites or astronauts have when they are in outer space without some protection such as the Earth's atmosphere (Collins Petersen, 2017).

For this reason, this work aims to create a predictive model of solar flares, based on the development presented by Korsós et al. (2014) and Korsós et al. (2015), where the dependence of bipolar active regions in the formation of flares is used. The variables of interest to be obtained in this case are the umbra areas and magnitude of the mean magnetic field of the sunspots of opposite polarity and the distance from the barycenters of these magnetically opposite areas, adjusting the model to data obtained in Granados Hernández (2019).

This work is divided into four parts. Chapter 1 presents a brief description of some generalities of the Sun, such as its characteristics and some physical parameters (mass, radius, luminosity, among others) and fundamental concepts for the development of this work such as solar flares, solar magnetic field, bipolar active regions and space weather. The last part of this chapter focus on the SAMMNet (Solar Activity Magnetic Monitor), which is an international project of solar activity magnetic monitors whose purpose is to monitor the solar magnetic field to protect technology from events associated with space weather.

In Chapter 2 the data acquired from a solar observatory was used for the analysis of the active regions will be presented, in this case SDO (Solar Dynamics Observatory) and its instrument HMI (Helioseismic and Magnetic Imager), which provides magnetograms of active regions. The work includes details of the data acquisition and manipulation. In the last section, the

algorithm used to find the previously mentioned variables of interest is shown. With these variables, the *Weighted Horizontal Magnetic Gradient* WG_m was computed (Korsós et al., 2014, 2015), where the value of the longitudinal mean magnetic field of the umbras from the HMI magnetograms is used.

Later, in Chapter 3, the results obtained with the application of the algorithm are shown. Eventually, a relation of the order of magnitude of the maximum value for the weighted horizontal magnetic gradient WG_m^{max} associated with the flare is presented, in order to classify this value with the GOES class of the flares under analysis. A predictive model for the possibility of flare occurrence is therefore furnished. Additionally, the resulting time interval in which the flare occurred will be shown, as well as the estimation given by the method for the most consistent for a flaring event to occur.

Finally, in Chapter 4 the discussion and conclusions of this work are presented. The advantages and limitations that were found when analyzing these active solar regions are discussed and how to improve the data collection and corrections to be made to this model.

1. The Sun and its Activity

The Sun is the closest star to Earth and the central body of the solar system. It is composed mainly of Hydrogen (70%) and Helium (28%) and an approximate of 2% of heavy elements. It is estimated that at the center, its core has a density of 148.000 kg/m^3 and that it was formed approximately 4.6×10^9 years ago. Due to its proximity to our planet, it has been one of the most studied stars and we have determined different characteristics that can be of crucial influence on Earth (Cravens, 1997). At the beginning of this section we will see some important properties of this star and its internal structure. Then different phenomena that can be observed on the surface and solar atmosphere such as flares; active regions will be presented and the influence of the magnetic field on these processes will be highlighted. Subsequently, some events and consequences that the Sun has on Earth with the Space Weather are presented and finally the SAMNet international project whose purpose is the detection and forecast of phenomena or events associated with space weather is mentioned.

1.1 General aspects of the Sun and other stars

1.1.1 Properties

The source of information on the properties of stars is found from the analysis of their radiation. To understand the physics behind the stellar structure, birth and evolution, it is necessary to find certain quantities such as stellar mass, composition, magnetic field, stellar diameter, among others. Definitions of some of these quantities are mentioned below:

- **Parallax and Stellar Distance:** The stellar distance can be found by determining the parallax, which is the angle subtended by 1 astronomical unit (AU) at the distance d of the star from the Sun (Figure 1.1). Taking into account that the Earth annually orbits the Sun, the change in the observer's position causes an annual shift in the measurement of the position of the star, generating an ellipse in the sky that reflects the size and orientation of the Earth's orbit as it would be perceived from the star. The size of this ellipse is inversely proportional to the distance. The unit of distance parsec (pc), by convention, is defined as the distance in which the parallax of the star is one arc second (arcsec), that is $d = \pi^{-1}$ (Murdin, 2001, Parallaxes).
- **Stellar Diameter:** The diameter of a star varies from tens of kilometers as Neutron Stars and to hundreds of millions of kilometers as Supergiant Stars. Usually the size of the stars is expressed in terms of the solar radius ($R_\odot$). It can be measured directly if its angular diameter and distance from Earth are known, however the angular diameter is a more complex measurement due to the long distances involved. Other methods to find the size of stars are by interferometry, the star's is eclipsed by the Moon or indirectly if they are members of an eclipsing binary system (Moore, 2005, Stellar Diameter).

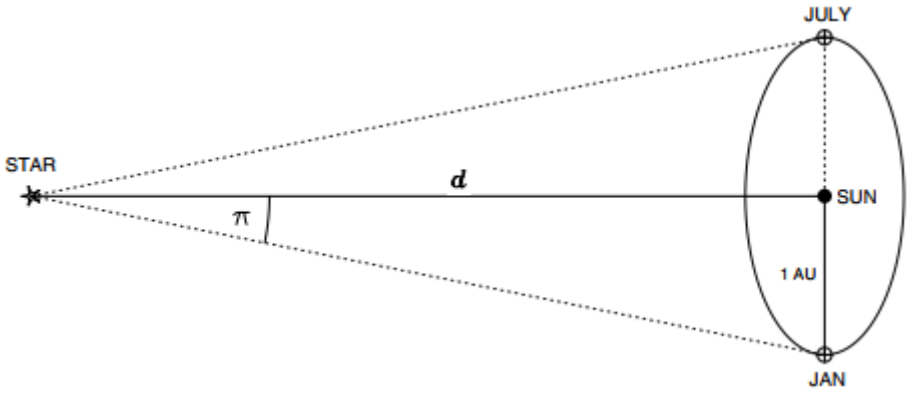

Figure 1.1: Scheme of the parallax π of a star at a distance d. Taken and edited from (Murdin, 2001, Figure 1)

- **Stellar Mass:** Its generally expressed in terms of the solar mass ($M_\odot$) and it is an important quantity to understand the evolution of the star and to determine its structure and life. They can vary from around 0.08 solar masses to around 150 of these (Moore, 2005, Stellar Mass).

1.1.2 Hetzprung-Russell Diagram and Evolution of the Sun

The Hetzprung-Russell Diagram (HRD) plots the temperature of a star versus its brightness. In the HRD the hottest stars are located on the left (blue stars are hotter than red stars) and therefore the temperature decreases towards the right of the diagram (Hanslmeier, 2008). Brightness is defined from *magnitudes*. The smaller the magnitude value, the brighter the star will be (it can include negative values). The less bright stars have magnitude $+6^m$, and as the brightness increases the magnitude decreases, including negative values, as in the case of Venus that has magnitude $-4.^m5$ or the Sun that has $-26.^m5$. Because these apparent magnitudes (m) depend on the star's intrinsic distance and luminosity, it is necessary to create a new definition, the *Absolute Magnitude* (M), which is the magnitude that a star has if viewed from a distance of 10 pc. In the HRD, instead of luminosity, the absolute magnitude can be used, where its relationship with the apparent magnitude is the following:

$$m - M = 5\log(r) - 5 \tag{1.1}$$

where r is the distance of the object in pc.

To find the temperature of a star, it can be considered as a *black body*, which is defined as an object that absorbs completely in all wavelengths. Radiation from a black body at a given temperature can be found with Planck's Law:

$$I_\nu = B_\nu = \frac{2h\nu^3}{c^2}\frac{1}{\exp(h\nu/k_BT) - 1} \tag{1.2}$$

where I_ν is the intensity of radiation at a frequency ν, and h, k_B and c are Planck's constant, Boltzmann's constant and the speed of light successively. If we now integrate this equation over all frequencies (wavelengths) we will obtain the total outgoing radiation flux emitted from the unit surface of a black body at temperature T, this is the Stefan-Boltzmann Law:

$$F = \int_0^\infty B_\lambda d\lambda = \sigma T^4 \tag{1.3}$$

where σ is the Boltzman constant. In the case of a star, for example the Sun, the emitted flux is given by the ratio of its Luminosity $L_\odot$ times the surface area, that is:

$$F_\odot = \frac{L_\odot}{4\pi R_\odot^2} \tag{1.4}$$

Therefore, the Stefan-Boltzmann Law allows us to find a specific temperature called **Effective Temperature** T_e:

$$F = \sigma T_e^4 = \frac{L_\odot}{4\pi R_\odot^2} \quad \rightarrow \quad L_\odot = 4\pi R_\odot^2 \sigma T_e \quad \rightarrow \quad T_e = \sqrt[4]{\frac{L_\odot}{4\pi R_\odot^2 \sigma}} \tag{1.5}$$

which in the case of the Sun is approximately 5778K (Severino, 2017).

The maximum intensity of radiation can be found by deriving Planck's Law respect to λ and setting it equal to zero, thus also finding the maximum wavelength:

$$T\lambda_{max} = 2.9 \times 10^{-3}\text{mK} \tag{1.6}$$

The previous equation is called Wien's Law and the associated temperature is the Wien Temperature, this is, the temperature found from the difference in intensity between two wavelengths or color temperature. To define color, the frequently used system is the UBV, which has three bands located at Ultraviolet (U), Blue (B) and Visual (V) to measure intensity I_ν. The color of the stars is obtained by comparing the magnitude through one filter with another (for example red with blue) where the magnitude is:

$$\text{Magnitud} = \text{const} - 2.5\log(I_\nu) \tag{1.7}$$

therefore temperature can also be found by color indices. If B-V is found, the following will be obtained:

- Positive values for cold stars since these are brighter in the visible (lower value in V) than in blue (higher value in B).
- Negative values for hot stars since they are brighter in the blue than in the visible.

Stellar Evolution and Evolution of the Sun

From Figure 1.2 it can be seen that:

- Main Sequence Stars: Most are located on the diagonal from the upper left (hot) to the lower right (cold) corner.
- Supergiants and Giants: They are similar in temperature to the main sequence, but are much larger and brighter.
- Dwarfs and White Dwarfs: They are weak but very hot objects, for this reason they must also be smaller and more compact (about 1/100 the size of the Sun).

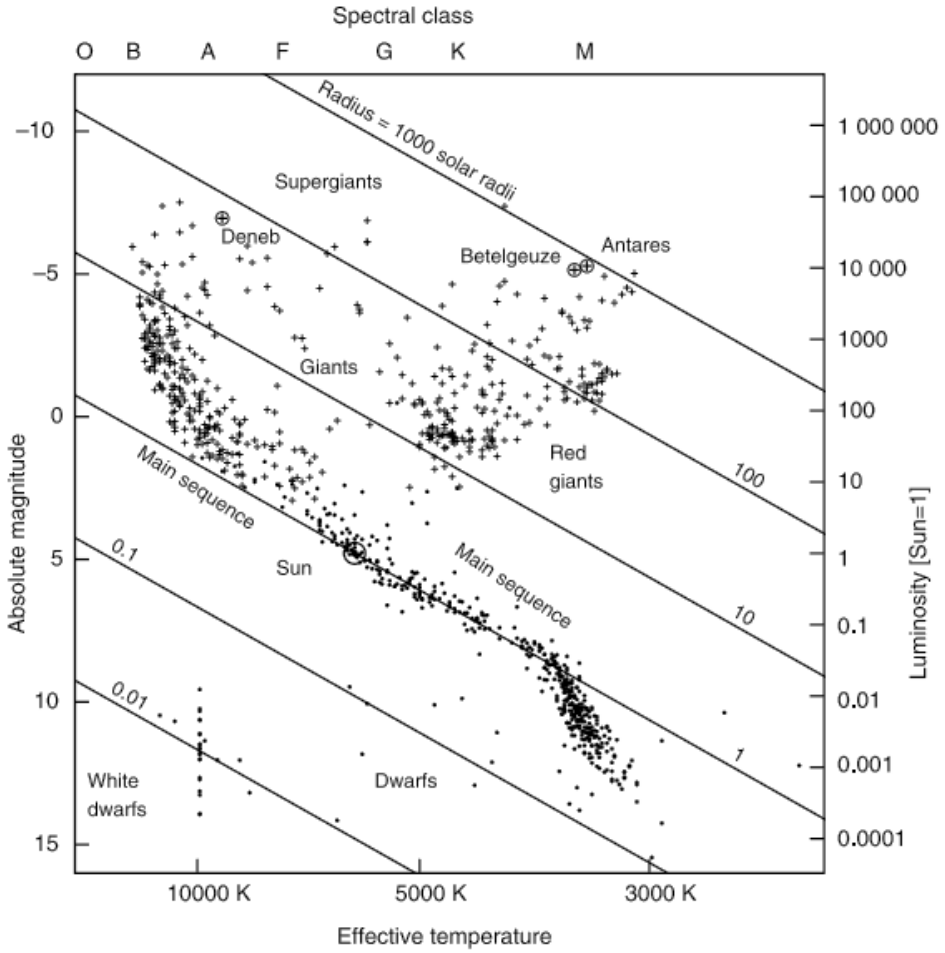

Figure 1.2: Taken and modified from (Karttunen et al., 2017, Fig. 9.8). HRD Diagram or Color-Magnitude Diagram. The horizontal coordinate can be either the *Intrinsic Color* obtained from observations or the *Spectral Class*. In theoretical studies the *Effective Temperature* is used. The vertical axis gives the value of the *Absolute Magnitude*

It is also observed that most stars are in the main sequence, this because it is the longest phase in stellar evolution. To understand it better, the case of the evolution of the Sun can be analyzed:

1. Pre-main sequence evolution: Before reaching the main sequence, the Sun was formed from protostellar gas and dust clouds, called the T Tauri phase.
2. In the main sequence the Sun stays around 10^{10} years slowly changing, where H is transformed into He by nuclear fusion.
3. The Sun evolves into a Red Giant, where it will expand in such a way that the Earth will be part of its atmosphere. This expansion will begin when all the H is transformed to He in its core, then a burning layer of H will supply the energy. It will stay in this form for about 10^8 years and will expand beyond Earth's orbit.
4. The Sun will eventually turn into a white dwarf which will slowly cool down.

The Sun during its evolution changes its radius drastically. Using the value of the radius that is known today, it is estimated that its radius changed as follows:

$$1R_{\odot}(\text{present Sun}) \rightarrow\sim 10^4 R_{\odot}(\text{red giant}) \rightarrow\sim R_{\odot}(\text{white dwarf})$$

Spectral class

Taking into account their spectrum, the stars can be classified in the following sequence: OBAFGKM (Table 1.1), where the O stars are hotter than the M. As seen in the equation 1.5, the Luminosity depends on the temperature and radius of the star, so for example for a star K, this can be a dwarf or a giant of the main sequence, therefore it was necessary to create classes of luminosity:

- Class I: brighter supergiants
- Class II: less brighter supergiants
- Class III: Normal giants
- Class IV: Subgiants
- Class V: Main sequence

With the above it can be understood that the spectral classification of the Sun is **G2V**.

O	ionized He, ionized metals
B	neutral He, H stronger
A	Balmer lines of H dominate
F	H becomes weaker, neutral and singly ionized metals
G	singly ionized Ca, H weaker, neutral metals
K	neutral metals molecular bands appear
M	TiO, neutral metals
R,N	CN, CH, neutral metals
S	Zirconium oxide, neutral metals

Table 1.1: Spectral classification of stars

Spectral Type	O	B0	A0	F0	G0	K0	M0	M5
T_e [K]	50000	25000	11000	7600	6000	5100	3600	3000

Table 1.2: Effective Temperature as a function of spectral type

1.1.3 Basic Properties of the Sun

From the previous section it was already mentioned that the Sun is a G2V-type star. The mass of the Sun is:

$$M_{\odot} = 1.99 \times 10^{30}\text{kg} \tag{1.8}$$

To find it, Kepler's third Law can be applied if the distance is known:

$$\frac{a^3}{P^2} = \frac{G}{4\pi^2}(M_1 + M_2) \tag{1.9}$$

where $a = 50 \times 10^6$ km is the Earth-Sun distance, $P = 1$ year the period of revolution of the Earth around the Sun, M_1 the mass of the Earth and M_2 the mass of the Sun. In this case we can assume that $M_1 << M_2$ therefore $M_1 + M_2 \sim M_2$ and with this we find the mass (Hanslmeier, 2008).

If the distance (1AU) and the angular diameter of the Sun are known, the radius can be found:

$$R_\odot = 6.96 \times 10^8 \text{m} \tag{1.10}$$

Taking into account that the size of the Sun is smaller than 1 AU, the angle under which we see it can be found with the ratio of its diameter and this distance, that is:

$$\alpha_\odot = \frac{2R_\odot}{\text{AU}} \quad \Rightarrow \quad R_\odot = \frac{\text{AU} \cdot \alpha_\odot}{2} \tag{1.11}$$

where $\alpha_\odot$ is the angular diameter in radians (Severino, 2017). If the mass and radius of the Sun are known, the mean density can be found:

$$\bar{\rho} = 1.4 \text{g/cm}^3 \tag{1.12}$$

The gravitational acceleration is given by:

$$g = \frac{GM_\odot}{R_\odot^2} = 274 \text{m/s}^2 \tag{1.13}$$

where G is the gravitational constant. The luminosity and effective temperature are:

$$L_\odot = 3.83 \times 10^{26} \text{W} \qquad T_{e\odot} = 5778 \text{K} \tag{1.14}$$

1.1.4 Structure of the Sun and Energy Transport

The Sun is composed mainly of Hydrogen (approximately 70% of its mass) and Helium (approximately 28%), and has a small proportion of heavy elements (approximately 2%) (Murdin, 2001, Sun).

It is estimated that the **Core** of the Sun has an approximate diameter of 200 000 km and a maximum density of 148 000kg/m $^{-3}$, that is, almost 30% of the Sun's mass is contained in just 3% of its volume. The temperature in this region is around 15 000 000 K, and the Hydrogen nuclei fuse together to generate Helium nuclei in a proton proton (p-p) type reaction chain. The energy released per second from the 4.4×10^9 kg of mass lost in this reaction is radiated through the **Radiative Zone**, a zone of approximately 200 000 km where the temperature has dropped to approximately 1000 000 K, and then the convection begins. The **Convection Zone** extends to the surface of the Sun, below the **Photosphere**, the latter is a layer several kilometers wide and represents the boundary between the atmosphere and the solar interior.

The temperature of the photosphere drops to around 6000 K at its base to 4000 K in its minimum temperature where it joins together with the **Chromosphere**. The chromosphere is composed of gases that span around thousands of kilometers wide where the temperature increases by about 50 000 K due to the mechanical dissipation process, while the density decreases dramatically towards the outside of the Sun. It is a region where it can be found events such as

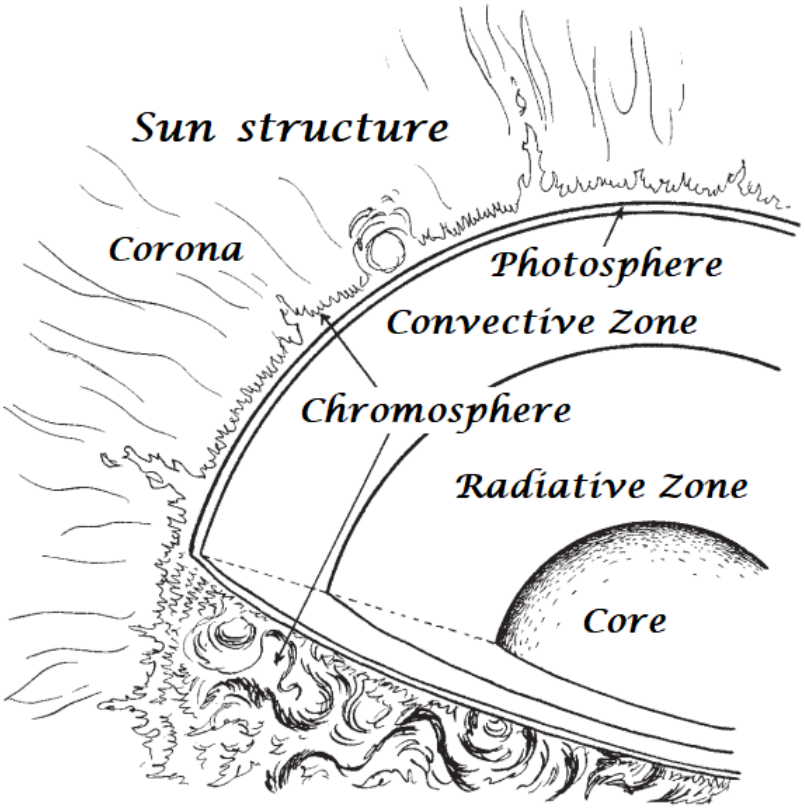

Figure 1.3: Diagram of the solar structure showing the layers that make up the interior and atmosphere of the Sun. Taken and edited from (Garfinkle and Garfinkle, 2008, Figure 4)

prominences that have high density and low temperatures compared to their surroundings. Short duration explosive events are also generated, called **Flares**. Sunspots, most prominences or filaments and flares constitute active regions, areas where solar activity is evident.

Above the chromosphere is the **Transition Region**, a few kilometers thick, where the temperature rises again to around 500 000 K. After this region is the **Corona**, which reaches temperatures of up to 2000 000 K at an elevation of about 75 000 and extending for millions of kilometers into the interplanetary medium, where the solar wind carries a stream of particles deep into the solar system.

1.2 The Active Sun

1.2.1 Sunspots

Discovery of sunspots

Solar spots can be observed with the naked eye (safely using solar filters), looking at the Sun in a short period of time and preferably when it is on the horizon in its lowest part so that its radiation is less intense due to the fact that the path that the light travels in the Earth's atmosphere is greater and its intensity decreases. This was first reported by Chinese astronomers who studied the Sun in this way for around 2000 years. At the begining of the XVII century, sunspots were observed for the first time with a telescope; an achievement attributed to four people: Galileo Galilei (Italy), Johann Goldsmid (Holland), Christoph Scheiner (Germany) and

Thomas Harriot (England). The first post on this topic was by Goldsmit, who argued that the Sun should have a rotation due to the movement of sunspots through the solar disk. Being a Jesuit, he initially thought that his telescope had some defect, but when confirming it, he could not publish it openly since his ecclesiastical superiors did not allow it. However, Christoph Scheiner, announced his discovery in three anonymous letters to a friend of Galileo Galilei, and he replied in three letters in 1612 that he had discovered these sunspots, this being the subject of discussion between the two. Nonetheless the observation from Thomas Harriot seems to be the very first one using a telescope, made on December 3, 1610, though his observations were not widely known for almost two centuries.

After the publication of Scheiner, there was no great interest in sunspots for a time, in part because from 1640 to 1705, a period of time known as the *Maunder Minimum*, occurred, in which there was a great reduction in the appearance of sunspots, practically disappearing from the solar surface.

Later would come another great discovery by Schwabe (Germany) who in 1826 bought a telescope to search for planets close to the orbit of Mercury, but then he recorded sequential appearances of sunspots for 43 years, noting a periodicity of occurrence every 10 years. In 1851, he published on the average 11-year periodicity of sunspots (Hanslmeier, 2008, Chapter 4.2.4).

General characteristics

Sunspots are the oldest detected manifestation of solar activity. They are regions on the solar surface that have a strong magnetic field of about 0.1 T, that is, about 1000 times larger than the average field in the photosphere. These look dark because they have less temperature compared to their surroundings as a result of the action of the magnetic field that inhibits convection and reduces the movement and temperature of the plasma. Its darkest part is known as **Umbra** with a temperature of approximately 4000 K, while around exists a region of lighter filaments called **Penumbra** with a temperature of approximately 5000 K. Sunspots that do not exhibit penumbra are called **Pores**. (Vaquero J.M., 2009, Chapter 1.2.4)

Sunspots appear in groups and generally in two heliographic latitude zones, in the northern or southern hemisphere, their average latitude value being given by a progressive movement from the mid-latitudes of the hemisphere towards the equatorial region. Its appearance number depends on the solar cycle (11 years).

Sunspots are unique, but they are similar in size and structure. Depending on the magnetic field they can be classified as:

Unipolar: A single spot or a compact group of spots with spacing no greater than 3^o heliographics. In the case of penumbra, the separation is measured from the center of a significant umbra and the closest edge of a penumbra of another contiguous spot.

Bipolar: Two or more spots, a large group of more than 3^o. Generally, a space is formed in the middle of the cluster by dividing it into two different parts. In order to be classified within this category, there must be a minimum separation of 5^o from the main spot. Murdin, 2001, Sunspot Classification

Sunspot Magnetic Field

As mentioned above, sunspots generally appear in magnetic bipolar groups. The magnetic polarity of the main spot in position varies every 11 years with respect to the solar hemispheres,

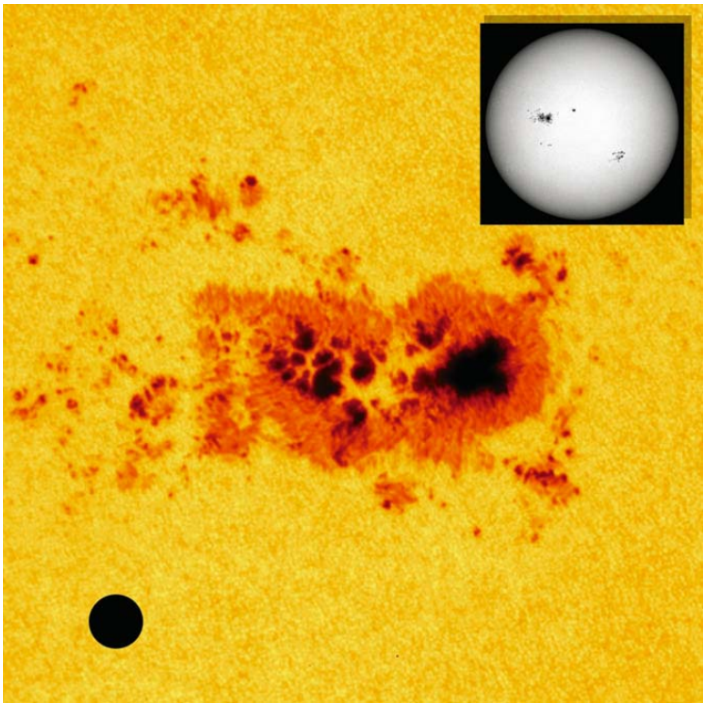

Figure 1.4: Group of sunspots. The image shows in the upper right corner the solar disk in the visible (white light), in the middle a group of sunspots conforming an active region, and in the lower left corner a black circle representing the size of the Earth for comparison. Images taken from SOHO, ESA and NASA (Kenneth R, 2006, Figure 5.2).

this is known as Hale's Law. Every 22 years you can see an inversion in the location of the magnetic fields of these regions, then you can define a 22-year magnetic solar cycle.

Sunspot also appear as upward flux tubes, intersecting with the photosphere. The magnetic induction in the umbra is 0.3 T and in the penumbra it is 0.15 T. In the umbra, the magnetic field is approximately vertical (perpendicular to the solar surface of the place), and this inclination increases as it approaches the penumbra. Hale also observed that, in general, the Sun has a magnetic dipole field of about 10^{-4} T, which reverses each solar magnetic cycle. The vast majority of the magnetic field in the photosphere outside sunspots is concentrated in smaller magnetic elements, with magnetic intensities of around 0.1 to 0.15 T.

From sunspots, it is only possible to observe the surface of their ascending tube flows, therefore a common question when analyzing them is related to the internal structure of the magnetic field in these areas, and how it varies depending on its depth below the photosphere. One of the simplest models is that of a monolithic flow column. First, it is assumed that the pressure inside the flow tube is negligible comparable to the magnetic pressure. It is also assumed that the gravitational force is not relevant in obtaining a magnetic field structure. The magnetic field in polar cylindrical coordinates without taking into account the current is:

$$\vec{B} = \frac{1}{\omega}\left[-\frac{d\psi}{dz}, 0, \frac{\partial\psi}{\partial\omega}\right] \tag{1.15}$$

Thus $\vec{\nabla} \times \vec{B} = 0$, and as $\vec{\nabla} \cdot \vec{B} = 0$ is known, then

$$\frac{\partial^2\psi}{\partial\omega^2} - \frac{1}{\omega}\frac{\partial\psi}{\partial\omega} + \frac{\partial^2\psi}{\partial z^2} = 0 \tag{1.16}$$

The surrounding photosphere, where the flow tube is submerged, has a pressure that varies with height $P(z)$. The boundary conditions of the flow are $\omega = \omega_0(z)$, where

$$\frac{B^2}{2\mu_0} = P(z) \tag{1.17}$$

Therefore, when $z \to \infty$ the field is approximately horizontal, that is $B_\omega \sim F/2\pi\omega_0^2$, and when $z \to -\infty$ the field becomes vertical, that is $B_\omega \sim F/\pi\omega_0^2$.

Although this model explains the orientation, it has problems when calculating the energy, since the difference in radiated energy between the spot and an equivalent area of the photosphere has a difference of a factor of 4, which is less than expected if you have note that convection in the spot is inhibited. This suggests that there is some kind of convective energy transport and that the field should be more complex. (Hanslmeier, 2008, Chapter 4.2.4)

Sunspots and the Magnetic Cycle

It is already known from previous sections, that the amount of sunspot appearance changes over a period of 11 years, just as solar activity is related to sunspots and all magnetic activity. Correspondingly, the Number of Sunspots was introduced as a way to measure solar activity:

$$R = k(10g + f) \tag{1.18}$$

where g is the number of sunspot groups, f the number of sunspots and k is a correction factor depending on the instrument with which these measurements are made to find R. R is given in months to avoid effects of solar rotation and is called the *Relative Number of Sunspots* (Hanslmeier, 2008, Chapter 4.2.4).

1.2.2 Active Regions

Active Regions correspond to localized areas of the Sun where phenomena such as sunspots, faculae, flares and prominences occur, among other phenomena associated with the activity of the star. Among the most evident ones are the *Bipolar Active Regions*, where in a given area of concentrated magnetic field there are two zones with approximately the same amount of magnetic flux but with opposite polarities. These are the characteristic regions of interest for this work, so hereafter, each time we refer to active regions it will be understood that they correspond to the bipolar-type ones. Murdin, 2001, Active Region.

Active regions are formed at sites where there are magnetic field loops similar to the shape of the Greek letter Omega (Ω) emerging from the photosphere into the solar atmosphere (Figure 1.5). All these magnetic loops exhibit magnetic field lines emerging from the photoshphere to the upper solar atmospheric layers. At their base appear *plages* or islands (bright region of the chromosphere near sunspots) near the *footpoints* (intersection zone between the photosphere and the magnetic loops). In one of the footpoints of the solar loop, the magnetic field moves towards the outside of the Sun (positive polarity) and in the other it moves towards the interior of the Sun (negative polarity). At its maximum expansion, after all the magnetic flux has been

released, the active regions have about four orders of magnitude more in spatial scale, magnetic flux and duration (Murdin, 2001, Solar Active Region).

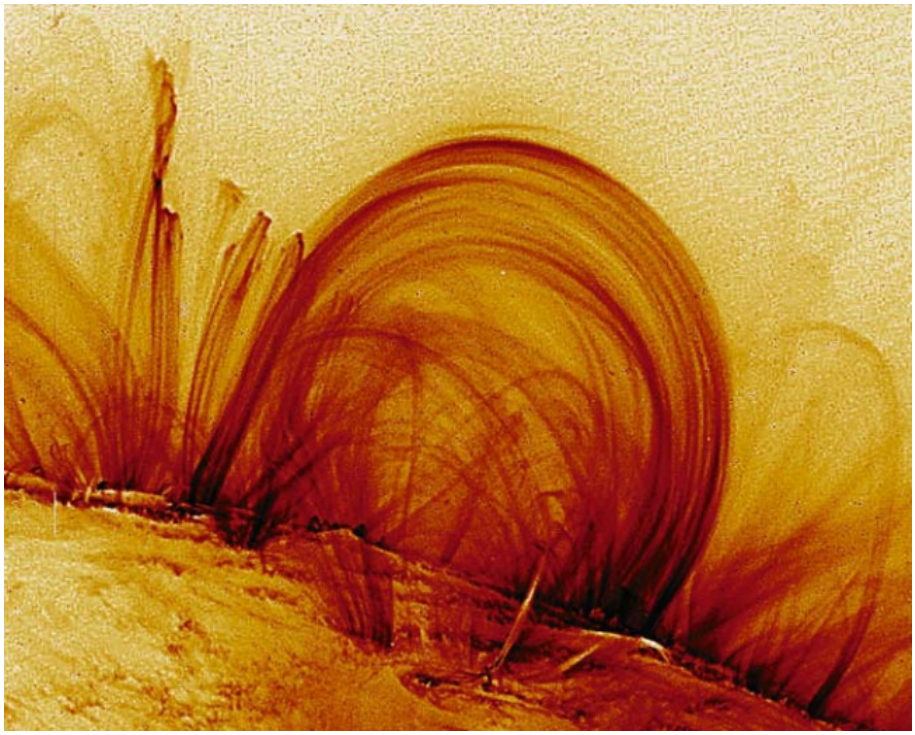

Figure 1.5: Visible Magnetic Loops: Image taken from the TRACE spacecraft (*Transition Region And Coronal Explorer*, (Kenneth R, 2006)

1.2.3 Evolution of Active Bipolar Regions

According to several investigations (Schrijver, 2000), the process of emergence of an active region takes a fraction of time compared to its lifetime. The formation of an active region is associated with the development of an emerging flow region (EFRs) which takes different paths. First, the bipolar region does not appear to affect the near magnetic field in the photosphere and chromosphere. The formed faculae of opposite polarity are separated: during the first half hour of manifestation, the separation ratio of the footpoints can exceed 2 km/s, then descends to values between 1.3 and 0.7 km/s in the next 6 hours. The expansion of the active region continues slowly for the following days. New magnetic flux can appear in the middle of the regions with opposite polarities that have just emerged or in their neighborhoods.

Initially, these regions of emergent bipolar flux may have arbitrary orientation, but generally after one day they assume a ”coherent” rotation of what can be considered a mature active region establishing itself almost parallel to the Sun’s equator.

Large active regions are made up of various EFRs that appear closely in rapid succession within a few days. During this process the polarity distribution is in disorder because the EFRs are not aligned, but usually, the EFRs emerge and are located in such a way that after a day in which all the flow has arisen, a region can be appreciated simple bipolar active.

In general, the EFRs appear as intruders since it has been shown that after the formation of these regions, no upward currents of plasma preceded by the emergent flow are detected. This phenomenon suggests the following behavior between an emerging flow loop and the plasma

around it. A progressive flow loop draws plasma around it. The loop is enhanced by convective instability such that the flow loop and the updrafts are entrained, reaching the photosphere at about the same time. The movement of the flow tubes associated with the loops differ from the divergent plasma flow, because in one part of the region they move in the direction of the local plasma flow and in another region against it. The dynamics of these flow tubes indicate that they are not directly associated with convective flows, but rather are dominated by forces found within the emergent flow loops.

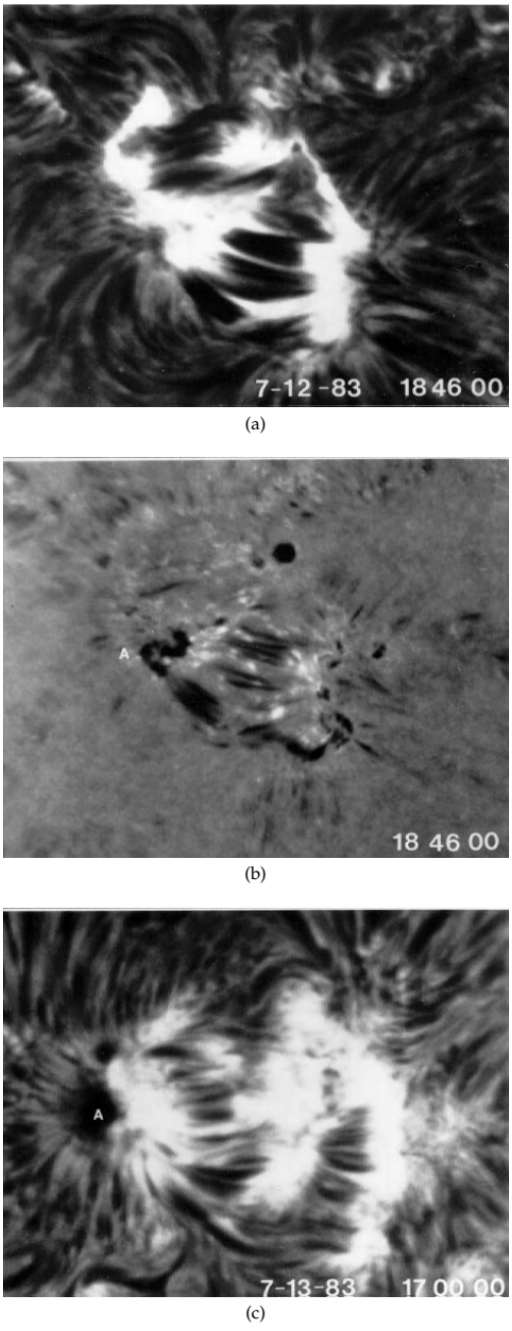

Figure 1.6: Emerging flow region: (a) early stages, H_α line center; (b) early stages, Hα blue wing; (c) 1 day later, Hα line center. Images taken from H. Zirin, Big Bear Solar Observatory.(Murdin, 2001, Solar Active Region, Figure 7)

As new flux continues to emerge in the active region, pores and small spots begin to appear and will merge into larger spots, which implies that the flux tubes are above the photosphere, meanwhile, emerging flux filaments can be observed. Commonly, the new flux is formed in the middle of the 'old' flux so that, in only some parts of the region, these filaments are seen. Subsequently, the distance between the spots of opposite polarity of the active region begins to increase. An example of the growth of an active region can be observed in Figure 1.6 by comparing images (a) and (b) with (c), the latter taken one day later.

The next phase in the development of an active region is the reconnection of the magnetic fields of the bipoles with the fields in the environment in which it has emerged. Figure 1.7 shows en example of an active region and the associated magnetic field and coronal loops. The polarities on the magnetic field map are shown in white (positive) and black (negative); the weak field is shown in gray. A compact bipole can be seen on the right of center with a black map on the left and a white map on the right. The coronal image (right) shows that the black and white regions connect to each other, as would be expected from an emergent bipolar region. However, you can also see outgoing connections of the bipole with the surrounding regions. These loops are formed by the connection/reconnection of the bipolar region with its surroundings (Murdin, 2001).

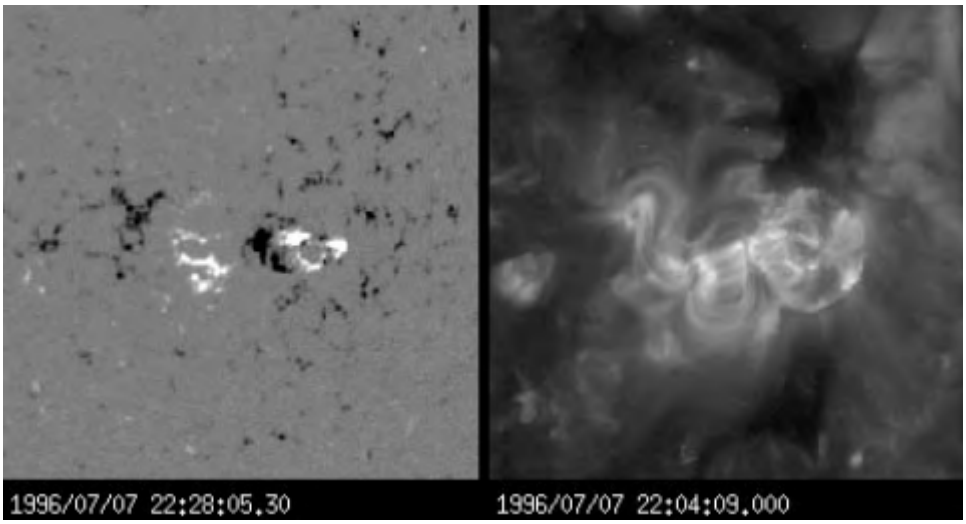

Figure 1.7: Coaligned images of photospheric magnetic field (left) and coronal loops (right) in an active region that has reconnected with its surroundings. Image taken by B. Thomson, NASA/ESA *Solar and Heliospheric Observatory* SOHO (Murdin, 2001, Solar Active Region, Figure 9)

Active regions, where events such as *Flashes* and sunspots generally occur, are between 10.000 and 100.000 km in size, and have a lifetime of one or two months (1 to 2 average solar rotations). They also have unique properties associated with the solar cycle. Few active regions are formed at the minimum of the solar cycle, even not appearing, while at its maximum the frequency of appearance varies by a factor of 8 in phase with the solar cycle. It has also been noted that regardless of whether it is at the maximum or the minimum, the shape and distributions of the active regions are not affected (Kenneth R, 2006).

1.2.4 Solar Flares

A solar flare is defined as a sudden, rapid and intense explosive event of energy release and local illumination in a complex active region, with various wavelengths of range. They usually occur

due to the fact that an accumulation of magnetic energy is generated in the atmosphere that is then released. These energy releases are between 10^{26} and 10^{32} erg of orders of magnitude, in time intervals between 100 to 1000 seconds, in a small area of the Sun that does not occupy more than 0.01% of the solar disk. The flares are hotter than the environment of the corona, and on some occasions they can lose balance and even reach a higher temperature than the solar core in a short period of time. They emit in a range of radiation, from radio, visible, extreme ultraviolet (EUV), X-rays, γ-Rays and particle emission. In white light only very energetic flares can be visible.

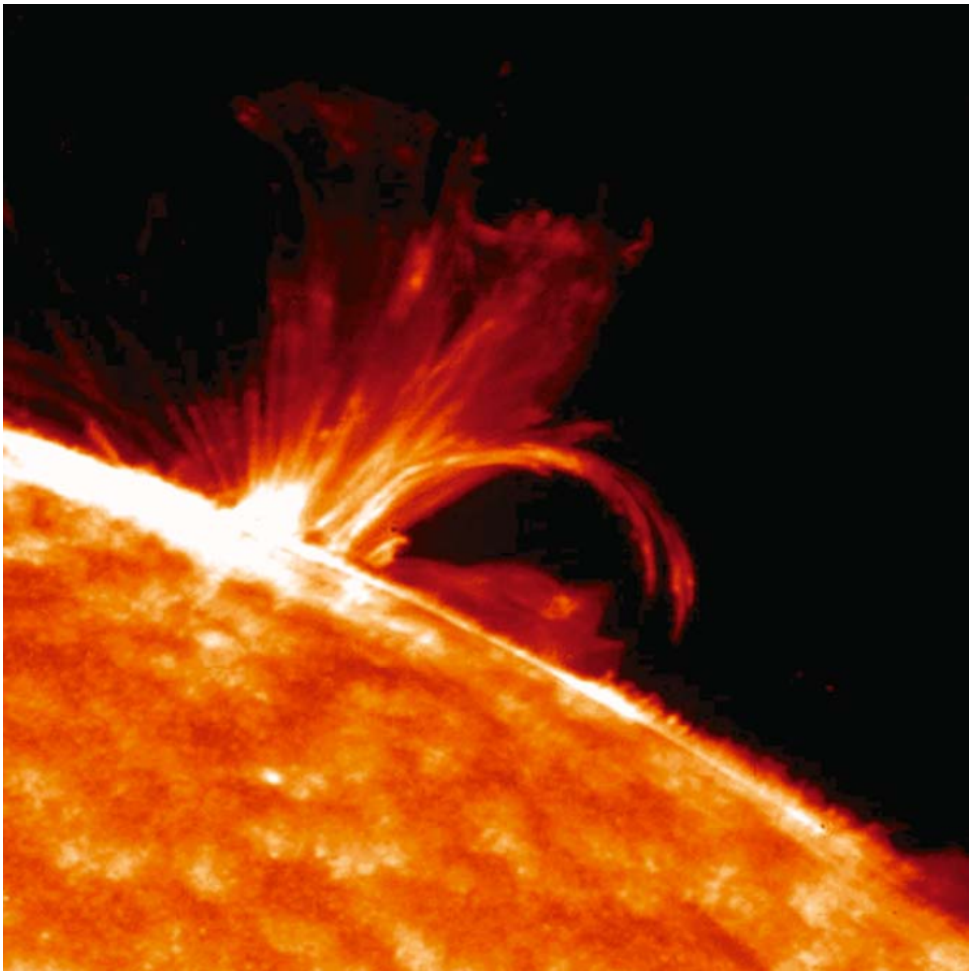

Figure 1.8: Flare in EUV: This image shows that radiation is emitted by long, thin, and numerous magnetic filaments. Image taken by *Transitional Region And Coronal Explorer: TRACE*. (Kenneth R, 2006, Figure 7.1)

The first observation of a solar flare was made in white light by astronomers Richard Carrington and Richard Hodgson in 1859. This emission originated in a small area of an active region and persisted for a few minutes. Later, when the Sun was already extensively studied in the Hα lines in the chromosphere, more reports of the observation of flares and some details about their great complexity were generated.

In the late 1950s, it was possible to observe flares in hard X-rays (X-rays with high photon energy, greater than 5-10 keV), which allowed L.E. Peterson discovered in 1958 the first emission during a flare. Later, development in microwave and X-ray emissions led to the discovery that these emitted particles contained a significant fraction of the initial energy release of the flare

(around 50 %). In 1972, the emission of γ-Rays from heavy nuclei excited by MeV protons was discovered, which made it possible to detect ionic acceleration in flares. Emissions of EUV and soft X-rays ($<$ 10keV) showed that the energy of the flares heats the plasma of the coronal loops to temperatures between 1 to 3 $\times 10^7$ K, in a matter of minutes some loops of active regions become bright in soft X-ray emission hiding the corona (Benz, 2002, Chapter 1.2.3).

Generally, flares occur in areas above the photosphere, where the electric current reaches a maximum (the maximum $\vec{\nabla} \times \vec{B}$). They usually appear above sunspots, or groups of them, while magnetic fluxes of opposite polarity emerge. Progressive large flares generally occur on the neutral lines of the photosphere, where regions of different polarity separate. These neutral lines are connected by the arcs of the loops, thus, in H_α, they are seen as two shapes of bright loops formed by the footpoints on each side of the neutral line. Like this, flares appear on the neutral line of magnetic polarity where it has been most affected (cut) due to the different movements at both sides. In quiet regions of the Sun, the most powerful microflares occur at the limits of supergranular cells (Vaquero J.M., 2009, Chapter 1.9.3).

Phases of solar flares

A typical large flare has three main phases (Benz, 2008, Chapter 1.3):

- *Preflare*: Coronal plasma in the flare region heats up slowly and is visible on soft X-rays and EUV. However, sometimes non-thermal emissions occur that are observed in different zones in the following phases.
- *Impulsive Phase*: A large number of energetic electrons ($\sim 10^{38}$) and sometimes ions with the same amount of energy are accelerated, when most of the energy of the flare has been released. The appearance of footpoints in the chromosphere can be observed in hard X-rays. Likewise, some high-energy particles are trapped, which produces radio emissions. After this phase, emissions in H_α and thermal soft X-rays reach the maximum, when the energy is released with less power, manifesting itself in pulsations and subsequent distribution.
- *Flash Phase*: In this phase, the rapid increase in the width of the intensity of the H_α line stops. It mostly coincides with the impulsive phase.
- *Decay Phase*: Most coronal plasma returns to its original state, not including the corona, where magnetic reconfigurations continue to occur, plasma ejections, and shock waves continue accelerating particles causing interplanetary particle events.

Classification of solar flares

There are different types of flares classification (Hanslmeier, 2008, Chapter 4.3.5):

- Optical Classification: The classes used are S, 1,2,3,4, which are used according to the area in which the flare in the solar disk is included. It refers to subflares and is expressed in millionths of a solar hemisphere.
- Soft X-Ray Classification: This classification has been done since 1970 in the band 1 to 8 Å. Using the intensity emission peak on a logarithmic scale, the size of the flare is known.

  According to this table, a B5 flare has a peak flow of $5 \times 10^{-7} \mathrm{Wm}^{-2}$. Flares of class less than C1 can only be detected during the solar minimum phase. Sometimes flares can exceed class X9 in intensity, these are classified as X10, X11, and so on.

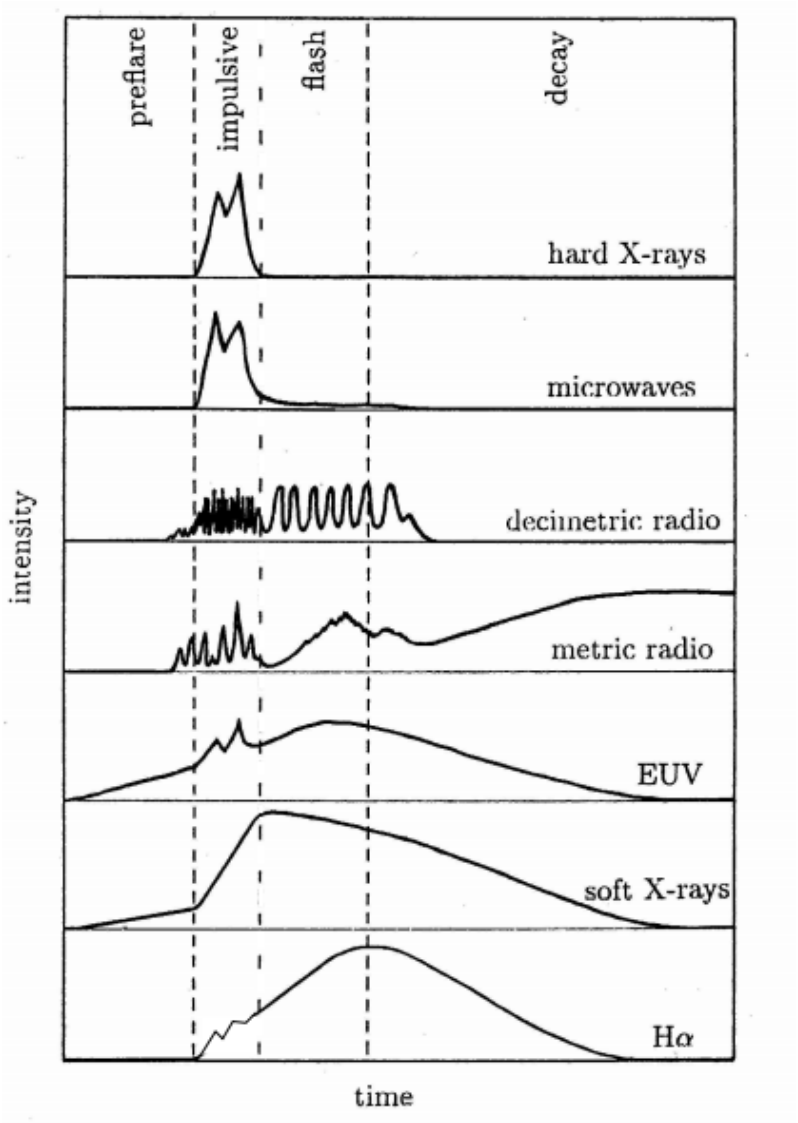

Figure 1.9: Scheme of the intensity of flares at different wavelengths (Benz, 2008, Figure 1.5)

Important Class	Area in 10^{-6} of a solar hemisphere
S	$A < 100$
1	$100 \leqslant A < 250$
2	$250 \leqslant A < 600$
3	$600 \leqslant A < 1200$
4	$A \geqslant 1200$

Table 1.3: Optical classification scheme of flares (Hanslmeier, 2008, Table 4.2)

- Classification into impulsive and gradual: Due to the magnetic topology, one can speak of a time scale classification.

  Long-duration flares are related to coronal mass ejections (CMEs), however, some short-duration flares have also been observed to cause ejections. Flares are events that occur in a single active region, while CMEs can spread out over several of these. Magnetic field lines in CMEs are open in eruptive events, then they close or reconnect within several

Soft X-ray class	Peak in power of 10 in the range of 1-8 Å flux W m^{-2}
A	-8
B	-7
C	-6
M	-5
X	-4

Table 1.4: Soft X-Rays classification scheme of flares (Hanslmeier, 2008, Table 4.3)

hours, providing a long release of energy that is characteristic of eruptive or gradual flares. Then, at the intersection of the newly formed loops on the solar surface, two parallel arcs can be observed at H_α.

Magnetic reconnection of loops can generate events that are confined or eruptive. Impulsive flares of the order of about 10^{24}J generally expand over an area of about $10^{14}m^2$ in H_α, therefore the difference between eruptive and impulsive flares can be given by the order of intensity.

- Radio Burst: Radio bursts are observed at wavelengths from mm to km. In 1950 the radio classification was developed by French and Australian astronomers. This classification can be observed in the *Dynamic Spectrum*: a diagram in which the x axis is related to time and on the y axis the frequency. Since the frequency varies with height, with this it is possible to study the evolution of flares and their propagation through the solar corona.

Type	Confined	Eruptive
Radio Burst	III/IV	II/IV
Soft X-Ray Duration	$<$ 1h	$>$ 1h
CME	-	Si
Interplanetary shocks	.	Si
Events/Year	$\sim$ 1000	$\sim$ 10

Table 1.5: Radio classification scheme of Solar Flares (Hanslmeier, 2008, Table 4.4)

Type III and V burst are characteristic of impulsive flares or the impulsive phase of fully developed flares. They are also associated with the acceleration of electrons along field lines towards the corona. Type III explosions generally occur in active regions (then they may or may not have flares). It is related to suprathermic electrons propagating upward out of the corona. The dynamic spectrum of this type is characterized by shifts at both high and low frequencies as the beam excites plasma at low densities that increase in the corona. Type III burst are related to flares.

Type II and IV burst are associated with eruptive flares. Type IIs show a shift in emission, which may be due to shock wave moving through the corona with speeds of around 500 km/s. These types of burst are the result of plasma radiation associated with magneto-hydrodynamic shocks that propagate through the corona. More than 90% of this type are associated with some flare, of which 30% are related to importance class H_α of class 2 and 3. 70% of this type are associated with CMEs. Type IVs are related to the emission of magnetic reconnection in CMEs.

1.3 Solar Magnetic Field

1.3.1 Magnetic Field and Solar Cycle

Most phenomena in the solar atmosphere are related to the magnetic field, which is organized into much more complex structures that cover a wide range of space above the solar atmosphere, changing systematically in the 11-year solar cycle (Chaplin, 2006, Chapter 10). At the minimum point of the cycle, weak magnetic fields appear with high uniformity where large concentrations of magnetic field are not evident. The large-scale solar magnetic field, however, has a similarity to a bar magnet, where the positive and negative poles are almost aligned with the axis of rotation, in addition to generating a large-scale dipole field. The magnetic field lines are organized in an enveloping way from positive to negative, such that it produces a *poloidal* type configuration.

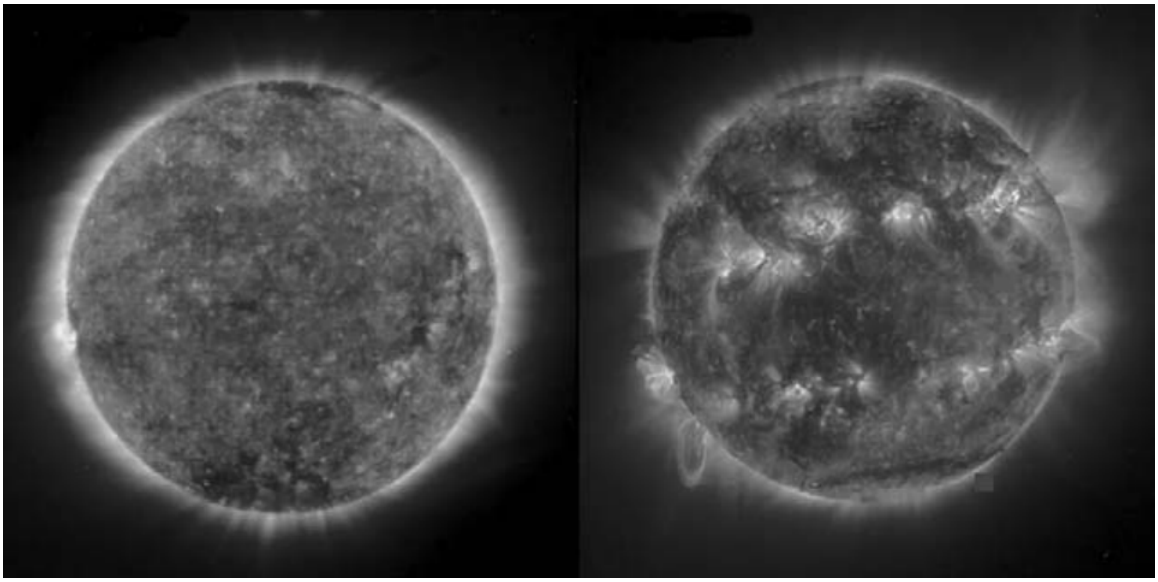

Figure 1.10: The Sun taken at ultraviolet wavelength, with the telescope on board SOHO *Extreme Ultraviolet Imaging Telescope (EIT)*. This image shows the emission by iron atoms in the solar corona at temperatures above one million Celsius degrees. On the left the Sun is observed at the minimum of the solar cycle, while on the right at its maximum. On the right also it can be seen the strong trapped field pattern of an east-west toroidal shape in some pronounced areas, generally where active regions and sunspots are formed. Image taken by the EIT consortium, ESA/NASA (Chaplin, 2006, Figure 3).

From these configurations the active regions begin to appear and with them the sunspots themselves at lower latitudes; then after about 5 to 6 years the number of sunspots and regions with strong magnetic flux reach their maximum, and most are located at latitudes close to the solar equator (about 20^o around the equator). From these observations, there is an hypothesis made, in which the configurations are no longer arranged according to the initial positive-negative (north-south) position but, instead, the magnetic field lines are wrapped in a new east-west *toroidal* configuration.

It is also believed that the magnetic field in the convection zone expands and compresses due to the process of rotation. The field is reduced in small cross sections, which increases the strength of the magnetic field as the density of field lines intensifies, and the field becomes strong enough to generate reactions in the solar plasma. The field then dislodges the plasma

and the field tubes become lighter compared to their surroundings, therefore they are prone to instabilities and thus to rise above this zone. When this happens, sunspots are generated.

The variation in the number of spots and solar active regions is repeated every 11 years in the solar cycle, but these in turn change in polarity. This happens when the poloidal field reverses, then the bar of magnet that we initially consider changes its poles: the one that was north becomes south and vice versa. This process occurs when the active regions and sunspots generated by the toroidal field are at their maximum appearance number.

1.3.2 3D Solar Magnetic Field and its Topology

(Vaquero J.M., 2009, Chapter 1.7) There are two main components to the emergent magnetic flux from the solar surface, depending on the magnetic field topology: (a) *Closed Magnetic Field* (*CMF*) which comprises X-Ray, Ultraviolet and Visible wavelengths; (b) *Open Magnetic Field* (*OMF*), of which the Solar Wind, Heliosphere, High Energy Particles, Interplanetary Magnetic Field and Galactic Cosmic Rays are characteristic. These two topologies generally include planetary atmospheres.

(a) The magnetic flux of active regions is characterized by closed magnetic field lines (CMF) that dominate variations of the total irradiance and the emission of high energies in the solar spectrum (X-rays and Ultraviolet). Most of the radiative losses from the upper layers occur in these regions.

(b) Large-scale magnetic regions have open magnetic field lines towards the interplanetary medium. These generate a continuous outward flow composed of charged particles such as protons, neutrons and helium nuclei, which is known as **Solar Wind**. The solar magnetic field of the open region (OMF) is frozen into this wind, creating the Interplanetary Magnetic Field (IMF). This produces a large-scale magnetic field region called the **Heliosphere**, which reaches all sites in the solar system.

Galactic Cosmic Rays (GCRs) are composed of high energy particles, mainly protons with energies between 1-20 GeV. These are generated outside the solar system and impact the Earth continuously from different directions. Both, the flow and the energy spectrum of GCRs, depend on the strength of the Heliosphere, being stronger when the IMF is weaker.

In Figure 1.11 the two topologies can be distinguished: (a) Active regions with closed magnetic field are observed in the bright regions, while (b) open magnetic field lines characteristic of the interplanetary medium are seen in the dark regions.

1.4 Space Weather

In this section, we will see how the Sun is involved in space weather and some of its consequences on Earth.

1.4.1 The Sun as the main source of space weather

(Volker Bothmer, 2007, Chapter 3) The Sun is the main source of energy in the solar system and of space weather. As we have seen, the main forms of energetic output from the Sun are flares, coronal mass ejections, events of solar energetic particles, among others, which determine conditions in the interplanetary medium and geospace, and their variation with the solar cycle.

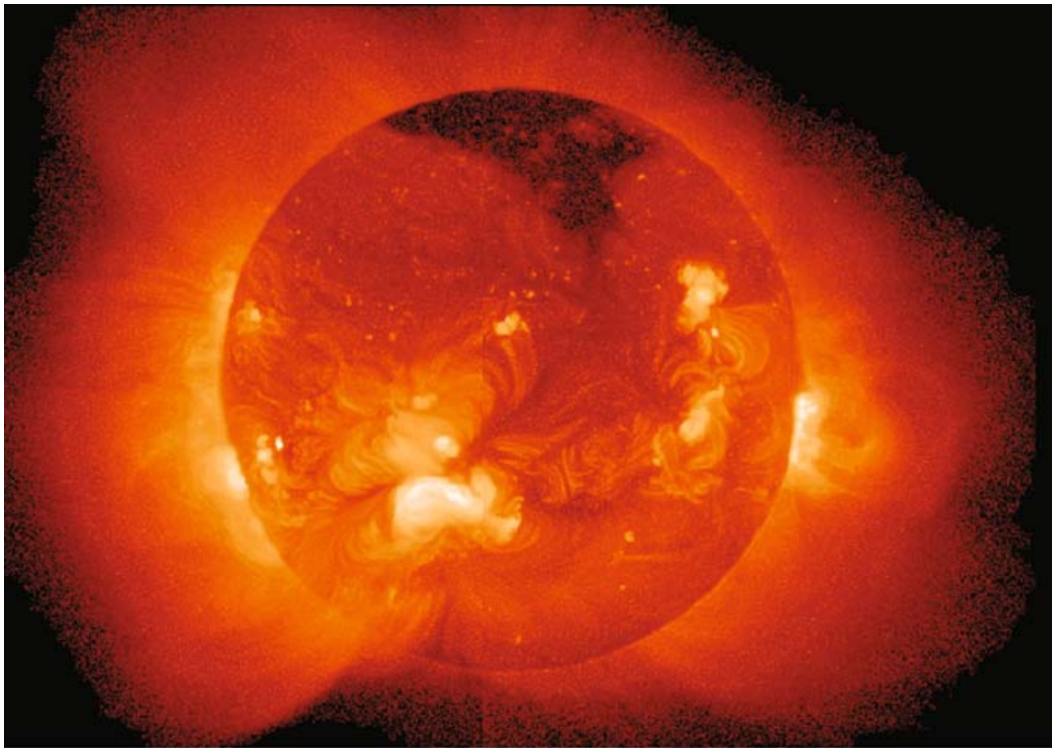

Figure 1.11: Solar disk in X-ray observed by the Yohkoh satellite, T. Shimizu, *The Institute of Space and Astronautical Science, Japan.* (Vaquero J.M., 2009, Figure 1.28)

In previous sections, it was shown that magnetic structures in the photosphere generate different explosive events (such as flares, prominences, CMEs, etc) which cause short-time emissions in EUV, X-ray, γ-ray and radio waves. On Earth, solar observations at wavelengths in X-ray and EUV must be accomplished through space missions. The irradiance of the Sun varies in the order of 0.1% in the course of the solar cycle, but the variation in specific ranges of wavelengths may be greater, and for this reason there is great interest in this area of research, since variations in UV and EUV wavelengths can have great effects on Earth's atmosphere. Therefore, the solar cycle and its variation is of great importance, either for space weather, for the temporal conditions that occur in the Sun, as well as for the interplanetary medium and geospace.

Information obtained from the analysis of individual cycles, such as rapid growth and decay, and the prediction of the strength of the next cycle, are generated as an aid to analysis. Using data from the Michelson Doppler Imager (MDI) for example, Dikpati et al. (2006) developed a flux transport model for the variation of the solar magnetic flux in different cycles, obtaining the results that solar cycle 24 will be between 30 to 50% stronger in terms of activity, being somewhat proportional to the evolution of the magnetic flux in the photosphere compared to the solar cycle that was taking place at the time of the research, although the prediction of the strength of the solar cycle at the time, is still uncertain.

The shape of the solar corona also varies with the activity phase of the solar cycle. During solar minimum the corona is more or less symmetric with respect to the solar equator and large coronal streamers are usually seen (Figure 1.12).

In addition to electromagnetic radiation, the Sun continuously emits a flow of charged particles (plasma) from the corona, that is, the **Solar Wind**. This has speeds of hundreds of km/s and fills the heliosphere, which is the region of interstellar space that occupies distances up to 100

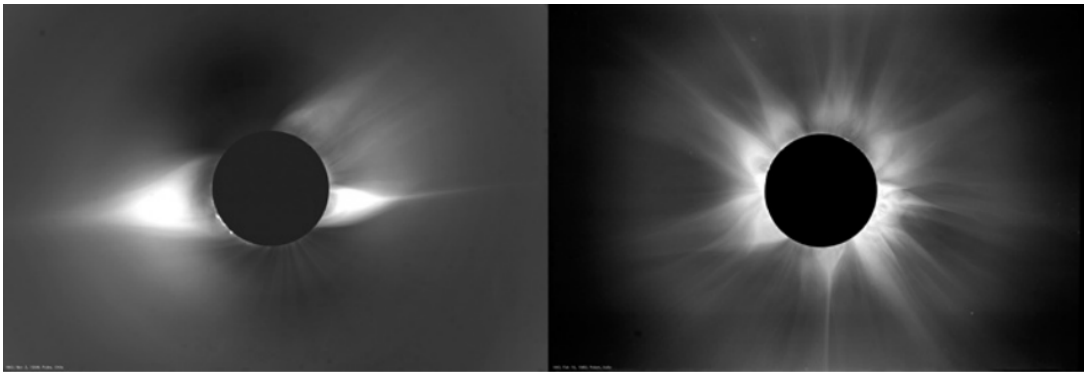

Figure 1.12: Left: Solar corona near solar minimum, seen during the total solar eclipse of November 3, 1994. Right: Solar corona near solar maximum, seen during the total eclipse of February 16, 1980. (Volker Bothmer, 2007, Figure 3.7)

AU, which means it extends to greater distances than those found by the most distant planets in our solar system. The properties of the solar wind and its evolution in the heliosphere control together with the flow of energetic particles in the energy ranges from eV (suprathermal) to MeV, the conditions of interplanetary space weather. The supersonic flow of the solar wind constantly affects the Earth's magnetic field. Along with the quasi-steady flows of the solar wind and energetic particles, there are solar winds and transient particle flows in which the solar wind can impact the Earth's magnetosphere with speeds of more than 2000 km/s and with particles of around GeV, as well as large solar flares and emissions of electromagnetic radiation, which can generate disturbances in the atmospheric conditions of the Earth.

1.4.2 Effects of Space Weather on communications

The variety of communication technologies that can be affected by the occurrence of natural processes of the Sun and space around the Earth, has increased significantly due to the rapid development of these technologies in the last century (Volker Bothmer, 2007, Chapter 9).

The discovery of Van Allen (van Allen, 1983), and Vernov and Chudakov, that magnetically confined charged particles exist around the Earth, demonstrated that this region (within the magnetosphere) is filled with particle radiation of sufficient intensity and energy to cause significant damage to satellites that may be orbiting both in their materials and in their electronics. Due to trapped radiation, the first telecommunications satellite, Telstar 1, launched on July 10, 1962, suffered anomalies in one of its two command lines within a few months after its launch, and after five months its two lines failed.

It was clear then from the Van Allen discovery, and from the Telstar event, that telecommunications satellites orbiting the Earth should be designed to withstand radiation from this environment. Likewise, as technology continues to evolve in both sophistication and miniaturization and its interconnectivity, a deeper understanding of Earth's space environment will be needed. Some of the effects of solar-terrestrial processes on communications are shown in Table 1.6.

Carrington Event

The Carrington event was a geomagnetic storm of great power on September 1-2, 1859 during solar cycle 10 (1855-1867). Richard Carrington detected a large area of sunspots in the northern hemisphere of the Sun. The area of the largest sunspot at approximately 45°N solar latitude detected on August 31 was the most notable. The observation of this sunspot region caught

Solar-Terrestrial Processes	Affected communications
Ionosphere Variations	
Induction of electrical currents in the Earth	Long communications cables.
Wireless signal reflection, propagation, attenuation	-Commercial radio and television. -Local and national safetty and security entities. -Aircraft Comunications.
Communication satellite signal interference, scintillation.	Commercial telecom and broadcast.
Magnetic Field Variations	Attitude control of communications spacecraft
Solar Radio Burst	-Excess noise in wireless communications systems. -Interference with radar and radio receivers.
Charge Particle Radiation	-Solar cell damage. -Semiconductor device damage and failure. -Faulty operation of semiconductor devices. -Spacecraft charging, surface and interior materials. -Aircraft communications avionics.
Micrometeroids and Artificial Space Debris	-Spacecraft solar cell damage. -Damage to surfaces, materials, complete vehicles. -Attitude control of communications spacecraft.
Atmosphere	-Drag on low-altitude communications satellites. -Attenuation and scatter of wireless signals.

Table 1.6: Impacts on solar-terrestrial processes on communications. Taken from (Volker Bothmer, 2007, Table 9.1)

Carrington's attention, comparing it to the research he had conducted in previous years. During his investigation of this region, he recorded the early observation of a solar flare, a glow that lasted for about 5 minutes and moved over the entire contour of the spot. Hours after this outburst of light from the large sunspot region, disturbances were observed in magnetic measuring instruments on Earth. The flare was associated with a large coronal mass ejection that traveled into the Earth's magnetosphere in just 17.6 hours (a journey of about 150 million kilometers), inducing one of the largest geomagnetic storms.

Northern Lights were seen around the world down to low latitudes such as in southern Central Mexico, Cuba, Hawaii, southern Japan and China, even in latitudes near the Equator as in the case of Colombia. The storm's strength is estimated to have ranged from -800 nT to -1750 nT (Phillips, 2014).

1.4.3 Space Weather in power grids

The solar wind formed by particles emitted by the Sun, interact with the geomagnetic field producing the magnetosphere around the Earth (Volker Bothmer, 2007, Chapter 10). The magnetosphere is in a complex plasma-physical coupling with the ionosphere. During space weather storms, the magnetosphere-ionosphere system is highly disturbed, containing intense currents that vary rapidly. Some important effects are the auroral electrojets accompanied by currents in high latitudes of the ionosphere. On Earth, they manifest as spatial variable current disturbances or storms in the geomagnetic field and therefore, a geoelectric field is induced (Faraday's Law of induction). The electric field generates currents, known as Geomagnetically Induced Currents (GIC) in terrestrial technological networks such as electrical power transmission sys-

tems, oil and gas pipelines, telecommunications cables and railway equipment. GICs therefore comprise the extreme end of the space weather chain. In power grids, GICs can saturate transformers, which can cause a variety of problems, from harmonics in the electricity to system-wide blackouts and permanent transformer damage. In pipelines, GIC can increase corrosion and interfere with the protection of survey systems and control. Likewise, the GIC can cause telecommunications and railway equipment to suffer overvoltages, possibly due to failures.

The first observations of the effects of space weather on technological systems were in the first telegraphs more than a century and a half ago. Systems were becoming inoperable, and operators were sometimes able to run without batteries using voltages induced by space weather. These situations depended on whether the direction of the induced voltage was in favor or against the operational voltage. Nowadays, fiber optic cables are not directly affected by space weather, but GIC can flow in metallic cables used by power repeaters.

Statistically both GIC phenomena and other space weather processes follow the 11-year sunspot cycle, however, large storms can also occur during the minimum, therefore there is a constant concern of possible GIC effects.

1.4.4 Solar storm of August 1972

In August 1972 the McMath 11976 active region produced a series of flares, energetic particles and ejections directed towards the Earth (Knipp et al., 2018). The first two ejections generated two impulses in the geomagnetic field and later after the 01 UT of August 4th a magnetic storm, this clearing the interplanetary path for an ultrafast interplanetary coronal mass ejection (ICME) that reached Earth in a record time of 14.6 hours. This ICME is associated with a bright Hα flare that peaked on August 4th at 06:21 UT. The SOLRAD-9 satellite X-ray detector was saturated to a magnitude of X5.1 in the current solar X-ray classification of the National Oceanographic and Atmospheric Administration (NOAA) solar X-ray classification, but, using phase propagation disturbances of ionospheric radio waves, the class of the flare was estimated to be $\sim$X20. Blackouts were generated on Earth in a matter of minutes and the X-ray radiation was sustained for more than 16 hours due to the long duration of the flare.

The Guam Observatory reported at 20:54 UT (06:54 local time) an extraordinary 62 seconds rise time for the sudden onset of a storm consistent with a 3080 km/s collision that swept through the magnetosphere. In Boulder, CO, USA, the magnetometer went off its scale and a bright aurora appeared over the northern United States. At 22:38 UT in India at low latitudes a significant disturbance appeared, a sudden impulse (SI) that swept this country with amplitudes between 301 and 486 nT. Similarly, this SI also took the magnetometer located at the Honolulu Observatory off its scale around noon. Also within the first 15 minutes of the first glow of what would be an aurora bright enough to cast shadows, appeared along the UK coastline and within 2 hours commercial airline pilots reported auroras as far south as Bilbao in Spain.

Naval effects also occurred in the middle of the Vietnam war due to the interplanetary disturbance of August 4th, this was the sudden detonation of a large number of sea mines of the U.S. Navy influenced by magnetism, left in the coastal waters of North Vietnam.

This event is one of the clearest examples of the need for space weather forecasting.

1.5 SAMNet: The Solar Activity Monitor Magnetic Network

(Erdelyi et al., 2021) The Solar Activity Magnetic Monitor (SAM) Network (SAMNet) is a future international network of ground-based telescope stations, a project led by the UK. SAMNet

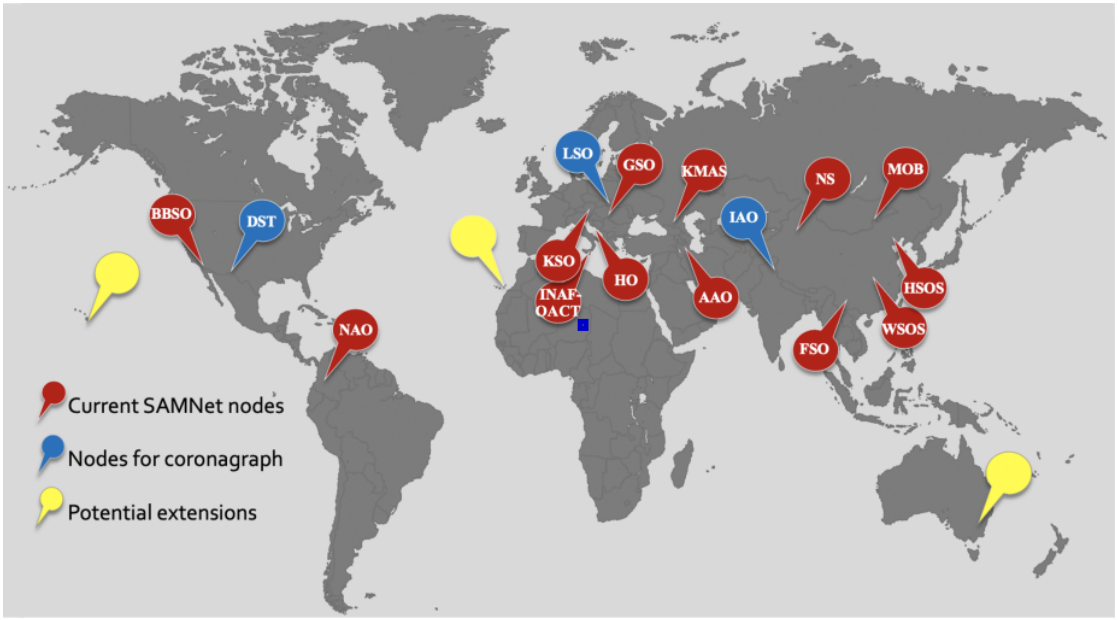

Figure 1.13: Potential host sites for future SAMNet sentinels. The blue marks highlight sentinels with about 5-8 hrs time zone differences to indicate where a coronagraph could be added as 4th OTA (optical telescope assemblies). Yellow marks are potential future expansion sites. Taken from Erdelyi et al. (2021, Figure 15).

will be able to monitor the Sun's intensity, magnetic and Doppler velocity fields at multiple heights in the solar atmosphere. Current international scientific partners with various levels of support and with principal interest include the countries shown in Figure 1.13.

Each SAMM (Figure 1.14) will be equipped with a set of identical telescopes, each with a different magneto-optical filter (MOFs) that will carry out observations in the KI, Na D and Ca I spectral bands. Likewise, a subset of SAMMs will have white-light coronagraphs and emission line coronal spectropolarimeters.

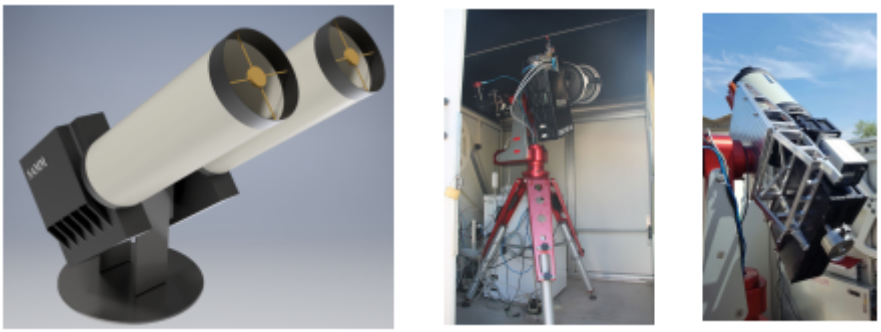

Figure 1.14: Snapshot of the scaled-down SAMM prototype telescope at various stages of its design and development. Taken form Erdelyi et al. (2021).

The objective of SAMNet is to provide observational data for research for space weather forecasting. The goal will be to operationally achieve a warning of between 2 to 8 hours ahead of a occurring event such as solar flares and to provide synoptic maps of interest of the lower solar atmosphere with a limited spatial resolution either only by the limit of vision or diffraction, whose cadence will be 10 minutes. The individual SAMM units will be connected to their main

HQ center, where all information received from all slave stations will be processed automatically and a flare warning of up to 26 hours will be issued.

1.5.1 Colombian node for solar observation (SAMco)

The Colombian node is called SAMco, and it will provide the first equipment of its kind in the country (Joya et al., 2020). Colombia will contribute high-level data for the first time to a global forecasting service of such characteristics. The country will also have an outstanding contribution in the development of algorithms and artificial intelligence technologies for the processing of solar magnetograms (Granados-Hernández and Vargas-Domínguez, 2020). For this, the evolutionary characteristics of the solar magnetic field will be analyzed in real time with data from the nodes of the network. This contribution has implications for the industry and important contributions in the handling of large amounts of data (big data) and machine learning, with direct and indirect repercussions on technologies associated with the fourth industrial revolution.

1.5.2 The Weighted Horizontal Magnetic Gradient Method

Recent studies that investigate the prediction of solar flares (Korsós et al., 2014, 2015) use certain variables of importance in active bipolar regions for their detection, these are: area and magnetic field of the umbra of sunspots of opposite polarity and the distance between its barycenters. The data used for this analysis was obtained from SDD (SOHO/MDI-Debrecen Data), which contains the data of positions, areas and mean magnetic fields for all observable sunspots from 1996 to 2010. The data analyzed was a sample of 142411 sunspots. The dependence of the mean magnetic field and umbra area was calculated (Equation 1.19) from Figure 1.15:

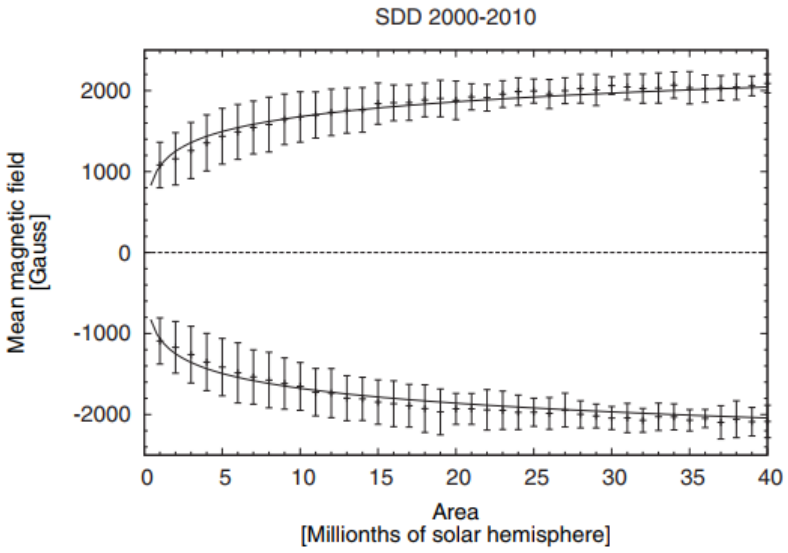

Figure 1.15: Dependence of mean magnetic field of both polarities umbras from Korsós et al. (2014).

$$B_{mean} = f(A) = K_1 \cdot \ln(A) + K_2 \tag{1.19}$$

where $|K_1| = 265$G and $|K_2| = 1067$G. As the intention to set this dependence is to find the horizontal gradient magnetic field of the two areas involved, the magnetic field will be

represented as the magnetic flux inside the umbra which can be obtain with the product from $B_{mean} = f(A)$ and its area. Korsós et al. (2014) defined a new proxy to represent the magnetic field gradient between two sunspots of opposite polarities with A_1 and A_2 areas at a distance d:

$$G_M = \left| \frac{f(A_1) \cdot A_1 - f(A_2) \cdot A_2}{d} \right| \tag{1.20}$$

which is being consider as possible proxy of non-potentiality at photospheric level. It was found a pre-flare characteristic behavior when relating this proxy through time. This is when a flare is about to occur, the G_M will increase its value due to the proximity of the sunspots of opposite polarity and the magnetic flux amount generating a maximum value, then when they set aside, the proxy will decrease and the flare will manifest. This can be seen in Figure 1.16.

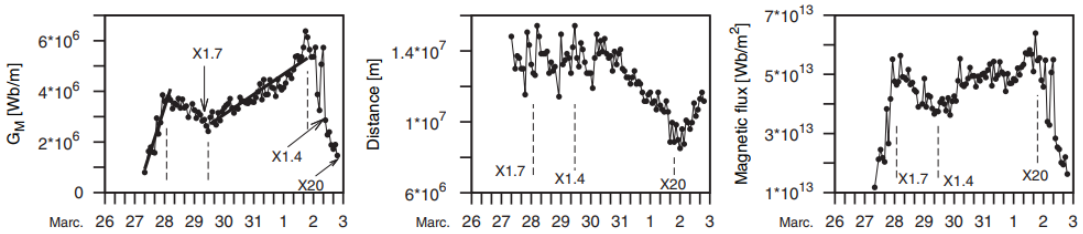

Figure 1.16: Diagram of the variation of G_M, distance and magnetic flux of the active region AR NOAA 9393 (Korsós et al., 2014, Figure 2).

Assuming now that the process involving a flare generation is due to a collective behavior between nearby spots, Korsós et al. (2015) in a later work, defined a generalize proxy that allows to use these values, called the *Weighted Horizontal Magnetic Gradient* (WG_M):

$$WG_M = \left| \frac{\sum_i B_{p,i} \cdot A_{p,i} - \sum_j B_{n,j} \cdot A_{n,j}}{d_{pn}} \right| \tag{1.21}$$

where the d_{pn} is the distance between the barycenters of the opposite polarities sunspot and the indices p and n denote positive and negative polarities. In this case i and j will denote the running indices in the selected spot cluster. With this new proxy the behavior previously seen is now consistent with the distance behavior, which is showing previous the flare formation a parabolic like form and in the end of it, the flare manifestation. This can be seen in Figure 1.17.

In order to have a predictive model regarding the flare formation, that is in this case, an estimated time in which these flares may or may not occur, Korsós et al. (2015, 2019) developed a statistical analysis involving the behavior of the WG_M using the values of this proxy at its maximum WG_M^{max} as well as the moment of the flare manifestation WG_M^{flare}, so that if a flare occurs, an estimate of the time range in which another flare can be generated can be provided. In Korsós et al. (2019) they found that if this percentage difference $WG_M^{\%}$ is greater than 54%, no further flares are expected to occur, but if is the value is below 40%, a flare will probably occur in the next 18 hours. If the percentage difference is between 40% and 54%, there is no reliable statement about a possible further flare manifestation.

1.5.3 Analysis of Magnetic Polarity Centroids in Solar Active Regions

Taking into account the work mentioned in Section 1.5.2, Granados Hernández (2019) used instead of SDD Debrecen data, magnetograms from the SOHO/MDI telescope to find the G_M

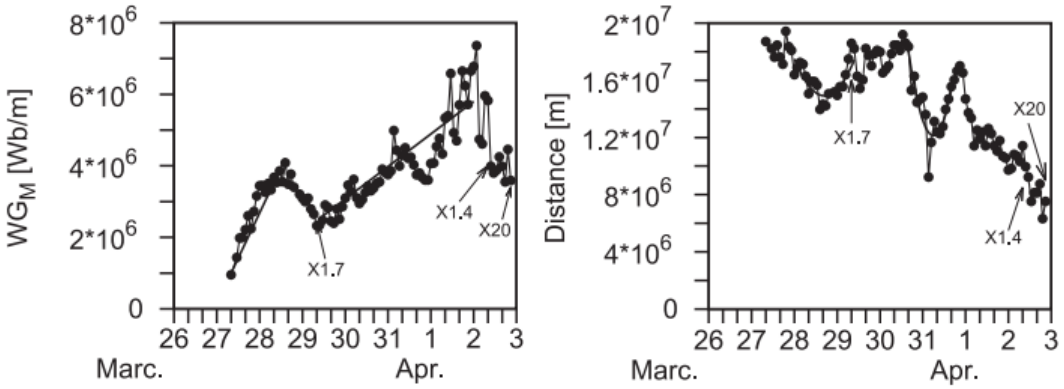

Figure 1.17: Diagram of the variation of WG_M and the distance of the active region AR NOAA 9393 (Korsós et al., 2015, Figure 2).

and WG_M using image analysis to obtain the area from the umbras, the mean magnetic field and the distance between the barycenters of the sunspots with inverse polarity. Also, instead of finding a mean magnetic field by fitting the area versus the magnetic field, it is used the one proportioned by the magnetogram. The image processing analysis was pursued with the python software, and the validation of the method was done using three active regions mentioned in Korsós et al. (2014, 2015).

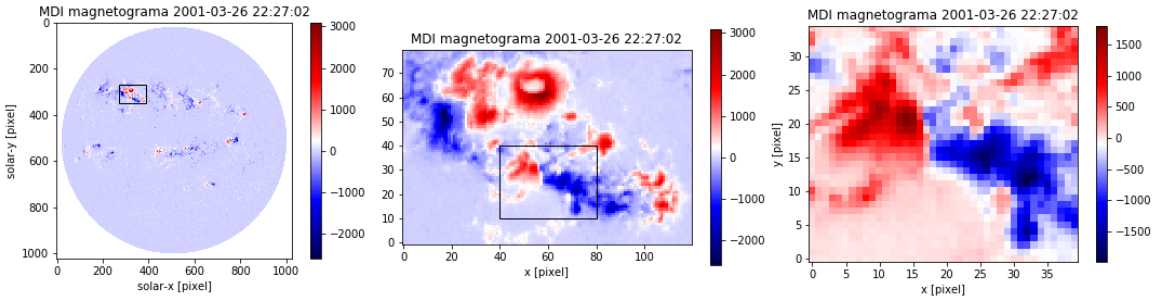

Figure 1.18: Image processing for solar active region AR NOAA 9393.

Full disk magnetograms were taken from the *Virtual Solar Observatory* (Hill et al., 2009) data base, and every active region was followed manually as seen in Figure 1.18. Due to the SOHO/MDI magnetograms have low resolution, the image resolution was improve by doing a pixel rescaling in order to find a smooth line in the umbra, in this case, where there is one pixel, now there will be ten. This can be seen comparing the axes from the right image in Figure 1.18 with Figure 1.19. Then, to estimate the umbra border, mapping color plots were used that allows seeing the magnetograms as level graphics, in this case of magnetic field as shown in Figure 1.19.

Map1 (Figure 1.19 above) allows to divide in 12 levels the magnetogram, while Map2 (Figure 1.19 below) divides it in 20 levels.

Taking this contours into account, it was used 4 conditions to find the opposite umbras barycenters, these were:

1. A mask involving the pixels with values equal or greater than the 40% of the maximum and equal or lower than the 40% of the minimum of the region.

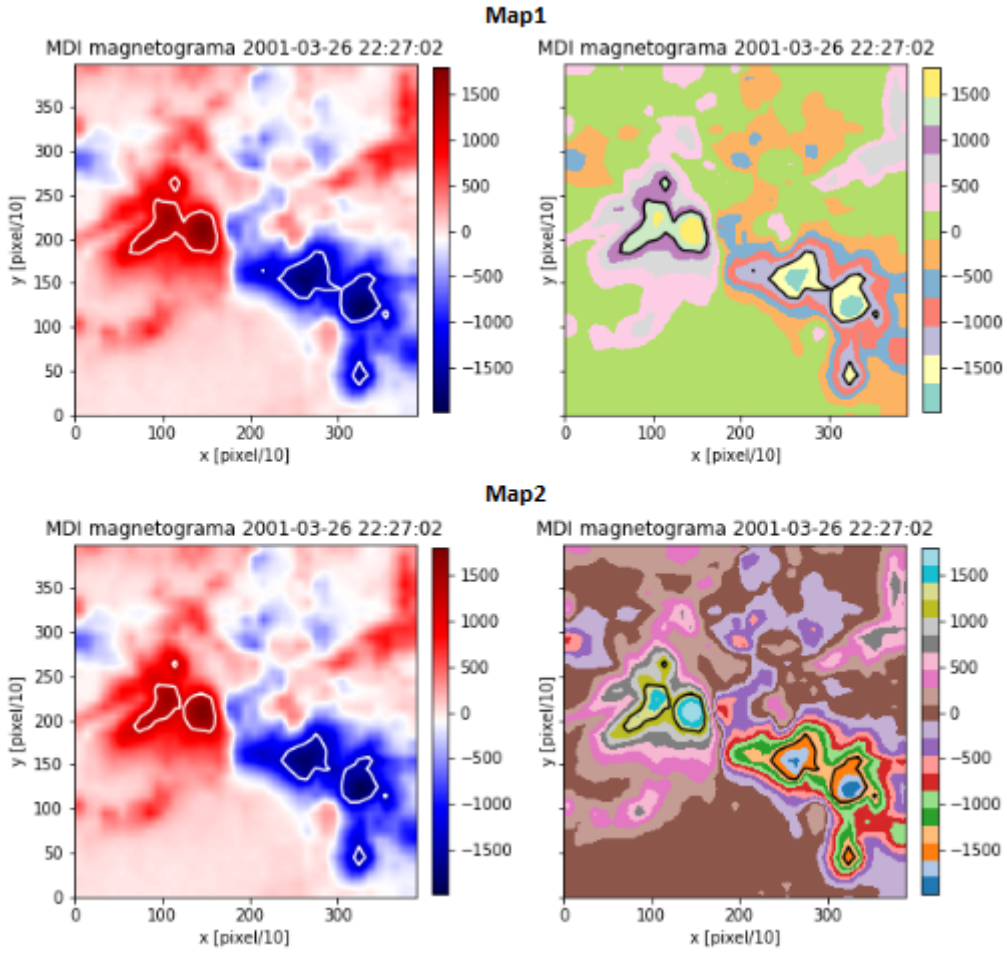

Figure 1.19: MDI Active Region AR NOAA 9393 magnetogram. Top: 12 levels. Bottom: 20 levels.

2. A mask involving the pixels with values equal or greater than the 99% of the maximum and equal or lower than the 99% of the minimum of the region.
3. A mask involving the pixels inside the contour found in Map1.
4. A mask involving the pixels inside the contour found in Map2.

Once the regions were analyzed, all methods were tested with the G_M and WG_M proxy. Granados Hernández (2019) found that the optimum method to estimated a time range for a flare to occur, is using the data associated with the Map2 image analysis and the WG_M. Its behavior can be seen in Figure 1.20.

As in Korsós et al. (2019), in Granados Hernández (2019) a difference percentage was calculated related to the flare manifestation, in order to find a time range in which a flare will or will not probably occur. For this analysis it was found that if the percentage difference $WG_M^{\%}$ is greater than 35.52%, the generation of flares is not expected in the following 18 hours, while if it is less than 30.05% flares are expected to occur in the next 18 hours. If the value of $WG_M^{\%}$ is between 30.05% and 35.52%, it was not possible to give an accurate statement about the appearance of flares.

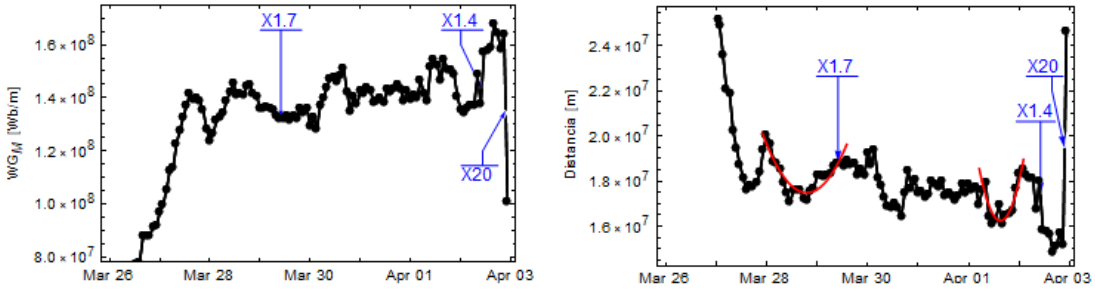

Figure 1.20: WG_M plot through time of Active Region AR NOOA 9393 (Granados Hernández, 2019).

2. Observations and Data Processing

2.1 Solar Dynamics Observatory and the Helioseismic and Magnetic Imager

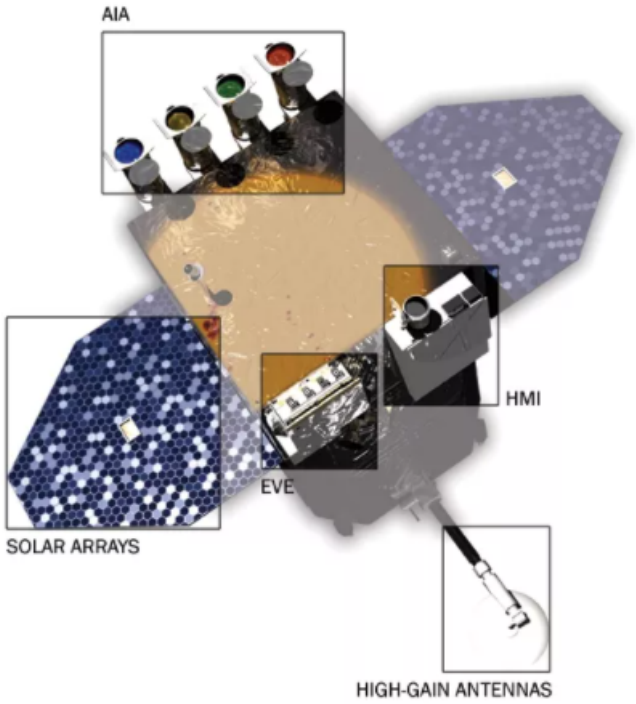

Figure 2.1: Solar Dynamics Observatory.(Howell, 2018)

(Chamberlin et al., 2012) The Solar Dynamics Observatory (SDO) is a space mission launched on February 11, 2010 from the Kennedy Space Center aboard an Atlas V 401 (AV-021) launch vehicle. SDO began to provide data from May 1, 2010, being the first space weather mission of NASA's Living With a Star (LWS) program. The main objective of SDO is to understand, focused on a predictive capacity, variations that can influence life on Earth and human technological systems. The scientific investigations of the SDO will determine how the solar magnetic field is generated and structured, and how its stored magnetic energy is released towards the heliosphere and geospace. Likewise, research done with SDO will guide the understanding of the role that solar variability has in changes in the Earth's atmosphere, its climate and chemistry. The SDO mission contains three scientific investigations: the *Atmospheric Imaging Assembly* (AIA), *Extreme Ultraviolet Variability Experiment* (EVE), and the *Helioseismic and Magnetic Imager* (HMI)), a spacecraft bus, and a dedicated ground station to handle the telemetry (Figure

2.1).

The purpose of the investigations by the Helioseismic and Magnetic Imager (HMI) instrument as part of NASA's SDO is to study the origin and evolution of sunspots, active regions and complex activity, the dynamics of the convection zone and the solar dynamo, the sources and drivers of magnetic activity and associated disturbances, the connections that may exist between internal processes and the dynamics of the corona and heliosphere, and precursors of solar disturbances for space weather forecasts.

2.1.1 SHARPs: Space-Weather HMI Active Region Patches (hmi.sharp_720s)

For this work magnetograms provided by HMI/SDO were used in SHARPs (Space-Weather HMI Active Region Patches) format in LoS magnetic field and taken from the catalog *Joint Science Operations Center* (JSOC) (JSOC, 1997). SHARPs contain space weather information and magnetic field data for *HMI Active Region Patches* (HARPs), provide geometric information, and extract observable HMI map slices. The data is organized by prime keywords HARPNUM (the HARP number) and time T_REC. SHARPs contain maps of vector and line-of-sight magnetic field, velocity, and intensity data for each HARP at each time step. It contains up to fifteen quantities that can be used for the prediction of space weather such as field gradients, current, helicity, emerging flux, free energy, among others (HARP, 1997).

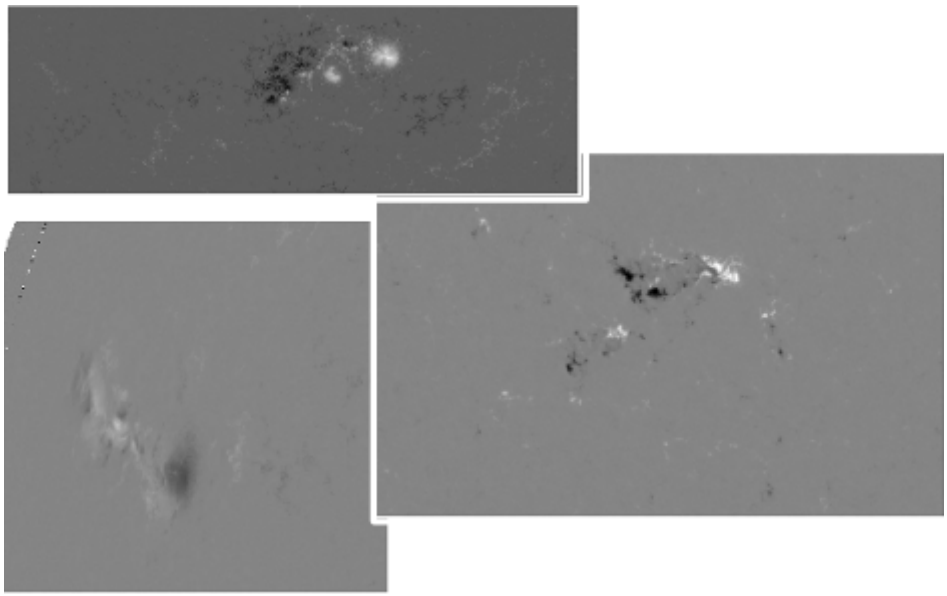

Figure 2.2: HMI Sharp Acive Region Magnetograms examples.

The bipolar active regions were taken from them, that is, areas where a duality of color is evidenced, each color for a polarity of magnetic field (positive and negative). By default SHARPs are downloaded in the FITS extension (*Flexible Image Transport System*). This is a format that simplifies the exchange of astronomical image data between different observatories, since in addition to the image, it contains arrays, a data table and metadata[1]. Because FITS is defined and approved in documents of the International Astronomical Union (IAU), documentation about the keywords of its header and handling of its arrays can be easily found.

[1] https://fits.gsfc.nasa.gov/rfc4047.txt

2.2 Algorithm: Image and Data Processing

2.2.1 Data acquisition

For data acquisition, a python code was made using the **drms** library, which is a SunPy-affiliated Python package for accessing data hosted by JSOC (see http://jsoc.stanford.edu/ajax/exportdata.html), that allows to access HMI and AIA instruments, and also data from the Michelson Doppler Imager (MDI) aboard the Solar and Heliospheric Observatory (SOHO) spacecraft and data from the Interface Region Imaging Spectrometer (IRIS) (Glogowski et al., 2019). The drms package allows the user to process complex codes for any number of metadata keywords and export tailored datasets in different formats, as FITS, movies, images, among others.

For the case of this work, the package will be used to download magnetograms from HMI, particularly in SHARPs formats, using the hmi.sharp_720s data series, which means the cadence of the magnetograms is 720 seconds (12 minutes). To download the data for each active region, the time range will be stipulated, together with the NOAA AR parameter, the product (magnetogram) and the format (FITS). Each magnetogram will be stored in a folder with the same name of the active region to later analyze each one of them automatically. An example of the acquisition of SHARPs is shown in Figure 2.3:

```
In [5]:
c = drms.Client(email='example@mail.edu.co', verbose=True)
si = c.info('hmi.sharp_720s')

keys = si.primekeys  ## Primary Keys ('HARPNUM', 'T_REC')
types = si.segments.loc[['magnetogram']] # Data type

## Dataseries, Datetime range, Active Region, product
ds = 'hmi.sharp_720s[][2011.01.25_00:00_TAI-2011.01.28_23:59_TAI][? NOAA_ARS ~ "11149" ?]{magnetogram}'

## Method of .fits download
r = c.export(ds, method='url', protocol='fits')

print(r.wait(),r.status,r.request_url)

## Folder creation and .fits download
out_dir = 'NOAA_ARS 11149'
if not os.path.exists(out_dir):
    os.mkdir(out_dir)

r.download(out_dir)
```

Figure 2.3: Python code for downloading fits data.

2.2.2 Border Noise Removal

As shown in Section 2.1.1, SHARPs contain specific information of the active region to be analyzed, but in some cases they may be close to the edge of the solar disk. This edge generates noise which can affect the analysis and the obtaining of the variables of interest since it can generate higher or lower values of magnetic field than the one in the active region itself (Figure 2.5a). For this reason it was necessary to remove it and thus highlight the active region values to be obtained. To identify SHARPs that have a border, the fact that data outside the solar disk is translated as *nan* (Not a Number) or data with no value is used. If the magnetogram has any *nan*, the image is binarized so that the pixels with this value are zero and everything else is 1. Once binarized, it is required to find where the border is located, which can be only four cases: upper left, upper right, bottom left or bottom right. As an example, see Figure 2.4, where the border is situated in the bottom left position.

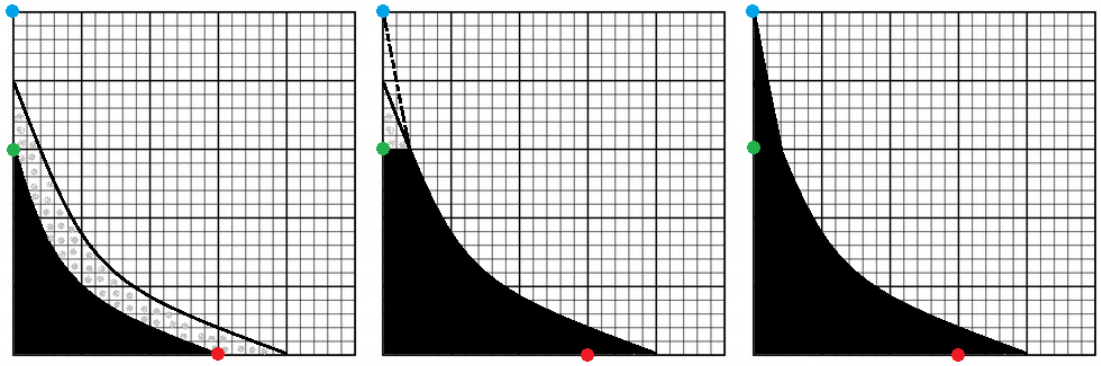

Figure 2.4: Border noise removal scheme. Details in the text.

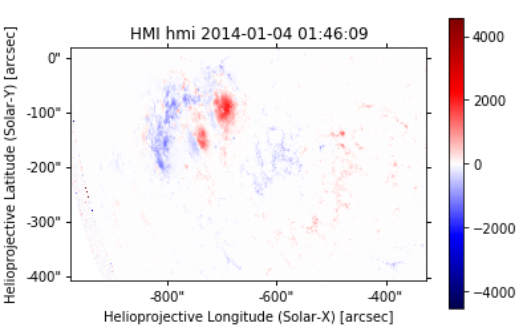

(a) Original SHARP Magnetogram.

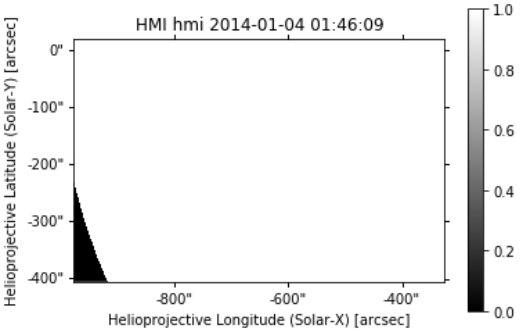

(b) Binarized SHARP Magnetogram.

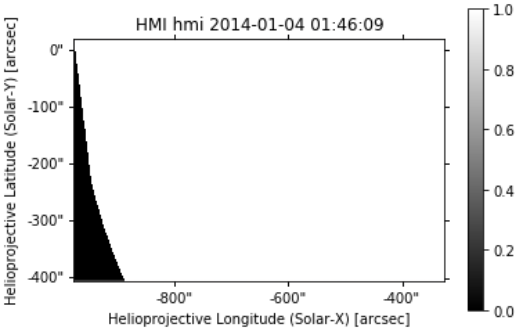

(c) Binarized SHARP Magnetogram without border noise.

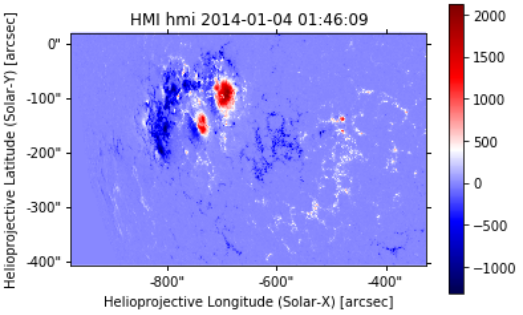

(d) Original SHARP Magnetogram without border noise.

Figure 2.5: Border noise removal for NOAA Active Region 11944.

Depending on the location, the axes that involve the edge will be taken, if we consider our example and have a look to the furthest left panel in Figure 2.4, it would be the left y axis and the bottom x axis, from where the location of the pixel with zero value in the ends of the axes will be found, this is the one that is higher in the y axis (green dot) and more to the right in the x axis (red dot). With the observation of multiple SHARPs, it is estimated that the width of the noise is approximately 60 pixels, so with the positions found, the 60 pixels to the right of these are transformed to zero like in the middle image of Figure 2.4. Now we need to transform the noise from the green dot (extreme y-axis equal to zero) to the blue dot (upper left corner not zero pixel). By locating the pixel with the upper zero value further to the right, a line is drawn to the upper left corner and transforming the values of the pixels within this triangle formed, to zero. Although it is not the exact edge of the solar disk in this last step (Figure 2.4 left), the

information that is lost is very little compared to the information that we want to obtain from the active region.

If we make this process in a SHARP magnetogram, it will look as Figure 2.5. The steps describe previously are represented from Figure 2.5b to 2.5c. Once we map the result in the Original SHARP, the Figure 2.5d will be obtain. It can be seen that the values of interest in the active region are now highlighted, also showing a notable difference between the Figure 2.5a and 2.5d, where the maximum and minimum in the magnetic field intensity change completely, giving more accurate values.

All of the above process can be executed as array manipulation in python using the *numpy* library.

2.2.3 Image resolution / Pixel rescaling

One of the specific objectives is to manipulate the resolution in order to confirm that at lower resolutions, the barycenter, therefore, the distances between them will not be affected. For this a pixel recaling will be made, that is, lower the amount of pixels that represented the original image. In Figure 2.6, an example is presented of how the manipulation is processed, with the first row from above being the image, the second row how the image is translate in a pixel frame and the last one how is perceive.

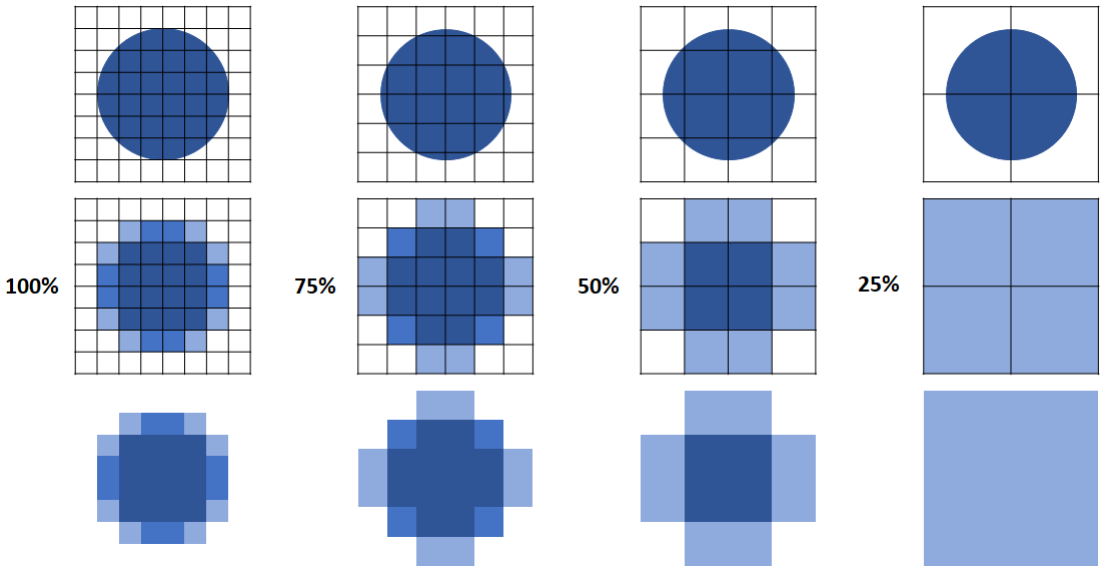

Figure 2.6: Pixel rescaling diagram

The original image will be named as to gave the 100% resolution (first column from the left), in this case, a resolution of 64 pixels. To lower the resolution to 75% the image will now be represented in a frame of 36 pixel resolution, to 50% in a frame of 16 pixel resolution and to 25% in a frame of 4 pixel resolution. To perform this process the module *rescale* from the library **skimage.transform** of python was used. In Figure 2.7 is shown this process in a magnetogram, evidencing the rescaling with the change of the axes range.

2.2.4 Image Segmentation

As one of the specific objectives is to automate the obtaining of the variables of interest, *Image Segmentation* is used, which consists of dividing a digital image into multiple segments

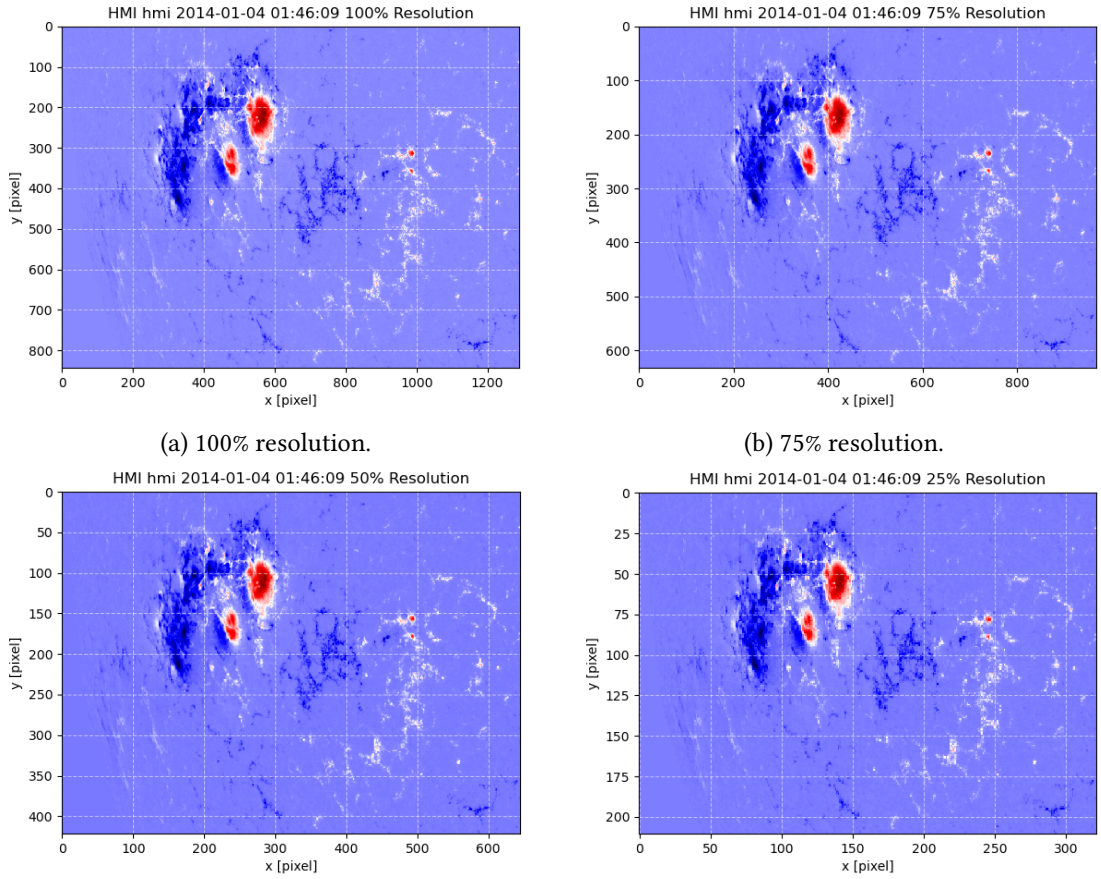

(a) 100% resolution.

(b) 75% resolution.

(c) 50% resolution.

(d) 25% resolution.

Figure 2.7: Magnetograms with different resolution.

to simplify or change the representation of the image into something more meaningful and easy to analyze. Segmentation is usually used to locate objects or boundaries in images. Image segmentation is used precisely to process assigning a label to each pixel of the image such that pixels with the same label share some characteristics.

The result of a segmented image is a set of segments that collectively will complete the image, or in this case, segments of the image will be extracted, which will be within the contours of the sunspot umbras of opposite polarity. The pixels in a region are similar in certain characteristics such as color, texture, or in the case of the umbras, magnetic field intensity.

Thresholding

One of the simplest image segmentation methods is **Thresholding**. This is based on a level or threshold value to convert a color image into a binary image. To use the method, the threshold level is selected, or in the case of active regions, there would be two threshold levels associated with positive and negative polarity. For this we will use what was found in Granados Hernández (2019), in which the best method to find the level was with the python color map *tab20*, which divides the active region into 20 levels of magnetic field intensity (in Gauss) and for the umbra the third highest level is taken for the positive spot, and the third lowest for the negative one.

SHARPs then will be treated as an image array to carry out the due segmentation process.

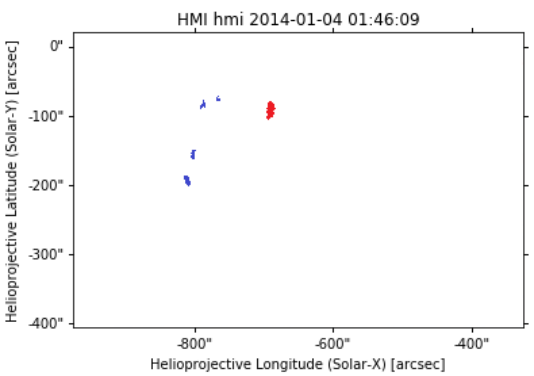

(a) Regions extracted for positive and negative umbras.

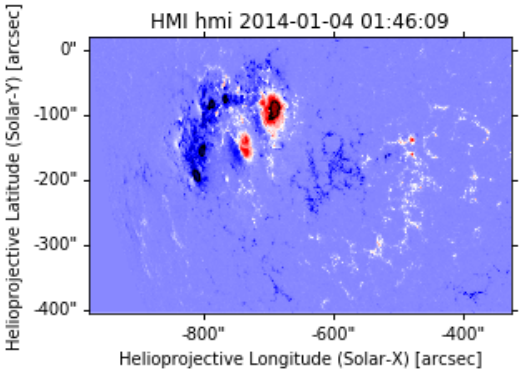

(b) Contours found from label regions in Figure 2.8a

Figure 2.8: Extraction of umbras for NOAA Active Region 11944 using thresholding.

For this, first all the values lower than the negative threshold (negative umbra) and higher than the positive threshold (positive umbra) will be mapped as zero. Then,with the module *measurements.label* from the **scipy.ndimage** library the labels will be assigned to the regions inside the thresholds (Figure 2.8a) to then find the contours of the sunspot umbras of opposite polarity (2.8b).

2.2.5 Algorithm

Initially we will have the input variables of the *Date and time of the Flare*, the *GOES class of the Flare* and the *Threshold level.*

As mentioned, one of the specific objectives is to automate the obtaining of the variables of interest (mean magnetic field, area of the opposite polarity umbras, its barycenters and the distance between them), which will be done by means of a for loop:

1. When the code is executed, it will initially obtain from the header of the .fits the size of the pixel in arcseconds and the date-time of the SHARP.
2. If the magnetogram has solar disk border, it will be removed as shown in section 2.2.2, else, it will continue with the following step.
3. Low the resolution of the magnetogram to 75%, 50% and 25% using pixel rescaling as shown in section 2.2.3.
4. Apply image segmentation: in this case the threshold is applied to the magnetogram in order to extract regions that are within this parameter. The threshold is the level at which the umbras will be determined, as shown in Figure 2.8.
5. Once the sunspots umbras are separated from the background, the following information can be calculated:
   - Mean magnetic field: B_p, B_n
   - Area of each umbra: A_p, A_n
   - Barycenters of each polarity: (x_p, y_p) , (x_n, y_n)
   - Distance between the barycenters: d_{pn}

Keeping in mind that this must be done for each resolution.

To find the area, the **scikit-image** python library can be used, which contains a collection of algorithms for image processing, in this case, the module *regionprops* which allows to measure properties of labeled image regions. To find the mean magnetic field and barycenters, from the library *scipy.ndimage*, the modules *measurements.mean* and *measurements.center_of_mass* are employed, using as parameters the labeled regions, and with the coordinates found for the barycenters, the distance can be calculated with the distance between two points (Equation 2.1).

$$d = \sqrt{(x_p - x_n)^2 + (y_p - y_n)^2} \tag{2.1}$$

where (x_p, y_p) and (x_n, y_n) are the coordinates of the barycenters of the sunspots with positive and negative polarity respectively. This equation is used since the distance between them is much smaller than the solar perimeter, so it can be approximated to a linear distance.

6. With the previous variables we will obtain the main variable, the Weighted Horizontal Magnetic Gradient WG_M with the Equation 1.21.
7. After obtaining the variables, these will be saved in this case in a .cvs file to be able to process the data more efficiently.
8. Once the .csv file is saved, it will confirm if there is any other .fits file, if there is one, it will loop over the new file, otherwise it will end.

A diagram of the flow carried out by the for loop is shown in the Figure 2.9.

Step 8 is key for future work to be able to perform the analysis of the regions in real-time, since by removing the loop closure restriction when there are no magnetograms, it will always remain active, so as soon as it detects a new .fits, it will begin to perform all the previously described analysis, and with a real-time plot, we will be able to see WG_M peaks and predict, if there is a possibility for a solar flare.

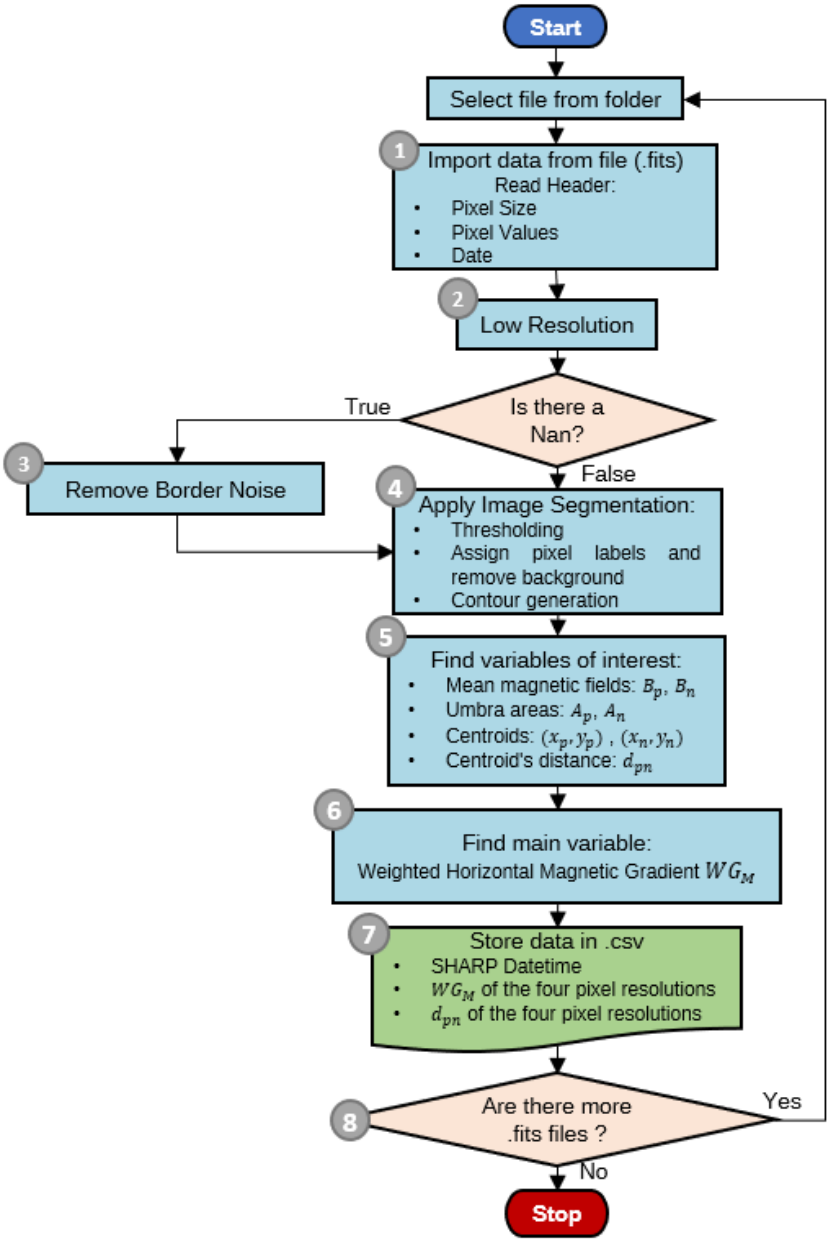

Figure 2.9: Pipeline for the analysis of solar magnetograms.

3. Data Analysis and Results

For the development of this work, magnetograms in SHARPs format from the Helioseismic and Magnetic Imager (HMI) instrument of the Solar Dynamics Observatory (SDO) were analyzed in order to study bipolar active regions by means of the method recently used by several authors (Korsós et al., 2014, 2015, 2019) to predict a time range in which solar flares can be generated.

102 active regions of the solar cycle 24 were analyzed from February 2011 to May 2019. Within these regions, 172 GOES class B, C, M and X solar flares were taken. In addition, up to four flares were analyzed for each active region. Within the sample there are 39 flares of GOES class X, 109 of M class, 12 of C class and 12 of B class.

The analysis was made with the algorithm described in section 2.2.5 and in each region the mean magnetic field, the area and the barycenters of the sunspots umbra of opposite polarity were found, together with the distance between these barycenters. Then the WG_M as shown in the equation 1.21 was calculated. Once found, we proceed to make the plots of WG_M against time. To verify the time of occurrence of the analyzed flares, the data from the National Oceanic and Atmospheric Administration (NOAA) solar flare list of GOES events in X-rays (https://hesperia.gsfc.nasa.gov/goes/goes_event_listings/) was used, in addition it is possible to extract the exact start time of a solar flare from that list.

Given the model presented in Korsós et al. (2015), it is expected to find a growth of WG_M associated with the action of approaching sunspots of opposite polarity and the creation of a current sheet between the magnetic field lines of these; then, this variable will decrease in a receding phase in which the spots separate, subsequently generating the magnetic reconnection process that produces solar flares.

The time between the maximum of WG_M and the flare will then be estimated. In addition, a statistical percentage will be found to establish a time range for the probability of occurrence of solar flares of different GOES classes, and a predictive model will be made from the relationship between the order of magnitude of the maximum of WG_M^{max} prior to the flare with the GOES class of this to predict what possible class of flare can occur.

3.1 Results Analysis

The data found is shown in the Tables A.1, B.1, C.1 and D.1 . One can see the date and maximum value of the Weighted Horizontal Magnetic Gradient WG_M^{max} for each flare and the date and flare value WG_M^{flare}. The minimum and maximum time range for the occurrence of flares of the different GOES classes for each resolution is found. These are shown in Table 3.1.

With this method it was possible to visualize the increase and decrease of WG_M by 86% of the sample. Among the data without a maximum, it is believed that in approximately 2% of the

Resolution \ GOES Class	X	M	C	B
100 % Minimum	8h 12m	48m	2h 24m	3h 12m
100 % Maximum	6d 2h 23m 59s	5d 18h 24m 02s	8d 8h 48m	5d 13h
75 % Minimum	7h 36m	36m	2h 24m	2h
75 % Maximum	8d 10h 35m 59s	6d 16h 48m	7d 22h 12m 1s	5d 12h 48m
50 % Minimum	48m	1h	2h 12m	1h 12m
50 % Maximum	6d 16h 59m 59s	6d 13h	7d 19h	5d 13h
25 % Minimum	4h 36m	24m	4h 24m	36m
25 % Maximum	8d 22h 23m 59s	5d 17h 48m 02s	8d 4h 1s	5d 16h 24m

Table 3.1: Minimum and maximum time range between the WG_M^{max} and the flare occurrence for X, M, C and B GOES class.

cases it was due to not having enough data prior to the flare manifestation to allow WG_M to increase.

It was found that after the first WG_M^{max}, the first flare occurred approximately in the time range shown in Table 3.2:

Resolution \ GOES Class	X	M	C	B
100 %	1d 22h 15m 22s	1d 13h 22m 33s	2d 12h 19m 12s	1d 12h 58m 40s
75 %	1d 23h 25m 55s	1d 16h 43m 39s	2d 11h 49m 12s	1d 11h 30m 40s
50 %	1d 23h 13m 26s	1d 15h 43m 2s	2d 9h 13m 12s	1d 11h 23m 59s
25 %	1d 20h 58m 33s	1d 10h 20m 41s	2d 10h 50m 24s	1d 10h 5m 20s

Table 3.2: Average time range of flare occurrence after the first WG_M^{max} for different GOES class and the resolutions applied.

As up to 4 flares were analyzed per active region, an average time range is found for their occurrence. The results are shown in Tables 3.3 and 3.4.

Resolution \ GOES Class	X	M	C	B
100 %	1d 15h 24m	1d 18h 48s	3d 19h 24m	2d 14h 28m
75 %	2d 6h 3m 26s	1d 21h 35m 12s	3d 18h 42m	2d 14h 36m
50 %	1d 18h 24m	1d 22h 11m 36s	3d 18h 18m	2d 14h 40m
25 %	2d 9h 13m 43s	1d 18h 13m 36s	3d 4h 24m	2d 14h 52m

Table 3.3: Average time range of second flare occurrence for different GOES class and different resolutions levels.

Resolution \ GOES Class	X_3	M_3	X_4	M_4
100 %	3d 6h 12m	1d 21h 21m 35s	3d 6h 36m	2d 3h 32m
75 %	3d 22h 26m 24s	2d 10h	4d 10h 24m	3d 3h
50 %	3d 6h 28m 47s	2d 4h 6m 20s	2d 20h 53m	3d 2h 6m
25 %	4d 4h 57m 36s	2d 3h 24m	4d 16h 5m 59s	2d 20h 8m

Table 3.4: Average time range of third and fourth (sub-indices 3 and 4) flare occurrence for GOES class X and M, and different resolutions levels.

Different temporal behaviors of WG_M were evidenced as shown below:

- Progressive and smooth growth and decrease of WG_M over time (Figure 3.1).

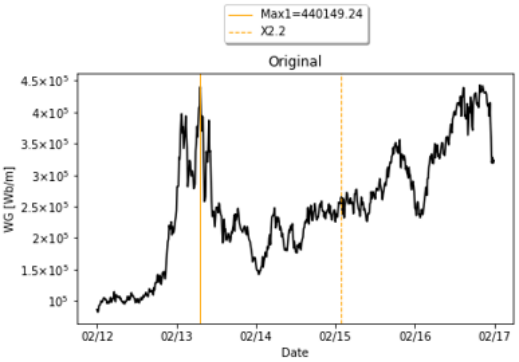

(a) WG_M vs time for NOAA AR 11158

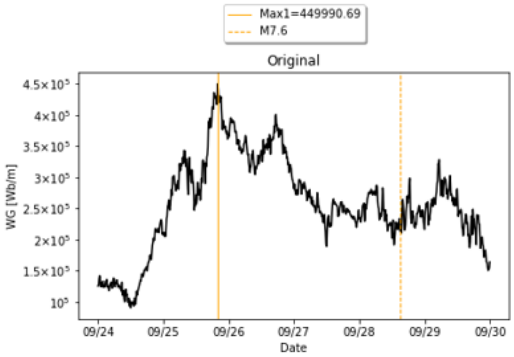

(b) WG_M vs time for NOAA AR 12422

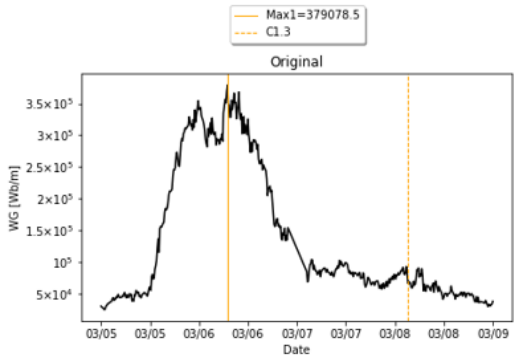

(c) WG_M vs time for NOAA AR 12734

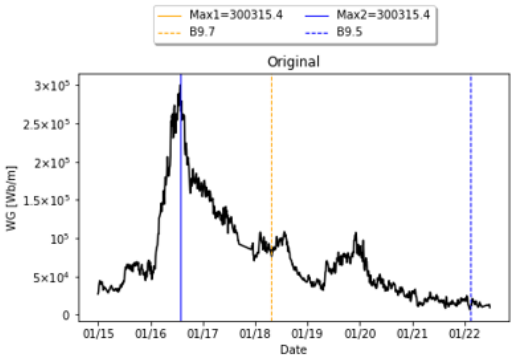

(d) WG_M vs time for NOAA AR 12696

Figure 3.1: WG_M vs time for flares of GOES Class X, M, C and B. In these events, it can be seen a smooth growth and decrease of the WG_M and next, the manifestation of a flare.

This is the behavior of WG_M most similar to that shown in Korsós et al. (2015) and Korsós et al. (2019), therefore confirming that the model works as expected.

- Sudden growth of WG_M, where the maximums are manifested as peaks prior to the formation of the flare (Figure 3.2).

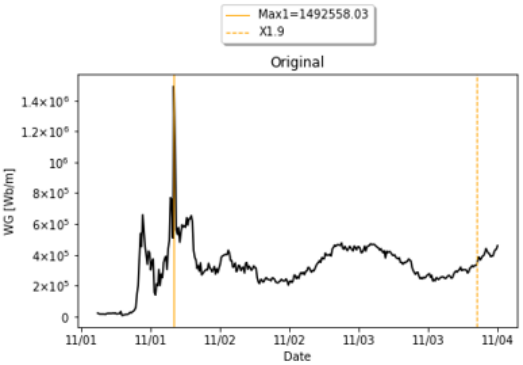

(a) WG_M vs time for NOAA AR 11339

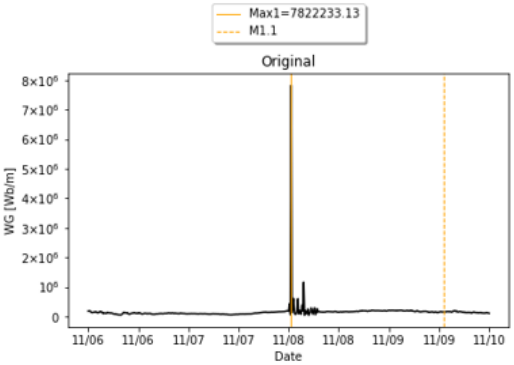

(b) WG_M vs time for NOAA AR 11342

Figure 3.2: WG_M vs time for flares of GOES Class X and M.

- Multiple WG_M^{max}: in approximately 2% of the sample, it is evidenced that for each flare of the active region there is a previous peak as shown in Figure 3.3.

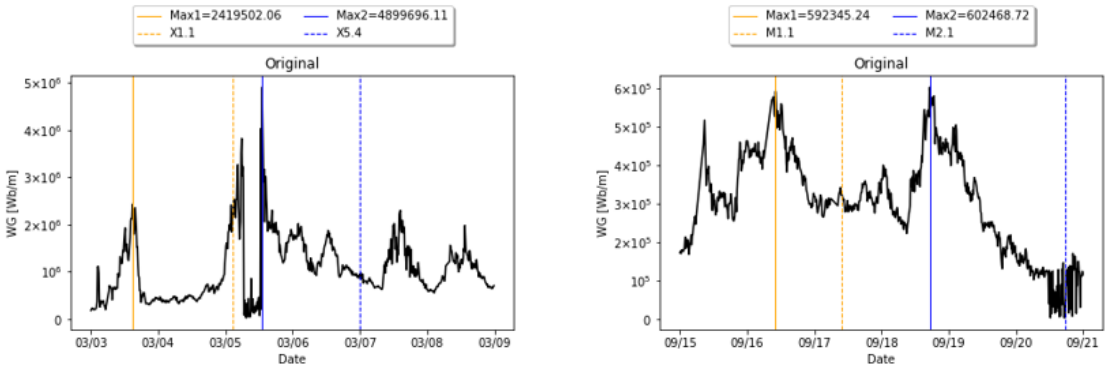

(a) WG_M vs time for NOAA AR 11429

(b) WG_M vs time for NOAA AR 12415

Figure 3.3: WG_M vs time for flares of GOES Class X and M.

The plots previously shown are all resulting from the analysis made upon magnetograms with its original resolution (100%). In all cases, regardless of how WG_M increases, the formation of a flare was evidenced after the decrease of this variable, and therefore the model works as expected.

3.1.1 Variation of WG_M with lower resolutions

The value of WG_M were also plotted for calculations over magnetograms with resolutions lower than the ones provided by HMI. The original resolution of the magnetograms was artificially lowered to test results for different resolution values in order to simulate and study the implications associated to working with magnetograms acquired with instruments under different conditions.

The following is evidenced as the resolution decreases:

- Approximately 52% the behavior of WG_M was the same in all resolutions. This means that regardless of the order of magnitude, the behavior of WG_M was similar or the same during the observation period.

  Figure 3.4 shows that the peak prior to flare was located in all resolutions at approximately the same date and time, and there were no sudden changes in the behavior of WG_M for them.

- By approximately 31% the performance of WG_M improved by decreasing the resolution. This means that the growth of this variable was more evident at lower resolution or that the maximum WG_M^{max} was generated earlier, giving a longer flare warning time.

  In Figure 3.5, it is evident that with 25% resolution a growth of WG_M is more evident, generating the maximum WG_M^{max} well in advance compared to the analysis with the 100% , 75% and 50% resolutions.

- By about 17% the behavior of WG_M is worsened as the resolution decreases. This means that the growth of this variable was more erratic in lower resolution. In detail this means that peaks of WG_M could not be evidenced or that the maximum was generated closer to the manifestation of the flare.

  In Figure 3.6, it can be seen that lowering the resolution will lead to a behavior of WG_M to be more erratic, making it more difficult to detect the growth of this variable.

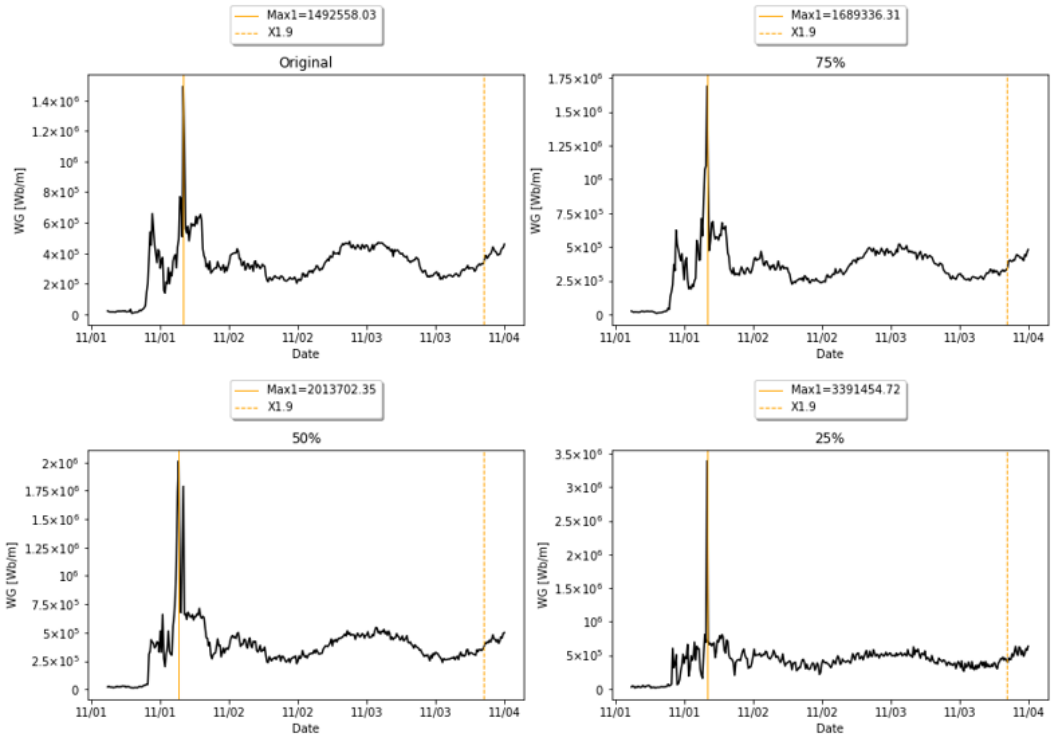

Figure 3.4: WG_M vs time for all resolutions of the NOAA AR 11339.

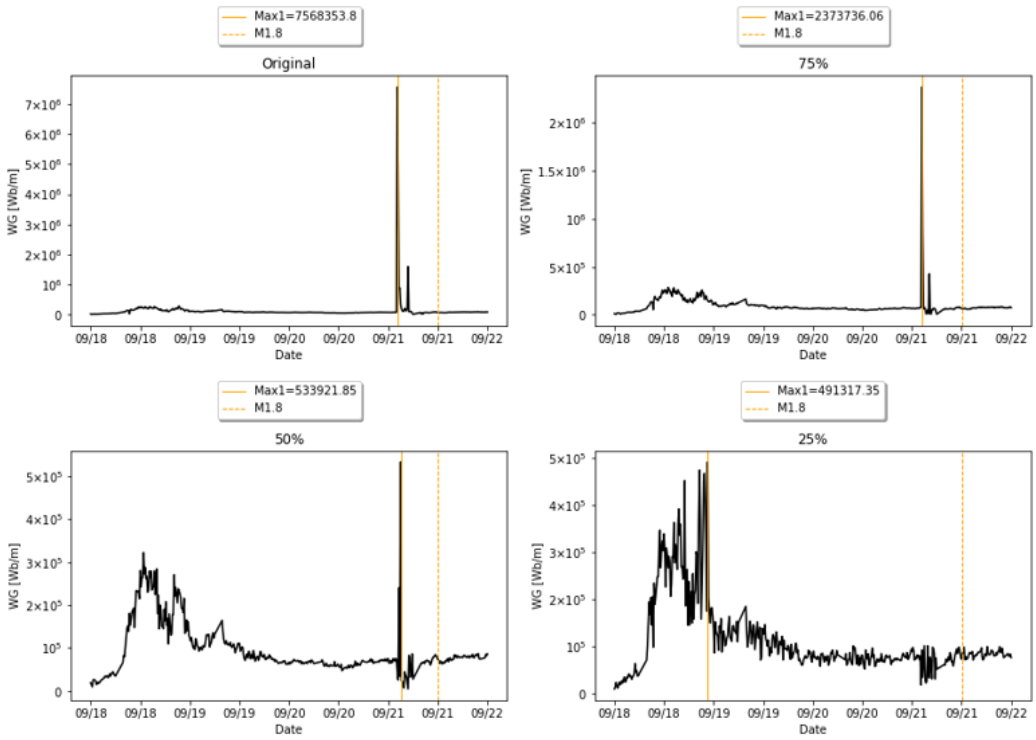

Figure 3.5: WG_M vs time for all resolutions of the NOAA AR 11301.

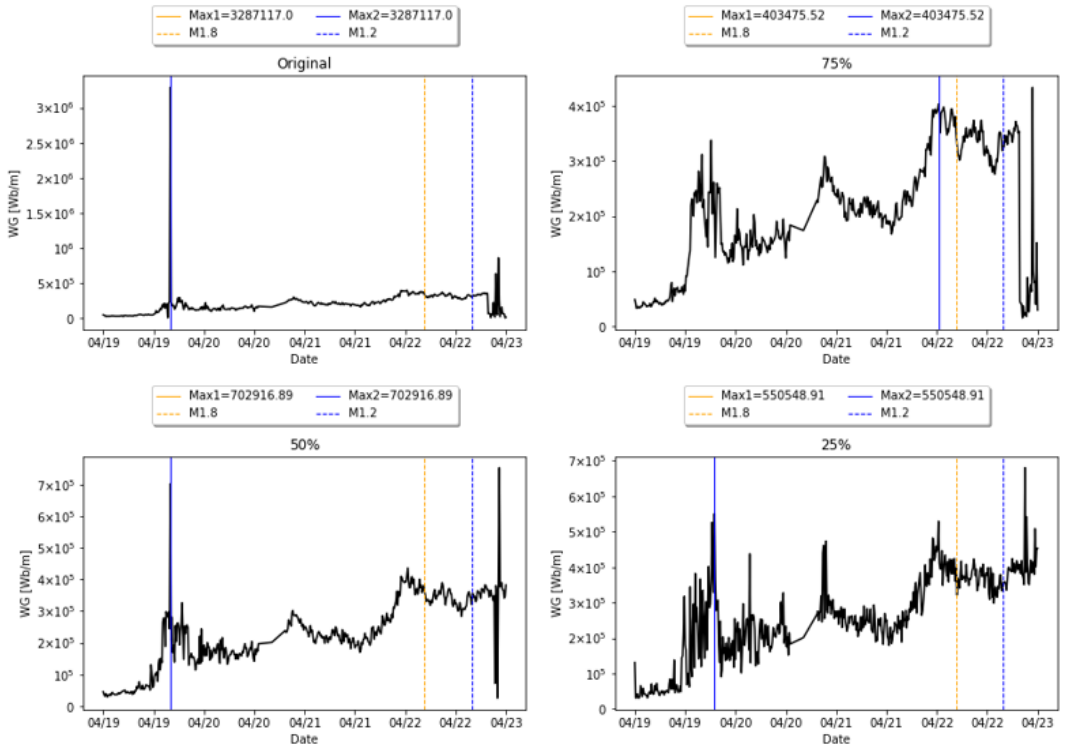

Figure 3.6: WG_M vs time for all resolutions of the NOAA AR 11195.

3.1.2 Variation of barycenters and distances with lower resolutions

Since one of the specific objectives is to verify how much the barycenters of the magnetically opposite polarity umbras change for lower magnetogram resolutions in order to confirm how the distance would be affected, a comparison scatter plot was made of the distances found for the different resolutions. As previously mentioned, the magnetogram resolutions were lowered to 75%, 50%, and 25%. In this case, it is evident that the distances are in accordance with those of the original SHARP, finding a single atypical data for the 50% resolution, with the following associated values:

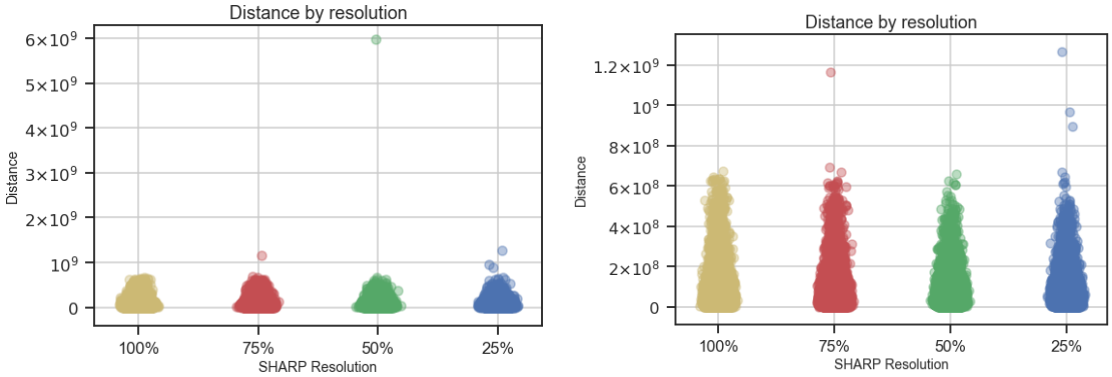

(a) Barycenter distance by resolution. A single outlier can be observed for the resolution of 50%.

(b) Distance by resolution removing atypical data for 50% resolution.

Figure 3.7: Variation of the barycenter distance with resolution, for solar magnetograms.

Its variation is shown in Figure 3.7. The graph on the left shows all the data obtained, where

$d_{100\%}$ [m]	$d_{75\%}$ [m]	$d_{50\%}$ [m]	$d_{25\%}$ [m]
1.45×10^{7}	2.59×10^{7}	5.97×10^{9}	1.84×10^{8}

Table 3.5: Atypical distance measure for the 50% resolution, along with the values for the other resolutions.

the odd data for the 50% resolution was found. If we eliminate this data, the graph on the right is therefore derived. It can be observed that the distance for lower resolution levels is consistent with that for the original magnetogram, therefore, lowering the resolutions did not significantly affect the distance measurements, being an important variable for finding WG_M.

3.1.3 Flare occurrence time

For all values of resolution, the percentage of the time of occurrence is estimated, finding the following results:

100% Resolution

<1 day	<2 days	<3 days	<4 days	<5 days	<6 days	<7 days	<8 days
34.88%	26.16%	20.35%	11.05%	1.16%	5.23%	0.58%	0.58%

Table 3.6: Time range percentage of appearance of flares per days for 100% Resolution.

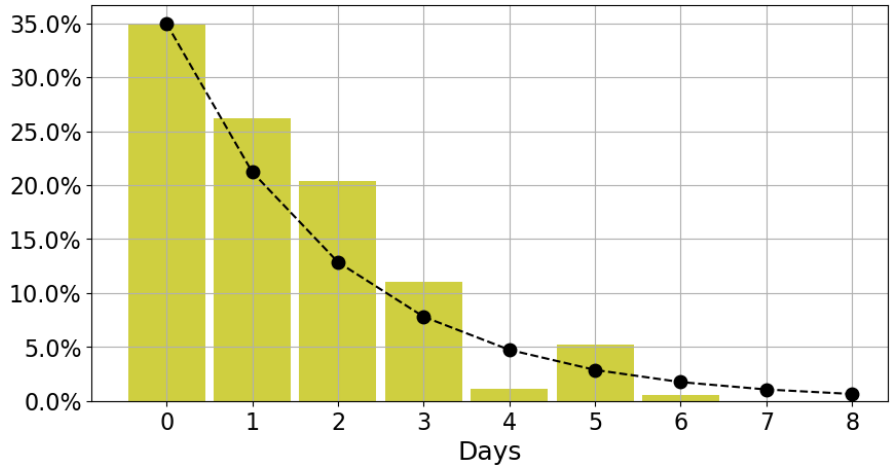

Figure 3.8: Range of time of appearance of flares per days for 100% Resolution.

75% Resolution

<1 day	<2 days	<3 days	<4 days	<5 days	<6 days	<7 days	<8 days
30.81%	25%	23.26%	9.88%	4.07%	3.49%	1.74%	1.74%

Table 3.7: Time range percentage of appearance of flares per days for 75% resolution.

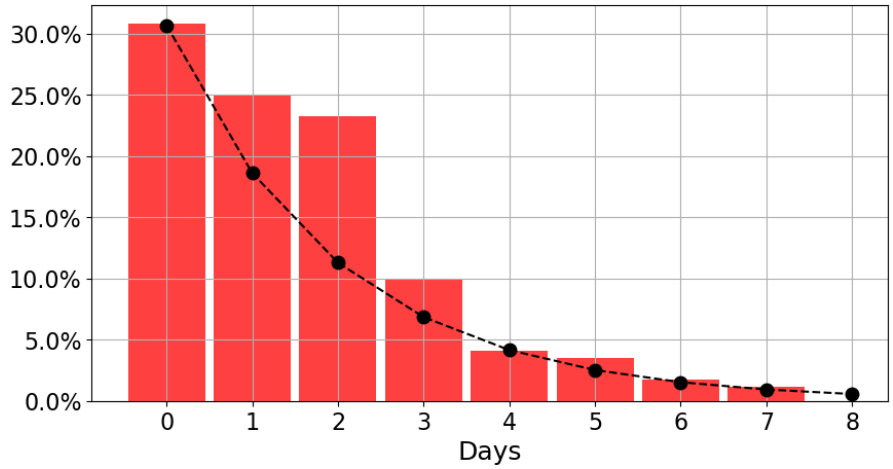

Figure 3.9: Range of time of appearance of flares per days for 75% resolution.

50% Resolution

<1 day	<2 days	<3 days	<4 days	<5 days	<6 days	<7 days	<8 days
31.4 %	27.91%	19.19%	11.05%	5.23%	2.91%	1.74%	0.58%

Table 3.8: Time range percentage of appearance of flares per days for 50% resolution.

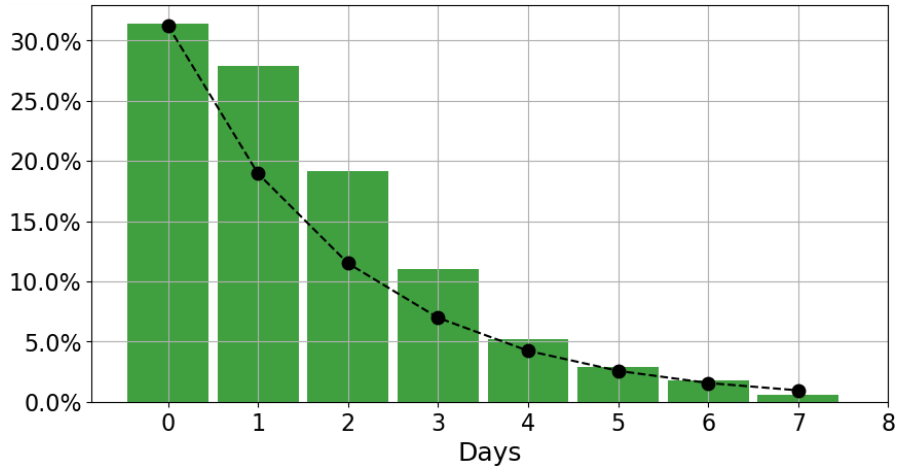

Figure 3.10: Range of time of appearance of flares per days for 50% resolution.

25% Resolution

<1 day	<2 days	<3 days	<4 days	<5 days	<6 days	<7 days	<8 days
36.05%	23.84%	22.67%	9.3 %	1.16%	4.65%	0%	2.33%

Table 3.9: Time range percentage of appearance of flares per days for 25% resolution.

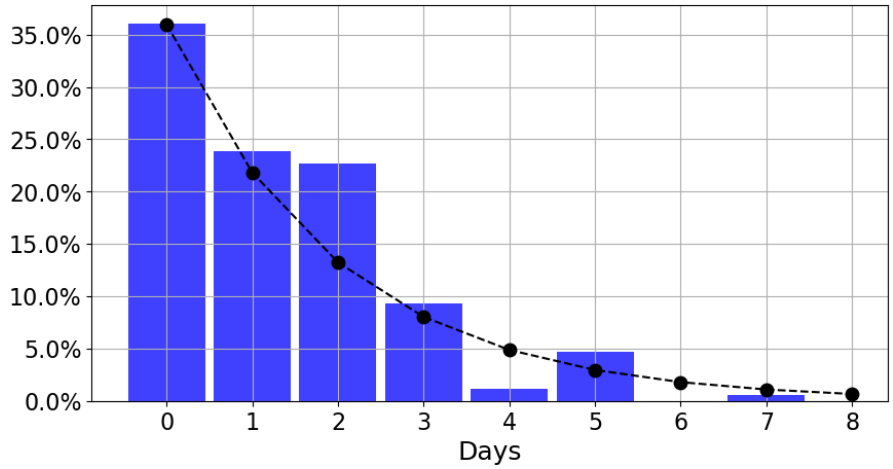

Figure 3.11: Range of time of appearance of flares per days for 25% resolution.

Therefore, with this model, the average time range of appearance of a flare after the first WG_M^{max} is most likely to happen within the next 24 to 48 hours, finding that for flares of X GOES class was approximately 1 day 22h 28 minutes, 1 day 14 hours for flares of GOES class M, 2 days 11 hours for GOES class C flares and 1 day 11 hours 29 minutes for GOES class B flares.

3.1.4 GOES Class Prediction

With the data obtained, a predictive model is created using the *Decision Tree Classifier Model*. This model is usually used in statistics, data mining and machine learning. Tree models, where the target variable can take a finite set of values, are called classification trees, it is when the predicted result is the class to which the data belongs. For the case of this work, the classification will be the GOES class of the flare and the input variable will be the order of magnitude of WG_M^{max}.

To use this prediction model, the *DecisionTreeClassifier* module of the python **sklearn** library is used. A number of 75% of the sample is used to train the model, and with this a precision of 76.74% was possible.

An example of the sample versus the prediction is shown in the Table 3.10. This short code could be implemented in a future work inside the algorithm made in section 2.2.5, giving an attempt of what could be the possible GOES class of a flare after a WG_M^{max}.

Figure 3.12 shows an example of how with this model the GOES class of the flare to happen can be obtained from the value of WG_M^{max}.

```
WG = 3.473686e+05
OM = order_of_magnitude.order_of_magnitude(WG)
variable = np.array([[WG,OM]])

print("Predicted GOES class: {}".format(ClassGoes[int(clf.predict(variable))]))
```

```
Predicted GOES class: M
```

Figure 3.12: Example code to obtain the GOES class from the WG_M^{max} previous the flare manifestation.

Prediction	X	M	M	M	M	X	M	X	M	M	M	B	B	M	M	C
Real	X	M	C	M	M	X	M	X	X	X	M	B	X	M	X	M

Prediction	X	M	M	M	X	X	M	M	C	M	M	M	M	M	M	M
Real	X	M	M	M	X	X	M	M	B	M	M	M	M	M	M	X

Prediction	B	X	M	X	M	M	M	M	M	M	M
Real	B	X	M	X	M	M	M	M	M	M	M

Table 3.10: List of solar flare class predictions compared to real data.

4. Conclusions and Discussions

The goal of this work is to develop a model that allows finding a time range in which solar flares are likely to occur, from the analysis of magnetograms of bipolar active regions. To this aim, important variables will be characterized when a flare occurs, i.e. the line-of-sight magnetic field in opposite polarity sunspot's umbras, the areas and distance between the magnetic barycenters of the umbras. An algorithm to compute such quantities was developed as explained in section 2.2.5. It is found that within the sample, the model fits expectations by approximately 86%, showing the growth and decrease of the WG_M variable prior to the occurrence of a flare. Moreover, the results are computed for different resolutions levels for magnetograms, in particular by artificially lowering the resolution to 75%, 50% and 25%.

A statistical analysis is carried out, finding that:

- Working with magnetograms at 100% resolution, for 34.88% of the cases the flare will occur within the next 24 hours, with GOES X class flares occurring after 8 hours 12 minutes, GOES M class flares 48 minutes after, GOES C class flares 2 hours 24 minutes after and GOES B class flares 3 hours 12 minutes after the maximum WG_M^{max}.
- Working with magnetograms at 75% resolution, for 30.81% of the cases the flare will occur within the next 24 hours, with GOES X class flares occurring after 7 hours 36 minutes, GOES M class flares 36 minutes after, GOES C class flares 2h 24 minutes after and GOES B class flares 2 hours after the maximum WG_M^{max}.
- Working with magnetograms at 50% resolution, for 31.4% of the cases the flare will occur within the next 24 hours, with GOES X class flares occurring after 48 minutes, GOES M class flares 1 hour after, GOES C class flares 2h 12 minutes after and GOES B class flares 36 minutes after the maximum WG_M^{max}.
- Working with magnetograms at 25% resolution, for 36.05% of the cases the flare will occur within the next 24 hours, with GOES X class flares occurring after 4h 36 minutes, GOES M class flares 24 minutes later, GOES C class flares 4h 24 minutes later and GOES B class flares 36 minutes after the maximum WG_M^{max}.

From the above, an improvement is evidenced for GOES X class flares (which are the ones likely to have the greatest impact on the Earth) in all magnetogram resolutions. The results established that the minimum time for a flare to occur for 100% resolution was around 8 hours, compared to the previous work by Granados Hernández (2019) in which the value found was 22 minutes. The minimum time range found for a flare to manifest was 48 minutes for the 50% resolution.

An average time range is found in which a flare occurs after the first WG_M^{max} for all resolutions, that is, 1 day 22h 28 minutes for GOES class X flares, 1 day 14 hours for flares of GOES class M, 2 days 11 hours for GOES class C flares and 1 day 11 hours 29 minutes for GOES class B flares.

When comparing the distances, it is evidenced that these have the same behavior as when using magnetograms with their original resolution (100%), showing that, despite the deviation of the barycenters, the variable of importance distance d_{pn} used to find the WG_M, has no significant changes. The results can be put in the context of having low resolution observations, e.g. because of the quality of the sky (seeing conditions), and still acquiring magnetograms that can be used as feasible inputs to apply the predictive method.

It is found that the threshold is a significant input variable to improve, in order to find more optimal values for the variables of interest (magnetic field in opposite polarity sunspot's umbras, the areas and distance between the magnetic barycenters of the umbras), in order to improve the behavior of WG_M. From this work, it is evident that the *Weighted Horizontal Magnetic Gradient* method stands as a good approximation for predicting the space weather associated with the occurrence of flares. The results from this work are of paramount importance for the implementation of the nodes part of SAMNet, in order to implement the method in real time with optimal results. As a future work, a user interface will be implemented to control the analysis of acquired magnetograms giving space weather alerts based on the predictions.

A. Appendix: Results for the 100% Resolution

Table A.1: Results of active regions analyzed for the SHARPs with 100% resolution. I can be seen the NOAA Active Region, the date-time of the maximum of the Weighted Horizontal Magnetic Gradient and its value WG_M previous the flare, the date-time of the flare and its value WG_M^{flare}, and in the last column the time range between the maximum of the WG_M an the flare occurrence.

NOAA AR	GOES Class	Date/time WG_M^{max}	WG_M^{max} [Wb/m]	Date-time Flare	WG_M^{flare} [Wb/m]	Time Range
11153	M 1.9	2011/02/07 23:35:53	4.30×10^{6}	2011/02/09 01:23:53	6.86×10^{5}	1d 1h 48m 0s
11158	X 2.2	2011/02/13 07:11:54	4.40×10^{5}	2011/02/15 01:47:54	2.65×10^{5}	1d 18h 36m 0s
11161	M 1.1	2011/02/15 01:35:54	8.51×10^{5}	2011/02/16 07:35:54	2.33×10^{5}	1d 6h 0m 0s
11162	M 1.0	2011/02/15 01:35:54	8.51×10^{5}	2011/02/18 10:23:54	1.94×10^{5}	3d 8h 48m 0s
	M 1.0	2011/02/15 01:35:54	8.51×10^{5}	2011/02/18 13:59:54	1.77×10^{5}	3d 12h 24m 0s
	M 1.3	2011/02/15 01:35:54	8.51×10^{5}	2011/02/18 20:59:54	1.70×10^{5}	3d 19h 24m 0s
11164	M 1.2	2011/03/06 19:23:56	6.46×10^{5}	2011/03/07 04:59:56	5.38×10^{5}	0d 9h 36m 0s
	M 1.4	2011/03/06 19:23:56	6.46×10^{5}	2011/03/07 07:59:56	5.01×10^{5}	0d 12h 36m 0s
	M 1.8	2011/03/06 19:23:56	6.46×10^{5}	2011/03/07 09:11:56	4.53×10^{5}	0d 13h 48m 0s
	M 3.7	2011/03/06 19:23:56	6.46×10^{5}	2011/03/07 19:47:56	4.49×10^{5}	1d 0h 24m 0s
11165	M 5.3	2011/03/07 01:35:56	6.96×10^{5}	2011/03/08 10:35:56	3.52×10^{5}	1d 9h 0m 0s
	M 4.4	2011/03/07 01:35:56	6.96×10^{5}	2011/03/08 18:11:56	3.00×10^{4}	1d 16h 36m 0s
11166	X 1.5	2011/03/07 11:35:56	3.69×10^{5}	2011/03/09 23:11:56	4.14×10^{5}	2d 11h 36m 0s
11169	M 4.2	2011/03/14 17:35:57	9.80×10^{5}	2011/03/14 19:35:57	6.38×10^{5}	0d 2h 0m 0s
	M 1.0	2011/03/14 17:35:57	9.80×10^{5}	2011/03/15 00:23:57	1.13×10^{5}	0d 6h 48m 0s
11176	M 1.4	2011/03/21 20:11:58	6.26×10^{5}	2011/03/23 01:59:58	1.14×10^{5}	1d 5h 48m 0s
	M 1.0	2011/03/21 20:11:58	6.26×10^{5}	2011/03/24 11:59:58	7.48×10^{4}	2d 15h 48m 0s
11190	M 1.3	2011/04/12 12:36:01	2.16×10^{6}	2011/04/15 17:00:01	3.16×10^{5}	3d 4h 24m 0s
11195	M 1.8	2011/04/19 16:00:02	3.29×10^{6}	2011/04/22 04:36:03	3.39×10^{5}	2d 12h 36m 1s
	M 1.2	2011/04/19 16:00:02	3.29×10^{6}	2011/04/22 15:48:02	3.06×10^{5}	2d 23h 48m 0s
11226	M 2.5	2011/06/07 03:48:07	2.63×10^{5}	2011/06/07 06:12:07	1.33×10^{5}	0d 2h 24m 0s
11260	M 1.1	2011/07/25 17:24:08	9.84×10^{5}	2011/07/27 15:48:08	1.18×10^{5}	1d 22h 24m 0s
11261	M 9.3	2011/07/27 23:00:08	8.13×10^{5}	2011/07/30 02:00:08	3.01×10^{5}	2d 3h 0m 0s
	M 6.0	2011/08/01 01:48:08	1.99×10^{6}	2011/08/03 13:12:07	4.49×10^{5}	2d 11h 23m 59s
	M 9.3	2011/08/01 01:48:08	1.99×10^{6}	2011/08/04 03:36:07	1.98×10^{5}	3d 1h 47m 59s
11263	X 6.9	2011/08/05 18:24:07	6.79×10^{5}	2011/08/09 07:48:07	7.65×10^{5}	3d 13h 24m 0s
11283	X 2.1	2011/09/06 06:36:04	6.94×10^{5}	2011/09/06 22:12:04	3.49×10^{5}	0d 15h 36m 0s
	X 1.8	2011/09/06 23:24:04	7.77×10^{5}	2011/09/07 22:36:04	2.57×10^{5}	0d 23h 12m 0s
11286	M 3.2	2011/09/01 18:00:04	2.21×10^{5}	2011/09/04 11:24:04	6.46×10^{4}	2d 17h 24m 0s
	M 1.6	2011/09/01 18:00:04	2.21×10^{5}	2011/09/05 04:12:04	4.50×10^{4}	3d 10h 12m 0s
	M 1.2	2011/09/01 18:00:04	2.21×10^{5}	2011/09/05 07:24:04	4.88×10^{4}	3d 13h 24m 0s
11301	M 1.8	2011/09/21 02:12:02	7.57×10^{6}	2011/09/21 12:00:02	6.85×10^{4}	0d 9h 48m 0s
11302	X 1.4	2011/09/22 10:12:02	1.39×10^{6}	2011/09/24 09:24:02	4.50×10^{3}	1d 23h 12m 0s

11305	M 1.0	2011/09/30 15:24:01	1.10×10^{6}	2011/09/30 19:00:01	6.41×10^{5}	0d 3h 36m 0s
	M 1.2	2011/09/30 15:24:01	1.10×10^{6}	2011/10/01 09:00:01	3.28×10^{5}	0d 17h 36m 0s
	M 3.9	2011/09/30 15:24:01	1.10×10^{6}	2011/10/02 00:36:01	2.44×10^{5}	1d 9h 12m 0s
11314	M 1.3	2011/10/19 11:23:58	2.41×10^{5}	2011/10/22 09:59:58	1.21×10^{4}	2d 22h 36m 0s
11319	M 1.3	2011/10/18 12:47:58	2.72×10^{5}	2011/10/21 12:47:58	8.96×10^{4}	3d 0h 0m 0s
11339	X 1.9	2011/11/01 15:59:56	1.49×10^{6}	2011/11/03 20:11:56	3.32×10^{5}	2d 4h 12m 0s
11342	M 1.1	2011/11/08 00:35:55	7.82×10^{6}	2011/11/09 12:59:55	1.55×10^{5}	1d 12h 24m 0s
11348	M 1.2	2011/11/14 03:35:55	7.59×10^{6}	2011/11/15 08:59:55	1.36×10^{5}	1d 5h 24m 0s
	M 1.1	2011/11/14 03:35:55	7.59×10^{6}	2011/11/15 22:23:55	8.17×10^{4}	1d 18h 48m 0s
11387	M 4.0	2011/12/25 15:35:52	9.32×10^{5}	2011/12/25 18:11:52	7.89×10^{5}	0d 2h 36m 0s
	M 1.5	2011/12/25 15:35:52	9.32×10^{5}	2011/12/26 02:11:52	3.57×10^{5}	0d 10h 36m 0s
	M 2.3	2011/12/25 15:35:52	9.32×10^{5}	2011/12/26 20:11:52	2.06×10^{5}	1d 4h 36m 0s
11389	M 2.0	2011/12/27 18:23:52	7.22×10^{5}	2011/12/29 21:47:52	1.27×10^{5}	2d 3h 24m 0s
	M 1.2	2011/12/27 18:23:52	7.22×10^{5}	2011/12/30 02:59:52	1.19×10^{5}	2d 8h 36m 0s
	M 2.4	2011/12/31 06:35:52	1.79×10^{6}	2011/12/31 13:11:52	2.65×10^{5}	0d 6h 36m 0s
	M 1.5	2011/12/31 06:35:52	1.79×10^{6}	2011/12/31 16:11:52	2.38×10^{5}	0d 9h 36m 0s
11401	M 1.0	2012/01/15 03:23:52	1.04×10^{6}	2012/01/17 04:35:52	1.47×10^{5}	2d 1h 12m 0s
	M 1.7	2012/01/17 12:11:52	6.33×10^{6}	2012/01/18 19:23:52	1.24×10^{5}	1d 7h 12m 0s
11402	X 1.7	2012/01/27 06:47:52	5.03×10^{5}	2012/01/27 17:35:52	1.63×10^{4}	0d 10h 48m 0s
11410	M 1.0	2012/02/04 10:23:53	3.43×10^{5}	2012/02/06 19:35:53	1.12×10^{5}	2d 9h 12m 0s
11429	X 1.1	2012/03/03 14:47:56	2.42×10^{6}	2012/03/05 02:35:56	2.24×10^{6}	1d 11h 48m 0s
	X 5.4	2012/03/05 12:59:56	4.90×10^{6}	2012/03/06 23:59:56	9.50×10^{5}	1d 11h 0m 0s
11430	X 1.3	2012/03/05 12:59:56	4.90×10^{6}	2012/03/07 00:59:56	9.39×10^{5}	1d 12h 0m 0s
11432	M 2.8	2012/03/12 15:23:57	3.60×10^{5}	2012/03/14 15:11:57	9.51×10^{4}	1d 23h 48m 0s
	M 1.8	2012/03/12 15:23:57	3.60×10^{5}	2012/03/15 08:11:57	6.28×10^{4}	2d 16h 48m 0s
11434	M 1.3	2012/03/12 02:11:56	1.57×10^{5}	2012/03/17 20:35:58	9.11×10^{4}	5d 18h 24m 2s
11520	X 1.4	2012/07/11 07:00:08	2.65×10^{6}	2012/07/12 15:36:08	1.01×10^{6}	1d 8h 36m 0s
11532	M 2.7	2012/07/26 12:24:08	4.46×10^{5}	2012/07/27 17:12:08	6.49×10^{4}	1d 4h 48m 0s
	M 6.1	2012/07/26 12:24:08	4.46×10^{5}	2012/07/28 20:48:08	9.74×10^{4}	2d 8h 24m 0s
	M 2.3	2012/07/26 12:24:08	4.46×10^{5}	2012/07/29 06:12:08	6.22×10^{4}	2d 17h 48m 0s
11748	X 1.2	2013/05/14 01:24:05	2.02×10^{6}	2013/05/15 01:24:05	2.40×10^{5}	1d 0h 0m 0s
11875	X 1.0	2013/10/27 17:23:57	7.40×10^{5}	2013/10/28 01:35:57	1.17×10^{6}	0d 8h 12m 0s
	X 2.3	2013/10/29 01:23:57	2.01×10^{6}	2013/10/29 21:47:57	1.01×10^{6}	0d 20h 24m 0s
11882	X 1.7	2013/10/24 09:11:57	2.36×10^{5}	2013/10/25 07:47:57	1.34×10^{5}	0d 22h 36m 0s
11890	X 3.3	2013/11/04 11:23:56	5.97×10^{6}	2013/11/05 22:11:56	3.05×10^{5}	1d 10h 48m 0s
	X 1.1	2013/11/04 11:23:56	5.97×10^{6}	2013/11/08 04:23:56	3.56×10^{5}	3d 17h 0m 0s
	X 1.1	2013/11/04 11:23:56	5.97×10^{6}	2013/11/10 05:11:55	3.14×10^{5}	5d 17h 47m 59s
11893	X 1.0	2013/11/16 00:59:54	3.09×10^{6}	2013/11/19 10:11:54	4.16×10^{6}	3d 9h 12m 0s
11944	X 1.2	2014/01/02 01:35:51	7.76×10^{5}	2014/01/07 17:59:52	2.92×10^{5}	5d 16h 24m 1s
11990	X 4.9	2014/02/23 23:23:55	5.85×10^{6}	2014/02/25 00:35:55	1.13×10^{5}	1d 1h 12m 0s
12017	X 1.0	2014/03/24 05:59:58	1.46×10^{5}	2014/03/29 17:35:59	1.34×10^{5}	5d 11h 36m 1s
12035	X 1.3	2014/04/24 09:48:03	7.62×10^{6}	2014/04/25 00:12:03	9.81×10^{4}	0d 14h 24m 0s
12087	X 2.2	2014/06/09 16:24:07	2.53×10^{6}	2014/06/10 11:36:08	3.40×10^{3}	0d 19h 12m 1s
	X 1.5	2014/06/09 16:24:07	2.53×10^{6}	2014/06/10 12:36:08	3.15×10^{4}	0d 20h 12m 1s
	X 1.0	2014/06/09 16:24:07	2.53×10^{6}	2014/06/11 09:00:08	9.44×10^{4}	1d 16h 36m 1s
12192	X 1.1	2014/10/16 23:23:58	7.13×10^{6}	2014/10/19 04:11:58	2.86×10^{4}	2d 4h 48m 0s
	X 1.6	2014/10/19 14:35:58	8.49×10^{6}	2014/10/22 13:59:58	6.13×10^{5}	2d 23h 24m 0s
	X 3.1	2014/10/19 14:35:58	8.49×10^{6}	2014/10/24 21:11:57	8.16×10^{5}	5d 6h 35m 59s
	X 1.0	2014/10/19 14:35:58	8.49×10^{6}	2014/10/25 16:59:57	8.67×10^{5}	6d 2h 23m 59s
12205	M 7.9	2014/11/04 23:35:56	3.58×10^{7}	2014/11/05 09:23:56	1.21×10^{6}	0d 9h 48m 0s
	M 5.4	2014/11/04 23:35:56	3.58×10^{7}	2014/11/06 03:35:56	6.42×10^{5}	1d 4h 0m 0s
	X 1.6	2014/11/04 23:35:56	3.58×10^{7}	2014/11/07 16:47:55	1.72×10^{5}	2d 17h 11m 59s
12242	X 1.8	2014/12/17 06:23:52	1.87×10^{6}	2014/12/20 00:11:52	8.68×10^{4}	2d 17h 48m 0s
12253	M 1.1	2015/01/02 14:23:52	3.62×10^{5}	2015/01/03 09:35:52	2.86×10^{5}	0d 19h 12m 0s
	M 1.3	2015/01/02 14:23:52	3.62×10^{5}	2015/01/04 15:23:52	1.78×10^{5}	2d 1h 0m 0s
12257	M 5.6	2015/01/12 22:11:52	1.02×10^{6}	2015/01/13 04:11:52	6.72×10^{4}	0d 6h 0m 0s
	M 2.2	2015/01/13 04:23:52	6.46×10^{6}	2015/01/14 12:35:52	3.27×10^{5}	1d 8h 12m 0s
12268	M 1.1	2015/01/24 07:35:52	1.21×10^{7}	2015/01/26 16:47:52	2.16×10^{5}	2d 9h 12m 0s
	M 1.4	2015/01/24 07:35:52	1.21×10^{7}	2015/01/28 04:23:52	1.39×10^{5}	3d 20h 48m 0s

	M 2.1	2015/01/24 07:35:52	1.21×10^{7}	2015/01/29 11:35:53	1.76×10^{5}	5d 4h 0m 1s
	M 2.0	2015/01/24 07:35:52	1.21×10^{7}	2015/01/30 00:35:52	2.07×10^{5}	5d 17h 0m 0s
12277	M 1.0	2015/01/27 16:59:52	4.54×10^{6}	2015/01/28 23:11:52	1.57×10^{5}	1d 6h 12m 0s
	M 2.4	2015/01/29 00:35:52	2.87×10^{7}	2015/01/30 12:11:53	1.21×10^{5}	1d 11h 36m 1s
12282	M 2.4	2015/02/07 21:11:53	4.55×10^{7}	2015/02/09 22:59:53	2.80×10^{5}	2d 1h 48m 0s
12290	M 1.0	2015/03/01 00:59:55	4.21×10^{6}	2015/03/02 06:23:56	1.38×10^{5}	1d 5h 24m 1s
	M 1.1	2015/03/02 05:35:56	4.31×10^{6}	2015/03/02 09:35:56	5.65×10^{5}	0d 4h 0m 0s
	M 3.7	2015/03/02 05:35:56	4.31×10^{6}	2015/03/02 14:23:55	3.66×10^{5}	0d 8h 47m 59s
12297	X 2.1	2015/03/08 03:11:56	7.25×10^{6}	2015/03/11 16:11:57	1.96×10^{6}	3d 13h 0m 1s
12320	M 1.4	2015/04/04 03:48:00	2.06×10^{6}	2015/04/08 14:36:01	1.46×10^{5}	4d 10h 48m 1s
12321	M 1.1	2015/04/11 16:12:01	3.16×10^{7}	2015/04/12 08:48:01	1.72×10^{5}	0d 16h 36m 0s
12322	M 4.0	2015/04/21 06:36:03	2.95×10^{6}	2015/04/21 15:24:02	2.71×10^{4}	0d 8h 47m 59s
12325	M 1.2	2015/04/19 22:12:02	9.47×10^{5}	2015/04/21 22:00:02	6.47×10^{3}	1d 23h 48m 0s
12339	X 2.7	2015/05/04 22:24:04	1.06×10^{7}	2015/05/05 22:00:04	5.20×10^{5}	0d 23h 36m 0s
12360	M 1.3	2015/06/13 02:12:08	4.59×10^{6}	2015/06/13 07:24:08	4.05×10^{5}	0d 5h 12m 0s
	M 2.0	2015/06/13 02:12:08	4.59×10^{6}	2015/06/14 00:48:08	6.77×10^{4}	0d 22h 36m 0s
12365	M 1.2	2015/06/17 19:36:08	4.98×10^{6}	2015/06/18 00:36:08	1.00×10^{5}	0d 5h 0m 0s
12367	M 3.8	2015/06/21 06:24:08	4.79×10^{5}	2015/06/21 09:36:08	2.90×10^{3}	0d 3h 12m 0s
12371	M 6.5	2015/06/20 11:24:08	5.81×10^{5}	2015/06/22 17:36:08	1.72×10^{5}	2d 6h 12m 0s
	M 7.9	2015/06/20 11:24:08	5.81×10^{5}	2015/06/25 08:00:08	3.06×10^{5}	4d 20h 36m 0s
12378	M 1.5	2015/07/02 20:24:08	6.29×10^{6}	2015/07/03 12:48:08	3.07×10^{5}	0d 16h 24m 0s
12381	M 1.7	2015/07/04 07:48:08	1.37×10^{7}	2015/07/06 20:36:08	2.49×10^{5}	2d 12h 48m 0s
12403	M 1.1	2015/08/20 10:48:06	5.18×10^{5}	2015/08/21 19:12:06	2.61×10^{5}	1d 8h 24m 0s
	M 1.2	2015/08/20 10:48:06	5.18×10^{5}	2015/08/22 06:36:06	2.33×10^{5}	1d 19h 48m 0s
	M 3.5	2015/08/20 10:48:06	5.18×10^{5}	2015/08/22 21:24:06	1.70×10^{5}	2d 10h 36m 0s
	M 5.6	2015/08/20 10:48:06	5.18×10^{5}	2015/08/24 07:24:06	3.75×10^{5}	3d 20h 36m 0s
12415	M 1.1	2015/09/16 10:12:03	5.92×10^{5}	2015/09/17 09:36:03	3.23×10^{5}	0d 23h 24m 0s
	M 2.1	2015/09/18 17:12:02	6.02×10^{5}	2015/09/20 17:36:02	8.77×10^{3}	2d 0h 24m 0s
12422	M 7.6	2015/09/25 20:00:01	4.50×10^{5}	2015/09/28 14:48:01	2.34×10^{5}	2d 18h 48m 0s
12423	M 3.6	2015/09/27 04:36:01	6.16×10^{5}	2015/09/28 03:48:01	3.63×10^{5}	0d 23h 12m 0s
	M 1.2	2015/09/28 02:12:01	1.46×10^{6}	2015/09/29 03:12:01	4.89×10^{5}	1d 1h 0m 0s
	M 1.2	2015/09/29 02:48:01	4.85×10^{6}	2015/09/29 05:36:01	9.12×10^{4}	0d 2h 48m 0s
	M 1.3	2015/09/29 02:48:01	4.85×10^{6}	2015/09/29 08:48:01	2.47×10^{5}	0d 6h 0m 0s
12434	M 1.1	2015/10/15 08:11:59	6.30×10^{6}	2015/10/15 23:23:59	1.38×10^{4}	0d 15h 12m 0s
	M 1.1	2015/10/15 08:11:59	6.30×10^{6}	2015/10/16 06:11:59	3.03×10^{4}	0d 22h 0m 0s
12437	M 1.5	2015/10/17 16:23:58	9.88×10^{6}	2015/10/17 20:35:58	8.96×10^{6}	0d 4h 12m 0s
12443	M 3.7	2015/11/01 01:47:56	3.00×10^{5}	2015/11/04 13:35:56	1.52×10^{5}	3d 11h 48m 0s
12445	M 2.5	2015/11/04 04:23:56	3.50×10^{6}	2015/11/04 11:59:56	1.30×10^{4}	0d 7h 36m 0s
12449	M 3.9	2015/11/07 16:11:55	1.01×10^{7}	2015/11/09 12:47:55	1.95×10^{5}	1d 20h 36m 0s
12473	M 1.6	2015/12/21 09:47:52	9.90×10^{6}	2015/12/22 03:11:52	5.89×10^{5}	0d 17h 24m 0s
	M 4.7	2015/12/22 11:23:52	1.90×10^{7}	2015/12/23 00:23:52	2.20×10^{5}	0d 13h 0m 0s
	M 1.1	2015/12/22 11:23:52	1.90×10^{7}	2015/12/24 01:47:52	3.50×10^{5}	1d 14h 24m 0s
12497	M 1.0	2016/02/12 09:47:54	3.57×10^{5}	2016/02/12 10:35:54	3.46×10^{5}	0d 0h 48m 0s
	M 1.8	2016/02/12 20:11:53	9.08×10^{5}	2016/02/13 15:11:54	2.00×10^{6}	0d 19h 0m 1s
	M 1.0	2016/02/13 18:59:54	4.07×10^{7}	2016/02/14 19:23:54	1.48×10^{5}	1d 0h 24m 0s
	M 1.1	2016/02/13 18:59:54	4.07×10^{7}	2016/02/15 10:35:54	4.83×10^{3}	1d 15h 36m 0s
12529	M 6.7	2016/04/15 14:36:02	5.47×10^{5}	2016/04/18 00:12:02	1.89×10^{5}	2d 9h 36m 0s
12567	M 7.6	2016/07/19 17:24:08	4.28×10^{5}	2016/07/23 05:00:08	2.79×10^{5}	3d 11h 36m 0s
12644	M 5.3	2017/04/02 01:47:00	3.39×10^{5}	2017/04/02 07:47:00	5.12×10^{4}	0d 6h 0m 0s
	M 5.7	2017/04/02 13:35:00	1.77×10^{6}	2017/04/02 20:23:00	2.47×10^{4}	0d 6h 48m 0s
	M 5.8	2017/04/02 13:35:00	1.77×10^{6}	2017/04/03 14:23:00	1.94×10^{4}	1d 0h 48m 0s
12665	M 1.3	2017/07/06 10:48:08	5.18×10^{6}	2017/07/09 03:12:08	4.87×10^{5}	2d 16h 24m 0s
12673	X 2.2	2017/09/05 19:12:04	1.92×10^{6}	2017/09/06 09:00:04	1.17×10^{6}	0d 13h 48m 0s
	X 9.3	2017/09/05 19:12:04	1.92×10^{6}	2017/09/06 11:48:04	8.29×10^{5}	0d 16h 36m 0s
	X 1.3	2017/09/06 17:36:04	2.10×10^{6}	2017/09/07 14:24:04	7.33×10^{5}	0d 20h 48m 0s
	X 8.2	2017/09/10 00:24:03	9.28×10^{6}	2017/09/10 11:12:03	4.10×10^{5}	0d 10h 48m 0s
12696	B 9.7	2018/01/16 13:35:52	3.00×10^{5}	2018/01/18 07:23:52	7.98×10^{4}	1d 17h 48m 0s
	B 9.5	2018/01/16 13:35:52	3.00×10^{5}	2018/01/22 02:35:52	6.86×10^{3}	5d 13h 0m 0s

12699	C 8.1	2018/02/05 01:59:53	5.01×10^{6}	2018/02/07 13:35:53	2.19×10^{5}	2d 11h 36m 0s
12700	C 1.9	2018/03/02 04:59:56	2.63×10^{5}	2018/03/02 10:59:56	3.33×10^{4}	0d 6h 0m 0s
12703	B 9.0	2018/03/29 21:47:00	1.41×10^{6}	2018/04/01 12:47:00	3.95×10^{4}	2d 15h 0m 0s
12704	B 1.0	2018/04/12 19:24:01	1.37×10^{5}	2018/04/14 00:12:01	3.09×10^{4}	1d 4h 48m 0s
12710	B 9.8	2018/05/21 08:00:06	1.98×10^{6}	2018/05/24 12:24:06	3.09×10^{4}	3d 4h 24m 0s
12712	C 2.7	2018/05/24 18:36:06	6.26×10^{6}	2018/05/28 17:00:07	1.11×10^{5}	3d 22h 24m 1s
12713	B 4.7	2018/06/23 07:00:08	3.84×10^{5}	2018/06/23 14:36:08	2.02×10^{5}	0d 7h 36m 0s
12714	B 1.0	2018/06/18 23:12:08	1.10×10^{5}	2018/06/19 02:24:08	7.33×10^{4}	0d 3h 12m 0s
	B 1.8	2018/06/19 13:12:08	2.14×10^{5}	2018/06/20 00:00:08	1.39×10^{5}	0d 10h 48m 0s
12715	C 2.1	2018/06/20 03:36:08	3.32×10^{5}	2018/06/21 01:12:08	3.48×10^{5}	0d 21h 36m 0s
12719	B 1.6	2018/08/23 02:48:06	1.08×10^{7}	2018/08/24 21:48:05	9.78×10^{4}	1d 18h 59m 59s
12729	B 2.4	2018/12/08 19:59:52	1.33×10^{7}	2018/12/09 06:59:53	1.00×10^{5}	0d 11h 0m 1s
12732	C 1.6	2019/01/06 08:11:52	3.42×10^{6}	2019/01/06 10:35:52	3.84×10^{5}	0d 2h 24m 0s
12733	C 5.0	2019/01/23 04:35:52	1.78×10^{5}	2019/01/26 13:11:52	1.43×10^{5}	3d 8h 36m 0s
12734	C 1.3	2019/03/06 06:59:56	3.79×10^{5}	2019/03/08 03:11:56	6.68×10^{4}	1d 20h 12m 0s
12736	C 4.8	2019/03/18 14:59:58	1.82×10^{5}	2019/03/20 10:35:58	1.76×10^{5}	1d 19h 36m 0s
	C 5.6	2019/03/18 14:59:58	1.82×10^{5}	2019/03/21 03:11:58	2.44×10^{5}	2d 12h 12m 0s
12738	B 7.1	2019/04/10 01:24:01	3.26×10^{5}	2019/04/12 11:24:01	1.23×10^{5}	2d 10h 0m 0s
	B 8.1	2019/04/18 04:48:02	2.80×10^{6}	2019/04/20 00:24:02	7.55×10^{4}	1d 19h 36m 0s
12740	C 9.9	2019/05/04 03:00:04	4.69×10^{6}	2019/05/06 05:00:04	3.84×10^{5}	2d 2h 0m 0s
	C 6.7	2019/05/04 03:00:04	4.69×10^{6}	2019/05/09 05:36:05	1.34×10^{5}	5d 2h 36m 1s
12741	C 2.0	2019/05/07 10:24:05	4.02×10^{6}	2019/05/15 19:12:05	2.19×10^{5}	8d 8h 48m 0s

B. Appendix: Results for the 75% Resolution

Table B.1: Results of active regions analyzed for the SHARPs with 75% resolution. I can be seen the NOAA Active Region, the date-time of the maximum of the Weighted Horizontal Magnetic Gradient and its value WG_M previous the flare, the date-time of the flare and its value WG_M^{flare}, and in the last column the time range between the maximum of the WG_M an the flare occurrence.

NOAA AR	GOES Class	Date-time WG_M^{max}	WG_M^{max} [Wb/m]	Date-time Flare	WG_M^{flare} [Wb/m]	Time Range
11153	M 1.9	2011/02/07 23:47:53	1.11×10^{6}	2011/02/09 01:23:53	6.88×10^{5}	1d 1h 36m 0s
11158	X 2.2	2011/02/13 07:11:54	4.40×10^{5}	2011/02/15 01:47:54	2.72×10^{5}	1d 18h 36m 0s
11161	M 1.1	2011/02/15 21:59:54	3.11×10^{5}	2011/02/16 07:35:54	2.33×10^{5}	0d 9h 36m 0s
11162	M 1.0	2011/02/15 21:59:54	3.11×10^{5}	2011/02/18 10:23:54	2.00×10^{5}	2d 12h 24m 0s
	M 1.0	2011/02/15 21:59:54	3.11×10^{5}	2011/02/18 13:59:54	1.78×10^{5}	2d 16h 0m 0s
	M 1.3	2011/02/15 21:59:54	3.11×10^{5}	2011/02/18 20:59:54	1.71×10^{5}	2d 23h 0m 0s
11164	M 1.2	2011/03/06 19:35:56	6.52×10^{5}	2011/03/07 04:59:56	5.53×10^{5}	0d 9h 24m 0s
	M 1.4	2011/03/06 19:35:56	6.52×10^{5}	2011/03/07 07:59:56	5.07×10^{5}	0d 12h 24m 0s
	M 1.8	2011/03/06 19:35:56	6.52×10^{5}	2011/03/07 09:11:56	4.48×10^{5}	0d 13h 36m 0s
	M 3.7	2011/03/06 19:35:56	6.52×10^{5}	2011/03/07 19:47:56	4.51×10^{5}	1d 0h 12m 0s
11165	M 5.3	2011/03/07 02:47:56	7.90×10^{5}	2011/03/08 10:35:56	3.55×10^{5}	1d 7h 48m 0s
	M 4.4	2011/03/07 02:47:56	7.90×10^{5}	2011/03/08 18:11:56	2.50×10^{4}	1d 15h 24m 0s
11166	X 1.5	2011/03/07 11:35:56	3.67×10^{5}	2011/03/09 23:11:56	4.11×10^{5}	2d 11h 36m 0s
11169	M 4.2	2011/03/14 18:35:57	1.08×10^{6}	2011/03/14 19:35:57	6.44×10^{5}	0d 1h 0m 0s
	M 1.0	2011/03/14 18:35:57	1.08×10^{6}	2011/03/15 00:23:57	1.31×10^{5}	0d 5h 48m 0s
11176	M 1.4	2011/03/21 22:23:58	6.35×10^{5}	2011/03/23 01:59:58	1.19×10^{5}	1d 3h 36m 0s
	M 1.0	2011/03/21 22:23:58	6.35×10^{5}	2011/03/24 11:59:58	7.78×10^{4}	2d 13h 36m 0s
11190	M 1.3	2011/04/12 07:48:01	2.96×10^{6}	2011/04/15 17:00:01	3.23×10^{5}	3d 9h 12m 0s
11195	M 1.8	2011/04/22 00:24:02	4.03×10^{5}	2011/04/22 04:36:03	3.50×10^{5}	0d 4h 12m 1s
	M 1.2	2011/04/22 00:24:02	4.03×10^{5}	2011/04/22 15:48:02	3.25×10^{5}	0d 15h 24m 0s
11226	M 2.5	2011/06/07 03:48:07	2.82×10^{5}	2011/06/07 06:12:07	1.32×10^{5}	0d 2h 24m 0s
11260	M 1.1	2011/07/26 01:24:08	6.72×10^{5}	2011/07/27 15:48:08	1.24×10^{5}	1d 14h 24m 0s
11261	M 9.3	2011/07/27 00:48:08	6.46×10^{5}	2011/07/30 02:00:08	3.15×10^{5}	3d 1h 12m 0s
	M 6.0	2011/08/01 01:48:08	1.99×10^{6}	2011/08/03 13:12:07	4.96×10^{5}	2d 11h 23m 59s
	M 9.3	2011/08/01 01:48:08	1.99×10^{6}	2011/08/04 03:36:07	2.02×10^{5}	3d 1h 47m 59s
11263	X 6.9	2011/08/05 18:24:07	6.90×10^{5}	2011/08/09 07:48:07	7.44×10^{5}	3d 13h 24m 0s
11283	X 2.1	2011/09/06 06:36:04	7.05×10^{5}	2011/09/06 22:12:04	4.13×10^{5}	0d 15h 36m 0s
	X 1.8	2011/09/07 00:00:04	8.55×10^{5}	2011/09/07 22:36:04	2.59×10^{5}	0d 22h 36m 0s
11286	M 3.2	2011/09/01 17:36:04	2.26×10^{5}	2011/09/04 11:24:04	8.14×10^{4}	2d 17h 48m 0s
	M 1.6	2011/09/01 17:36:04	2.26×10^{5}	2011/09/05 04:12:04	4.96×10^{4}	3d 10h 36m 0s
	M 1.2	2011/09/01 17:36:04	2.26×10^{5}	2011/09/05 07:24:04	4.98×10^{4}	3d 13h 48m 0s
11301	M 1.8	2011/09/21 02:24:02	2.37×10^{6}	2011/09/21 12:00:02	6.80×10^{4}	0d 9h 36m 0s
11302	X 1.4	2011/09/22 10:48:02	1.44×10^{6}	2011/09/24 09:24:02	1.34×10^{5}	1d 22h 36m 0s

11305	M 1.0	2011/09/30 15:24:01	1.10×10^{6}	2011/09/30 19:00:01	6.38×10^{5}	0d 3h 36m 0s
	M 1.2	2011/09/30 15:24:01	1.10×10^{6}	2011/10/01 09:00:01	3.35×10^{5}	0d 17h 36m 0s
	M 3.9	2011/09/30 15:24:01	1.10×10^{6}	2011/10/02 00:36:01	2.44×10^{5}	1d 9h 12m 0s
11314	M 1.3	2011/10/19 11:23:58	2.39×10^{5}	2011/10/22 09:59:58	1.34×10^{4}	2d 22h 36m 0s
11319	M 1.3	2011/10/18 14:11:58	2.80×10^{5}	2011/10/21 12:47:58	1.02×10^{5}	2d 22h 36m 0s
11339	X 1.9	2011/11/01 15:59:56	1.69×10^{6}	2011/11/03 20:11:56	3.33×10^{5}	2d 4h 12m 0s
11342	M 1.1	2011/11/08 00:11:55	5.47×10^{5}	2011/11/09 12:59:55	1.54×10^{5}	1d 12h 48m 0s
11348	M 1.2	2011/11/14 03:35:55	7.09×10^{6}	2011/11/15 08:59:55	1.21×10^{5}	1d 5h 24m 0s
	M 1.1	2011/11/14 03:35:55	7.09×10^{6}	2011/11/15 22:23:55	8.95×10^{4}	1d 18h 48m 0s
11387	M 4.0	2011/12/25 15:47:52	9.09×10^{5}	2011/12/25 18:11:52	8.42×10^{5}	0d 2h 24m 0s
	M 1.5	2011/12/25 15:47:52	9.09×10^{5}	2011/12/26 02:11:52	3.80×10^{5}	0d 10h 24m 0s
	M 2.3	2011/12/25 15:47:52	9.09×10^{5}	2011/12/26 20:11:52	2.13×10^{5}	1d 4h 24m 0s
11389	M 2.0	2011/12/27 13:59:52	1.06×10^{6}	2011/12/29 21:47:52	1.38×10^{5}	2d 7h 48m 0s
	M 1.2	2011/12/27 13:59:52	1.06×10^{6}	2011/12/30 02:59:52	1.23×10^{5}	2d 13h 0m 0s
	M 2.4	2011/12/27 13:59:52	1.06×10^{6}	2011/12/31 13:11:52	2.53×10^{5}	3d 23h 12m 0s
	M 1.5	2011/12/27 13:59:52	1.06×10^{6}	2011/12/31 16:11:52	2.47×10^{5}	4d 2h 12m 0s
11401	M 1.0	2012/01/16 05:11:52	5.61×10^{5}	2012/01/17 04:35:52	1.53×10^{5}	0d 23h 24m 0s
	M 1.7	2012/01/16 05:11:52	5.61×10^{5}	2012/01/18 19:23:52	2.83×10^{4}	2d 14h 12m 0s
11402	X 1.7	2012/01/26 09:59:52	5.02×10^{5}	2012/01/27 17:35:52	5.00×10^{4}	1d 7h 36m 0s
11410	M 1.0	2012/02/04 10:23:53	3.46×10^{5}	2012/02/06 19:35:53	1.01×10^{5}	2d 9h 12m 0s
11429	X 1.1	2012/03/03 14:59:56	2.91×10^{6}	2012/03/05 02:35:56	2.43×10^{6}	1d 11h 36m 0s
	X 5.4	2012/03/05 05:47:56	4.50×10^{6}	2012/03/06 23:59:56	9.44×10^{5}	1d 18h 12m 0s
11430	X 1.3	2012/03/05 05:47:56	4.50×10^{6}	2012/03/07 00:59:56	9.39×10^{5}	1d 19h 12m 0s
11432	M 2.8	2012/03/12 19:11:57	3.42×10^{5}	2012/03/14 15:11:57	9.22×10^{4}	1d 20h 0m 0s
	M 1.8	2012/03/12 19:11:57	3.42×10^{5}	2012/03/15 08:11:57	6.79×10^{4}	2d 13h 0m 0s
11434	M 1.3	2012/03/12 02:11:56	1.60×10^{5}	2012/03/17 20:35:58	9.16×10^{4}	5d 18h 24m 2s
11520	X 1.4	2012/07/09 02:36:08	6.12×10^{6}	2012/07/12 15:36:08	1.00×10^{6}	3d 13h 0m 0s
11532	M 2.7	2012/07/26 03:00:08	2.38×10^{5}	2012/07/27 17:12:08	6.98×10^{4}	1d 14h 12m 0s
	M 6.1	2012/07/26 03:00:08	2.38×10^{5}	2012/07/28 20:48:08	9.61×10^{4}	2d 17h 48m 0s
	M 2.3	2012/07/26 03:00:08	2.38×10^{5}	2012/07/29 06:12:08	6.13×10^{4}	3d 3h 12m 0s
11748	X 1.2	2013/05/14 01:36:05	1.82×10^{6}	2013/05/15 01:24:05	2.45×10^{5}	0d 23h 48m 0s
11875	X 1.0	2013/10/27 17:23:57	7.68×10^{5}	2013/10/28 01:35:57	3.76×10^{4}	0d 8h 12m 0s
	X 2.3	2013/10/28 08:23:57	1.68×10^{6}	2013/10/29 21:47:57	3.77×10^{6}	1d 13h 24m 0s
11882	X 1.7	2013/10/24 09:23:57	2.45×10^{5}	2013/10/25 07:47:57	1.23×10^{5}	0d 22h 24m 0s
11890	X 3.3	2013/11/03 12:23:56	1.03×10^{6}	2013/11/05 22:11:56	3.33×10^{5}	2d 9h 48m 0s
	X 1.1	2013/11/03 12:23:56	1.03×10^{6}	2013/11/08 04:23:56	3.53×10^{5}	4d 16h 0m 0s
	X 1.1	2013/11/03 12:23:56	1.03×10^{6}	2013/11/10 05:11:55	3.25×10^{5}	6d 16h 47m 59s
11893	X 1.0	2013/11/16 00:59:54	3.15×10^{6}	2013/11/19 10:11:54	3.75×10^{6}	3d 9h 12m 0s
11944	X 1.2	2014/01/02 01:35:51	7.98×10^{5}	2014/01/07 17:59:52	2.95×10^{5}	5d 16h 24m 1s
11990	X 4.9	2014/02/23 22:11:55	2.66×10^{6}	2014/02/25 00:35:55	1.88×10^{4}	1d 2h 24m 0s
12017	X 1.0	2014/03/24 06:59:58	1.48×10^{5}	2014/03/29 17:35:59	1.39×10^{5}	5d 10h 36m 1s
12035	X 1.3	2014/04/24 16:36:03	3.47×10^{6}	2014/04/25 00:12:03	1.87×10^{4}	0d 7h 36m 0s
12087	X 2.2	2014/06/09 16:36:07	8.57×10^{5}	2014/06/10 11:36:08	6.71×10^{2}	0d 19h 0m 1s
	X 1.5	2014/06/09 16:36:07	8.57×10^{5}	2014/06/10 12:36:08	1.17×10^{4}	0d 20h 0m 1s
	X 1.0	2014/06/09 16:36:07	8.57×10^{5}	2014/06/11 09:00:08	2.62×10^{4}	1d 16h 24m 1s
12192	X 1.1	2014/10/17 06:23:58	7.19×10^{6}	2014/10/19 04:11:58	8.76×10^{3}	1d 21h 48m 0s
	X 1.6	2014/10/17 06:23:58	7.19×10^{6}	2014/10/22 13:59:58	6.79×10^{5}	5d 7h 36m 0s
	X 3.1	2014/10/17 06:23:58	7.19×10^{6}	2014/10/24 21:11:57	7.76×10^{5}	7d 14h 47m 59s
	X 1.0	2014/10/17 06:23:58	7.19×10^{6}	2014/10/25 16:59:57	8.64×10^{5}	8d 10h 35m 59s
12205	M 7.9	2014/11/04 03:47:56	2.34×10^{6}	2014/11/05 09:23:56	3.53×10^{4}	1d 5h 36m 0s
	M 5.4	2014/11/05 19:47:56	8.58×10^{6}	2014/11/06 03:35:56	1.71×10^{5}	0d 7h 48m 0s
	X 1.6	2014/11/05 19:47:56	8.58×10^{6}	2014/11/07 16:47:55	1.81×10^{5}	1d 20h 59m 59s
12242	X 1.8	2014/12/17 06:11:52	1.81×10^{6}	2014/12/20 00:11:52	1.64×10^{5}	2d 18h 0m 0s
12253	M 1.1	2015/01/02 14:11:52	3.74×10^{5}	2015/01/03 09:35:52	2.93×10^{5}	0d 19h 24m 0s
	M 1.3	2015/01/02 14:11:52	3.74×10^{5}	2015/01/04 15:23:52	1.83×10^{5}	2d 1h 12m 0s
12257	M 5.6	2015/01/09 23:59:51	5.48×10^{5}	2015/01/13 04:11:52	1.24×10^{4}	3d 4h 12m 1s
	M 2.2	2015/01/14 09:23:52	3.67×10^{6}	2015/01/14 12:35:52	9.57×10^{4}	0d 3h 12m 0s
12268	M 1.1	2015/01/23 07:47:52	5.32×10^{6}	2015/01/26 16:47:52	2.19×10^{5}	3d 9h 0m 0s
	M 1.4	2015/01/23 07:47:52	5.32×10^{6}	2015/01/28 04:23:52	1.45×10^{5}	4d 20h 36m 0s

	M 2.1	2015/01/23 07:47:52	5.32×10^{6}	2015/01/29 11:35:53	1.82×10^{5}	6d 3h 48m 1s
	M 2.0	2015/01/23 07:47:52	5.32×10^{6}	2015/01/30 00:35:52	2.12×10^{5}	6d 16h 48m 0s
12277	M 1.0	2015/01/28 06:47:53	8.27×10^{5}	2015/01/28 23:11:52	3.73×10^{4}	0d 16h 23m 59s
	M 2.4	2015/01/29 00:59:52	1.21×10^{6}	2015/01/30 12:11:53	9.80×10^{3}	1d 11h 12m 1s
12282	M 2.4	2015/02/07 21:11:53	2.72×10^{6}	2015/02/09 22:59:53	4.36×10^{4}	2d 1h 48m 0s
12290	M 1.0	2015/02/28 05:35:55	3.23×10^{6}	2015/03/02 06:23:56	4.20×10^{4}	2d 0h 48m 1s
	M 1.1	2015/02/28 05:35:55	3.23×10^{6}	2015/03/02 09:35:56	1.11×10^{5}	2d 4h 0m 1s
	M 3.7	2015/02/28 05:35:55	3.23×10^{6}	2015/03/02 14:23:55	1.27×10^{5}	2d 8h 48m 0s
12297	X 2.1	2015/03/10 05:23:57	1.41×10^{6}	2015/03/11 16:11:57	1.90×10^{6}	1d 10h 48m 0s
12320	M 1.4	2015/04/05 03:36:00	3.37×10^{5}	2015/04/08 14:36:01	1.51×10^{5}	3d 11h 0m 1s
12321	M 1.1	2015/04/11 16:12:01	6.60×10^{6}	2015/04/12 08:48:01	1.10×10^{5}	0d 16h 36m 0s
12322	M 4.0	2015/04/21 10:12:02	1.43×10^{6}	2015/04/21 15:24:02	3.33×10^{4}	0d 5h 12m 0s
12325	M 1.2	2015/04/20 00:48:02	8.11×10^{5}	2015/04/21 22:00:02	1.53×10^{4}	1d 21h 12m 0s
12339	X 2.7	2015/05/05 07:24:04	6.86×10^{6}	2015/05/05 22:00:04	8.42×10^{4}	0d 14h 36m 0s
12360	M 1.3	2015/06/13 06:48:08	5.12×10^{5}	2015/06/13 07:24:08	2.32×10^{4}	0d 0h 36m 0s
	M 2.0	2015/06/13 20:24:08	6.99×10^{5}	2015/06/14 00:48:08	4.79×10^{4}	0d 4h 24m 0s
12365	M 1.2	2015/06/16 17:48:08	5.35×10^{5}	2015/06/18 00:36:08	2.28×10^{4}	1d 6h 48m 0s
12367	M 3.8	2015/06/21 04:24:08	7.44×10^{5}	2015/06/21 09:36:08	1.23×10^{5}	0d 5h 12m 0s
12371	M 6.5	2015/06/20 11:24:08	5.95×10^{5}	2015/06/22 17:36:08	1.78×10^{5}	2d 6h 12m 0s
	M 7.9	2015/06/20 11:24:08	5.95×10^{5}	2015/06/25 08:00:08	3.10×10^{5}	4d 20h 36m 0s
12378	M 1.5	2015/07/01 23:36:08	3.36×10^{6}	2015/07/03 12:48:08	3.30×10^{4}	1d 13h 12m 0s
12381	M 1.7	2015/07/04 00:36:08	4.73×10^{6}	2015/07/06 20:36:08	2.57×10^{5}	2d 20h 0m 0s
12403	M 1.1	2015/08/20 03:12:06	5.51×10^{5}	2015/08/21 19:12:06	2.62×10^{5}	1d 16h 0m 0s
	M 1.2	2015/08/20 03:12:06	5.51×10^{5}	2015/08/22 06:36:06	2.91×10^{5}	2d 3h 24m 0s
	M 3.5	2015/08/20 03:12:06	5.51×10^{5}	2015/08/22 21:24:06	1.71×10^{5}	2d 18h 12m 0s
	M 5.6	2015/08/20 03:12:06	5.51×10^{5}	2015/08/24 07:24:06	3.79×10^{5}	4d 4h 12m 0s
12415	M 1.1	2015/09/16 10:12:03	6.28×10^{5}	2015/09/17 09:36:03	3.13×10^{5}	0d 23h 24m 0s
	M 2.1	2015/09/16 10:12:03	6.28×10^{5}	2015/09/20 17:36:02	7.60×10^{3}	4d 7h 23m 59s
12422	M 7.6	2015/09/25 20:00:01	4.56×10^{5}	2015/09/28 14:48:01	2.35×10^{5}	2d 18h 48m 0s
12423	M 3.6	2015/09/27 04:36:01	6.36×10^{5}	2015/09/28 03:48:01	2.28×10^{5}	0d 23h 12m 0s
	M 1.2	2015/09/28 04:00:01	2.01×10^{6}	2015/09/29 03:12:01	3.07×10^{4}	0d 23h 12m 0s
	M 1.2	2015/09/28 04:00:01	2.01×10^{6}	2015/09/29 05:36:01	5.15×10^{4}	1d 1h 36m 0s
	M 1.3	2015/09/28 04:00:01	2.01×10^{6}	2015/09/29 08:48:01	1.12×10^{5}	1d 4h 48m 0s
12434	M 1.1	2015/10/13 07:59:59	2.43×10^{6}	2015/10/15 23:23:59	3.18×10^{4}	2d 15h 24m 0s
	M 1.1	2015/10/13 07:59:59	2.43×10^{6}	2015/10/16 06:11:59	1.01×10^{4}	2d 22h 12m 0s
12437	M 1.5	2015/10/16 17:11:58	1.81×10^{6}	2015/10/17 20:35:58	7.78×10^{5}	1d 3h 24m 0s
12443	M 3.7	2015/11/01 01:47:56	3.02×10^{5}	2015/11/04 13:35:56	1.46×10^{5}	3d 11h 48m 0s
12445	M 2.5	2015/11/02 03:35:56	4.61×10^{5}	2015/11/04 11:59:56	9.06×10^{3}	2d 8h 24m 0s
12449	M 3.9	2015/11/07 01:47:56	2.35×10^{6}	2015/11/09 12:47:55	9.11×10^{4}	2d 10h 59m 59s
12473	M 1.6	2015/12/21 10:59:52	2.61×10^{7}	2015/12/22 03:11:52	4.06×10^{4}	0d 16h 12m 0s
	M 4.7	2015/12/21 10:59:52	2.61×10^{7}	2015/12/23 00:23:52	1.42×10^{4}	1d 13h 24m 0s
	M 1.1	2015/12/21 10:59:52	2.61×10^{7}	2015/12/24 01:47:52	3.59×10^{5}	2d 14h 48m 0s
12497	M 1.0	2016/02/12 09:47:54	3.54×10^{5}	2016/02/12 10:35:54	3.57×10^{5}	0d 0h 48m 0s
	M 1.8	2016/02/12 20:23:53	7.06×10^{5}	2016/02/13 15:11:54	2.95×10^{6}	0d 18h 48m 1s
	M 1.0	2016/02/13 20:47:54	1.06×10^{8}	2016/02/14 19:23:54	3.53×10^{5}	0d 22h 36m 0s
	M 1.1	2016/02/13 20:47:54	1.06×10^{8}	2016/02/15 10:35:54	9.08×10^{6}	1d 13h 48m 0s
12529	M 6.7	2016/04/15 06:00:02	5.57×10^{5}	2016/04/18 00:12:02	2.50×10^{5}	2d 18h 12m 0s
12567	M 7.6	2016/07/19 17:48:08	4.33×10^{5}	2016/07/23 05:00:08	3.40×10^{5}	3d 11h 12m 0s
12644	M 5.3	2017/04/02 03:35:00	1.88×10^{5}	2017/04/02 07:47:00	9.38×10^{4}	0d 4h 12m 0s
	M 5.7	2017/04/02 03:35:00	1.88×10^{5}	2017/04/02 20:23:00	5.54×10^{4}	0d 16h 48m 0s
	M 5.8	2017/04/03 02:23:00	8.35×10^{5}	2017/04/03 14:23:00	1.37×10^{5}	0d 12h 0m 0s
12665	M 1.3	2017/07/06 04:48:08	2.09×10^{6}	2017/07/09 03:12:08	4.85×10^{5}	2d 22h 24m 0s
12673	X 2.2	2017/09/05 19:12:04	2.04×10^{6}	2017/09/06 09:00:04	1.26×10^{6}	0d 13h 48m 0s
	X 9.3	2017/09/05 19:12:04	2.04×10^{6}	2017/09/06 11:48:04	8.93×10^{5}	0d 16h 36m 0s
	X 1.3	2017/09/05 19:12:04	2.04×10^{6}	2017/09/07 14:24:04	7.28×10^{5}	1d 19h 12m 0s
	X 8.2	2017/09/10 01:00:03	3.93×10^{6}	2017/09/10 11:12:03	1.33×10^{5}	0d 10h 12m 0s
12696	B 9.7	2018/01/16 13:47:52	2.96×10^{5}	2018/01/18 07:23:52	7.62×10^{4}	1d 17h 36m 0s
	B 9.5	2018/01/16 13:47:52	2.96×10^{5}	2018/01/22 02:35:52	6.70×10^{3}	5d 12h 48m 0s

12699	C 8.1	2018/02/05 12:11:53	1.08×10^{6}	2018/02/07 13:35:53	2.25×10^{5}	2d 1h 24m 0s
12700	C 1.9	2018/03/02 04:23:56	2.20×10^{5}	2018/03/02 10:59:56	2.95×10^{4}	0d 6h 36m 0s
12703	B 9.0	2018/03/29 21:47:00	3.85×10^{5}	2018/04/01 12:47:00	3.49×10^{4}	2d 15h 0m 0s
12704	B 1.0	2018/04/12 19:36:01	1.41×10^{5}	2018/04/14 00:12:01	3.14×10^{4}	1d 4h 36m 0s
12710	B 9.8	2018/05/21 09:12:06	8.53×10^{5}	2018/05/24 12:24:06	2.59×10^{4}	3d 3h 12m 0s
12712	C 2.7	2018/05/24 00:24:06	8.47×10^{5}	2018/05/28 17:00:07	1.16×10^{5}	4d 16h 36m 1s
12713	B 4.7	2018/06/23 12:36:08	4.53×10^{5}	2018/06/23 14:36:08	2.24×10^{5}	0d 2h 0m 0s
12714	B 1.0	2018/06/18 23:00:08	1.07×10^{5}	2018/06/19 02:24:08	7.87×10^{4}	0d 3h 24m 0s
	B 1.8	2018/06/19 12:36:08	2.15×10^{5}	2018/06/20 00:00:08	1.39×10^{5}	0d 11h 24m 0s
12715	C 2.1	2018/06/20 03:36:08	3.29×10^{5}	2018/06/21 01:12:08	3.58×10^{5}	0d 21h 36m 0s
12719	B 1.6	2018/08/23 03:24:06	5.03×10^{6}	2018/08/24 21:48:05	9.96×10^{4}	1d 18h 23m 59s
12729	B 2.4	2018/12/09 01:35:53	1.78×10^{6}	2018/12/09 06:59:53	1.61×10^{4}	0d 5h 24m 0s
12732	C 1.6	2019/01/06 08:11:52	2.65×10^{6}	2019/01/06 10:35:52	3.08×10^{5}	0d 2h 24m 0s
12733	C 5.0	2019/01/23 04:35:52	1.80×10^{5}	2019/01/26 13:11:52	1.45×10^{5}	3d 8h 36m 0s
12734	C 1.3	2019/03/06 08:35:56	3.70×10^{5}	2019/03/08 03:11:56	5.99×10^{4}	1d 18h 36m 0s
12736	C 4.8	2019/03/18 16:59:58	2.26×10^{5}	2019/03/20 10:35:58	1.74×10^{5}	1d 17h 36m 0s
	C 5.6	2019/03/18 16:59:58	2.26×10^{5}	2019/03/21 03:11:58	2.53×10^{5}	2d 10h 12m 0s
12738	B 7.1	2019/04/10 01:24:01	3.55×10^{5}	2019/04/12 11:24:01	1.18×10^{5}	2d 10h 0m 0s
	B 8.1	2019/04/18 04:48:02	3.34×10^{6}	2019/04/20 00:24:02	1.11×10^{4}	1d 19h 36m 0s
12740	C 9.9	2019/05/04 02:24:04	2.38×10^{6}	2019/05/06 05:00:04	3.72×10^{5}	2d 2h 36m 0s
	C 6.7	2019/05/04 02:24:04	2.38×10^{6}	2019/05/09 05:36:05	1.43×10^{5}	5d 3h 12m 1s
12741	C 2.0	2019/05/07 21:00:04	1.60×10^{6}	2019/05/15 19:12:05	2.23×10^{5}	7d 22h 12m 1s

C. Appendix: Results for the 50% Resolution

Table C.1: Results of active regions analyzed for the SHARPs with 50% resolution. I can be seen the NOAA Active Region, the date-time of the maximum of the Weighted Horizontal Magnetic Gradient and its value WG_M previous the flare, the date-time of the flare and its value WG_M^{flare}, and in the last column the time range between the maximum of the WG_M an the flare occurrence.

NOAA AR	GOES Class	Date-time WG_M^{max}	WG_M^{max} [Wb/m]	Date-time Flare	WG_M^{flare} [Wb/m]	Time Range
11153	M 1.9	2011-02-08 01:59:53	1.58×10^{6}	2011-02-09 01:23:53	6.55×10^{5}	0d 23h 24m 0s
11158	X 2.2	2011-02-13 07:11:54	4.77×10^{5}	2011-02-15 01:47:54	2.71×10^{5}	1d 18h 36m 0s
11161	M 1.1	2011-02-15 18:47:54	3.16×10^{5}	2011-02-16 07:35:54	2.32×10^{5}	0d 12h 48m 0s
11162	M 1.0	2011-02-15 18:47:54	3.16×10^{5}	2011-02-18 10:23:54	2.08×10^{5}	2d 15h 36m 0s
	M 1.0	2011-02-15 18:47:54	3.16×10^{5}	2011-02-18 13:59:54	1.75×10^{5}	2d 19h 12m 0s
	M 1.3	2011-02-15 18:47:54	3.16×10^{5}	2011-02-18 20:59:54	1.80×10^{5}	3d 2h 12m 0s
11164	M 1.2	2011-03-06 19:23:56	6.51×10^{5}	2011-03-07 04:59:56	5.53×10^{5}	0d 9h 36m 0s
	M 1.4	2011-03-06 19:23:56	6.51×10^{5}	2011-03-07 07:59:56	5.37×10^{5}	0d 12h 36m 0s
	M 1.8	2011-03-06 19:23:56	6.51×10^{5}	2011-03-07 09:11:56	5.09×10^{5}	0d 13h 48m 0s
	M 3.7	2011-03-06 19:23:56	6.51×10^{5}	2011-03-07 19:47:56	4.56×10^{5}	1d 0h 24m 0s
11165	M 5.3	2011-03-07 01:59:56	6.99×10^{5}	2011-03-08 10:35:56	3.51×10^{5}	1d 8h 36m 0s
	M 4.4	2011-03-07 01:59:56	6.99×10^{5}	2011-03-08 18:11:56	2.82×10^{4}	1d 16h 12m 0s
11166	X 1.5	2011-03-07 16:59:56	3.76×10^{5}	2011-03-09 23:11:56	4.19×10^{5}	2d 6h 12m 0s
11169	M 4.2	2011-03-14 16:47:57	1.18×10^{6}	2011-03-14 19:35:57	6.09×10^{5}	0d 2h 48m 0s
	M 1.0	2011-03-14 16:47:57	1.18×10^{6}	2011-03-15 00:23:57	1.71×10^{5}	0d 7h 36m 0s
11176	M 1.4	2011-03-21 18:47:58	6.99×10^{5}	2011-03-23 01:59:58	1.22×10^{5}	1d 7h 12m 0s
	M 1.0	2011-03-21 18:47:58	6.99×10^{5}	2011-03-24 11:59:58	8.28×10^{4}	2d 17h 12m 0s
11190	M 1.3	2011-04-12 08:24:01	2.35×10^{6}	2011-04-15 17:00:01	4.02×10^{5}	3d 8h 36m 0s
11195	M 1.8	2011-04-19 16:00:02	7.03×10^{5}	2011-04-22 04:36:03	3.63×10^{5}	2d 12h 36m 1s
	M 1.2	2011-04-19 16:00:02	7.03×10^{5}	2011-04-22 15:48:02	3.21×10^{5}	2d 23h 48m 0s
11226	M 2.5	2011-06-07 03:48:07	2.76×10^{5}	2011-06-07 06:12:07	1.95×10^{5}	0d 2h 24m 0s
11260	M 1.1	2011-07-25 20:24:08	5.70×10^{5}	2011-07-27 15:48:08	1.39×10^{5}	1d 19h 24m 0s
11261	M 9.3	2011-07-27 00:48:08	6.75×10^{5}	2011-07-30 02:00:08	3.31×10^{5}	3d 1h 12m 0s
	M 6.0	2011-08-01 00:48:08	2.08×10^{6}	2011-08-03 13:12:07	5.00×10^{5}	2d 12h 23m 59s
	M 9.3	2011-08-01 00:48:08	2.08×10^{6}	2011-08-04 03:36:07	2.01×10^{5}	3d 2h 47m 59s
11263	X 6.9	2011-08-05 18:24:07	7.06×10^{5}	2011-08-09 07:48:07	7.30×10^{5}	3d 13h 24m 0s
11283	X 2.1	2011-09-06 06:00:04	7.50×10^{5}	2011-09-06 22:12:04	3.83×10^{5}	0d 16h 12m 0s
	X 1.8	2011-09-07 00:36:04	8.59×10^{5}	2011-09-07 22:36:04	2.74×10^{5}	0d 22h 0m 0s
11286	M 3.2	2011-09-01 20:48:04	2.29×10^{5}	2011-09-04 11:24:04	7.64×10^{4}	2d 14h 36m 0s
	M 1.6	2011-09-01 20:48:04	2.29×10^{5}	2011-09-05 04:12:04	4.76×10^{4}	3d 7h 24m 0s
	M 1.2	2011-09-01 20:48:04	2.29×10^{5}	2011-09-05 07:24:04	6.08×10^{4}	3d 10h 36m 0s
11301	M 1.8	2011-09-21 03:00:02	5.34×10^{5}	2011-09-21 12:00:02	7.33×10^{4}	0d 9h 0m 0s
11302	X 1.4	2011-09-22 11:00:02	1.56×10^{6}	2011-09-24 09:24:02	1.59×10^{5}	1d 22h 24m 0s

11305	M 1.0	2011-09-30 15:36:01	1.13×10^{6}	2011-09-30 19:00:01	6.63×10^{5}	0d 3h 24m 0s
	M 1.2	2011-09-30 15:36:01	1.13×10^{6}	2011-10-01 09:00:01	3.35×10^{5}	0d 17h 24m 0s
	M 3.9	2011-09-30 15:36:01	1.13×10^{6}	2011-10-02 00:36:01	2.46×10^{5}	1d 9h 0m 0s
11314	M 1.3	2011-10-20 11:35:58	2.48×10^{5}	2011-10-22 09:59:58	1.50×10^{4}	1d 22h 24m 0s
11319	M 1.3	2011-10-18 14:35:58	2.90×10^{5}	2011-10-21 12:47:58	1.26×10^{5}	2d 22h 12m 0s
11339	X 1.9	2011-11-01 15:11:56	2.01×10^{6}	2011-11-03 20:11:56	3.54×10^{5}	2d 5h 0m 0s
11342	M 1.1	2011-11-06 00:35:56	2.51×10^{5}	2011-11-09 12:59:55	1.78×10^{5}	3d 12h 23m 59s
11348	M 1.2	2011-11-14 03:35:55	3.91×10^{6}	2011-11-15 08:59:55	1.38×10^{5}	1d 5h 24m 0s
	M 1.1	2011-11-14 03:35:55	3.91×10^{6}	2011-11-15 22:23:55	8.99×10^{4}	1d 18h 48m 0s
11387	M 4.0	2011-12-25 16:23:52	1.04×10^{6}	2011-12-25 18:11:52	9.02×10^{5}	0d 1h 48m 0s
	M 1.5	2011-12-25 16:23:52	1.04×10^{6}	2011-12-26 02:11:52	3.84×10^{5}	0d 9h 48m 0s
	M 2.3	2011-12-25 16:23:52	1.04×10^{6}	2011-12-26 20:11:52	2.44×10^{5}	1d 3h 48m 0s
11389	M 2.0	2011-12-27 10:11:52	1.50×10^{6}	2011-12-29 21:47:52	1.35×10^{5}	2d 11h 36m 0s
	M 1.2	2011-12-27 10:11:52	1.50×10^{6}	2011-12-30 02:59:52	1.11×10^{5}	2d 16h 48m 0s
	M 2.4	2011-12-27 10:11:52	1.50×10^{6}	2011-12-31 13:11:52	2.91×10^{5}	4d 3h 0m 0s
	M 1.5	2011-12-27 10:11:52	1.50×10^{6}	2011-12-31 16:11:52	2.47×10^{5}	4d 6h 0m 0s
11401	M 1.0	2012-01-15 03:23:52	1.57×10^{6}	2012-01-17 04:35:52	1.72×10^{5}	2d 1h 12m 0s
	M 1.7	2012-01-15 03:23:52	1.57×10^{6}	2012-01-18 19:23:52	1.74×10^{5}	3d 16h 0m 0s
11402	X 1.7	2012-01-26 14:47:52	1.74×10^{6}	2012-01-27 17:35:52	5.61×10^{4}	1d 2h 48m 0s
11410	M 1.0	2012-02-04 10:23:53	3.61×10^{5}	2012-02-06 19:35:53	9.51×10^{4}	2d 9h 12m 0s
11429	X 1.1	2012-03-03 14:59:56	3.06×10^{6}	2012-03-05 02:35:56	2.36×10^{6}	1d 11h 36m 0s
	X 5.4	2012-03-05 07:35:56	9.86×10^{6}	2012-03-06 23:59:56	9.92×10^{5}	1d 16h 24m 0s
11430	X 1.3	2012-03-05 07:35:56	9.86×10^{6}	2012-03-07 00:59:56	9.59×10^{5}	1d 17h 24m 0s
11432	M 2.8	2012-03-12 22:11:57	3.64×10^{5}	2012-03-14 15:11:57	9.32×10^{4}	1d 17h 0m 0s
	M 1.8	2012-03-12 22:11:57	3.64×10^{5}	2012-03-15 08:11:57	6.21×10^{4}	2d 10h 0m 0s
11434	M 1.3	2012-03-12 02:11:56	1.65×10^{5}	2012-03-17 20:35:58	1.00×10^{5}	5d 18h 24m 2s
11520	X 1.4	2012-07-11 07:12:08	2.89×10^{6}	2012-07-12 15:36:08	1.08×10^{6}	1d 8h 24m 0s
11532	M 2.7	2012-07-26 03:24:08	2.39×10^{5}	2012-07-27 17:12:08	7.17×10^{4}	1d 13h 48m 0s
	M 6.1	2012-07-26 03:24:08	2.39×10^{5}	2012-07-28 20:48:08	1.00×10^{5}	2d 17h 24m 0s
	M 2.3	2012-07-26 03:24:08	2.39×10^{5}	2012-07-29 06:12:08	6.80×10^{4}	3d 2h 48m 0s
11748	X 1.2	2013-05-14 01:24:05	1.93×10^{6}	2013-05-15 01:24:05	2.35×10^{5}	1d 0h 0m 0s
11875	X 1.0	2013-10-27 17:23:57	8.10×10^{5}	2013-10-28 01:35:57	1.09×10^{4}	0d 8h 12m 0s
	X 2.3	2013-10-28 04:23:57	2.37×10^{6}	2013-10-29 21:47:57	1.79×10^{4}	1d 17h 24m 0s
11882	X 1.7	2013-10-24 09:23:57	2.67×10^{5}	2013-10-25 07:47:57	1.37×10^{5}	0d 22h 24m 0s
11890	X 3.3	2013-11-03 12:11:56	1.05×10^{6}	2013-11-05 22:11:56	3.54×10^{5}	2d 10h 0m 0s
	X 1.1	2013-11-03 12:11:56	1.05×10^{6}	2013-11-08 04:23:56	3.66×10^{5}	4d 16h 12m 0s
	X 1.1	2013-11-03 12:11:56	1.05×10^{6}	2013-11-10 05:11:55	3.54×10^{5}	6d 16h 59m 59s
11893	X 1.0	2013-11-15 22:47:54	3.11×10^{6}	2013-11-19 10:11:54	4.02×10^{6}	3d 11h 24m 0s
11944	X 1.2	2014-01-02 20:23:51	8.56×10^{5}	2014-01-07 17:59:52	3.31×10^{5}	4d 21h 36m 1s
11990	X 4.9	2014-02-23 22:59:55	4.06×10^{6}	2014-02-25 00:35:55	1.33×10^{4}	1d 1h 36m 0s
12017	X 1.0	2014-03-24 05:59:58	1.52×10^{5}	2014-03-29 17:35:59	1.42×10^{5}	5d 11h 36m 1s
12035	X 1.3	2014-04-22 02:12:03	1.36×10^{7}	2014-04-25 00:12:03	3.61×10^{4}	2d 22h 0m 0s
12087	X 2.2	2014-06-09 16:48:07	4.13×10^{5}	2014-06-10 11:36:08	2.05×10^{3}	0d 18h 48m 1s
	X 1.5	2014-06-10 11:48:08	6.50×10^{5}	2014-06-10 12:36:08	3.68×10^{4}	0d 0h 48m 0s
	X 1.0	2014-06-10 17:36:08	4.08×10^{6}	2014-06-11 09:00:08	9.59×10^{4}	0d 15h 24m 0s
12192	X 1.1	2014-10-17 05:47:58	8.97×10^{6}	2014-10-19 04:11:58	1.98×10^{5}	1d 22h 24m 0s
	X 1.6	2014-10-20 00:23:58	9.11×10^{6}	2014-10-22 13:59:58	6.98×10^{5}	2d 13h 36m 0s
	X 3.1	2014-10-20 00:23:58	9.11×10^{6}	2014-10-24 21:11:57	7.29×10^{5}	4d 20h 47m 59s
	X 1.0	2014-10-20 00:23:58	9.11×10^{6}	2014-10-25 16:59:57	8.74×10^{5}	5d 16h 35m 59s
12205	M 7.9	2014-11-04 20:11:56	4.77×10^{6}	2014-11-05 09:23:56	7.14×10^{4}	0d 13h 12m 0s
	M 5.4	2014-11-04 20:11:56	4.77×10^{6}	2014-11-06 03:35:56	1.26×10^{4}	1d 7h 24m 0s
	X 1.6	2014-11-04 20:11:56	4.77×10^{6}	2014-11-07 16:47:55	1.82×10^{5}	2d 20h 35m 59s
12242	X 1.8	2014-12-17 06:23:52	2.11×10^{6}	2014-12-20 00:11:52	1.73×10^{5}	2d 17h 48m 0s
12253	M 1.1	2015-01-02 14:11:52	3.81×10^{5}	2015-01-03 09:35:52	2.94×10^{5}	0d 19h 24m 0s
	M 1.3	2015-01-02 14:11:52	3.81×10^{5}	2015-01-04 15:23:52	2.06×10^{5}	2d 1h 12m 0s
12257	M 5.6	2015-01-10 00:11:51	5.62×10^{5}	2015-01-13 04:11:52	3.70×10^{4}	3d 4h 0m 1s
	M 2.2	2015-01-13 04:59:52	2.16×10^{6}	2015-01-14 12:35:52	9.86×10^{4}	1d 7h 36m 0s
12268	M 1.1	2015-01-23 11:35:52	3.97×10^{6}	2015-01-26 16:47:52	2.14×10^{5}	3d 5h 12m 0s
	M 1.4	2015-01-23 11:35:52	3.97×10^{6}	2015-01-28 04:23:52	1.47×10^{5}	4d 16h 48m 0s

	M 2.1	2015-01-23 11:35:52	3.97×10^{6}	2015-01-29 11:35:53	1.82×10^{5}	6d 0h 0m 1s
	M 2.0	2015-01-23 11:35:52	3.97×10^{6}	2015-01-30 00:35:52	2.25×10^{5}	6d 13h 0m 0s
12277	M 1.0	2015-01-28 07:11:53	2.49×10^{6}	2015-01-28 23:11:52	2.48×10^{4}	0d 15h 59m 59s
	M 2.4	2015-01-29 05:11:53	3.72×10^{6}	2015-01-30 12:11:53	7.95×10^{4}	1d 7h 0m 0s
12282	M 2.4	2015-02-08 02:47:53	2.55×10^{6}	2015-02-09 22:59:53	4.42×10^{4}	1d 20h 12m 0s
12290	M 1.0	2015-03-01 21:11:55	8.22×10^{6}	2015-03-02 06:23:56	1.09×10^{5}	0d 9h 12m 1s
	M 1.1	2015-03-01 21:11:55	8.22×10^{6}	2015-03-02 09:35:56	1.12×10^{5}	0d 12h 24m 1s
	M 3.7	2015-03-01 21:11:55	8.22×10^{6}	2015-03-02 14:23:55	4.48×10^{4}	0d 17h 12m 0s
12297	X 2.1	2015-03-10 05:35:57	1.41×10^{6}	2015-03-11 16:11:57	1.96×10^{6}	1d 10h 36m 0s
12320	M 1.4	2015-04-04 22:48:00	1.06×10^{6}	2015-04-08 14:36:01	1.54×10^{5}	3d 15h 48m 1s
12321	M 1.1	2015-04-11 07:00:01	1.98×10^{6}	2015-04-12 08:48:01	8.16×10^{4}	1d 1h 48m 0s
12322	M 4.0	2015-04-20 21:48:02	1.23×10^{6}	2015-04-21 15:24:02	1.82×10^{4}	0d 17h 36m 0s
12325	M 1.2	2015-04-20 01:36:02	9.81×10^{5}	2015-04-21 22:00:02	1.92×10^{5}	1d 20h 24m 0s
12339	X 2.7	2015-05-04 21:24:04	7.70×10^{6}	2015-05-05 22:00:04	5.38×10^{4}	1d 0h 36m 0s
12360	M 1.3	2015-06-13 04:24:08	1.94×10^{6}	2015-06-13 07:24:08	1.51×10^{5}	0d 3h 0m 0s
	M 2.0	2015-06-13 23:00:08	9.93×10^{6}	2015-06-14 00:48:08	1.52×10^{5}	0d 1h 48m 0s
12365	M 1.2	2015-06-17 05:12:08	2.23×10^{6}	2015-06-18 00:36:08	1.94×10^{4}	0d 19h 24m 0s
12367	M 3.8	2015-06-21 07:24:08	3.18×10^{5}	2015-06-21 09:36:08	1.75×10^{5}	0d 2h 12m 0s
12371	M 6.5	2015-06-20 12:48:08	5.93×10^{5}	2015-06-22 17:36:08	1.80×10^{5}	2d 4h 48m 0s
	M 7.9	2015-06-20 12:48:08	5.93×10^{5}	2015-06-25 08:00:08	3.20×10^{5}	4d 19h 12m 0s
12378	M 1.5	2015-07-02 09:12:08	7.34×10^{6}	2015-07-03 12:48:08	2.66×10^{5}	1d 3h 36m 0s
12381	M 1.7	2015-07-04 00:12:08	6.62×10^{5}	2015-07-06 20:36:08	2.54×10^{5}	2d 20h 24m 0s
12403	M 1.1	2015-08-20 03:24:06	5.88×10^{5}	2015-08-21 19:12:06	3.00×10^{5}	1d 15h 48m 0s
	M 1.2	2015-08-20 03:24:06	5.88×10^{5}	2015-08-22 06:36:06	2.99×10^{5}	2d 3h 12m 0s
	M 3.5	2015-08-20 03:24:06	5.88×10^{5}	2015-08-22 21:24:06	1.74×10^{5}	2d 18h 0m 0s
	M 5.6	2015-08-20 03:24:06	5.88×10^{5}	2015-08-24 07:24:06	3.83×10^{5}	4d 4h 0m 0s
12415	M 1.1	2015-09-16 10:12:03	6.30×10^{5}	2015-09-17 09:36:03	3.08×10^{5}	0d 23h 24m 0s
	M 2.1	2015-09-16 10:12:03	6.30×10^{5}	2015-09-20 17:36:02	1.58×10^{5}	4d 7h 23m 59s
12422	M 7.6	2015-09-25 20:12:01	4.58×10^{5}	2015-09-28 14:48:01	2.39×10^{5}	2d 18h 36m 0s
12423	M 3.6	2015-09-27 04:36:01	5.38×10^{5}	2015-09-28 03:48:01	3.32×10^{5}	0d 23h 12m 0s
	M 1.2	2015-09-28 02:12:01	7.43×10^{5}	2015-09-29 03:12:01	4.25×10^{5}	1d 1h 0m 0s
	M 1.2	2015-09-28 02:12:01	7.43×10^{5}	2015-09-29 05:36:01	5.03×10^{4}	1d 3h 24m 0s
	M 1.3	2015-09-28 02:12:01	7.43×10^{5}	2015-09-29 08:48:01	1.54×10^{5}	1d 6h 36m 0s
12434	M 1.1	2015-10-14 08:11:59	1.66×10^{6}	2015-10-15 23:23:59	6.41×10^{4}	1d 15h 12m 0s
	M 1.1	2015-10-14 08:11:59	1.66×10^{6}	2015-10-16 06:11:59	6.66×10^{4}	1d 22h 0m 0s
12437	M 1.5	2015-10-17 16:59:58	2.81×10^{6}	2015-10-17 20:35:58	8.28×10^{5}	0d 3h 36m 0s
12443	M 3.7	2015-10-31 19:35:56	3.12×10^{5}	2015-11-04 13:35:56	1.51×10^{5}	3d 18h 0m 0s
12445	M 2.5	2015-11-04 02:23:56	9.22×10^{5}	2015-11-04 11:59:56	1.07×10^{4}	0d 9h 36m 0s
12449	M 3.9	2015-11-07 14:11:55	5.04×10^{6}	2015-11-09 12:47:55	3.23×10^{4}	1d 22h 36m 0s
12473	M 1.6	2015-12-21 15:47:52	3.92×10^{6}	2015-12-22 03:11:52	1.16×10^{5}	0d 11h 24m 0s
	M 4.7	2015-12-22 21:23:52	4.14×10^{6}	2015-12-23 00:23:52	1.16×10^{5}	0d 3h 0m 0s
	M 1.1	2015-12-22 21:23:52	4.14×10^{6}	2015-12-24 01:47:52	3.59×10^{5}	1d 4h 24m 0s
12497	M 1.0	2016-02-12 09:35:54	3.70×10^{5}	2016-02-12 10:35:54	3.59×10^{5}	0d 1h 0m 0s
	M 1.8	2016-02-12 20:23:53	8.03×10^{5}	2016-02-13 15:11:54	3.57×10^{6}	0d 18h 48m 1s
	M 1.0	2016-02-14 03:59:54	4.60×10^{7}	2016-02-14 19:23:54	1.81×10^{6}	0d 15h 24m 0s
	M 1.1	2016-02-14 03:59:54	4.60×10^{7}	2016-02-15 10:35:54	2.48×10^{6}	1d 6h 36m 0s
12529	M 6.7	2016-04-15 05:24:02	5.77×10^{5}	2016-04-18 00:12:02	2.55×10^{5}	2d 18h 48m 0s
12567	M 7.6	2016-07-19 17:24:08	4.61×10^{5}	2016-07-23 05:00:08	3.23×10^{5}	3d 11h 36m 0s
12644	M 5.3	2017-04-02 06:47:00	1.86×10^{5}	2017-04-02 07:47:00	9.45×10^{4}	0d 1h 0m 0s
	M 5.7	2017-04-02 17:59:00	2.64×10^{5}	2017-04-02 20:23:00	7.10×10^{4}	0d 2h 24m 0s
	M 5.8	2017-04-03 11:12:00	4.43×10^{5}	2017-04-03 14:23:00	2.47×10^{5}	0d 3h 11m 0s
12665	M 1.3	2017-07-06 08:12:08	4.68×10^{6}	2017-07-09 03:12:08	5.07×10^{5}	2d 19h 0m 0s
12673	X 2.2	2017-09-05 17:24:04	2.14×10^{6}	2017-09-06 09:00:04	1.35×10^{6}	0d 15h 36m 0s
	X 9.3	2017-09-05 17:24:04	2.14×10^{6}	2017-09-06 11:48:04	8.79×10^{5}	0d 18h 24m 0s
	X 1.3	2017-09-06 17:48:04	2.15×10^{6}	2017-09-07 14:24:04	8.01×10^{5}	0d 20h 36m 0s
	X 8.2	2017-09-10 10:00:04	3.95×10^{6}	2017-09-10 11:12:03	5.10×10^{4}	0d 1h 11m 59s
12696	B 9.7	2018-01-16 13:35:52	3.16×10^{5}	2018-01-18 07:23:52	7.79×10^{4}	1d 17h 48m 0s
	B 9.5	2018-01-16 13:35:52	3.16×10^{5}	2018-01-22 02:35:52	9.99×10^{3}	5d 13h 0m 0s

12699	C 8.1	2018-02-05 07:47:53	1.71×10^{7}	2018-02-07 13:35:53	2.26×10^{5}	2d 5h 48m 0s
12700	C 1.9	2018-03-02 08:47:56	6.08×10^{5}	2018-03-02 10:59:56	2.85×10^{4}	0d 2h 12m 0s
12703	B 9.0	2018-03-29 19:59:00	1.22×10^{5}	2018-04-01 12:47:00	3.55×10^{4}	2d 16h 48m 0s
12704	B 1.0	2018-04-12 19:36:01	1.56×10^{5}	2018-04-14 00:12:01	3.39×10^{4}	1d 4h 36m 0s
12710	B 9.8	2018-05-21 08:00:06	1.04×10^{6}	2018-05-24 12:24:06	2.92×10^{4}	3d 4h 24m 0s
12712	C 2.7	2018-05-25 01:12:06	3.03×10^{6}	2018-05-28 17:00:07	1.01×10^{5}	3d 15h 48m 1s
12713	B 4.7	2018-06-23 13:24:08	2.53×10^{5}	2018-06-23 14:36:08	2.42×10^{5}	0d 1h 12m 0s
12714	B 1.0	2018-06-18 23:00:08	1.15×10^{5}	2018-06-19 02:24:08	9.14×10^{4}	0d 3h 24m 0s
	B 1.8	2018-06-19 12:24:08	2.17×10^{5}	2018-06-20 00:00:08	1.45×10^{5}	0d 11h 36m 0s
12715	C 2.1	2018-06-20 03:48:08	3.21×10^{5}	2018-06-21 01:12:08	3.58×10^{5}	0d 21h 24m 0s
12719	B 1.6	2018-08-23 03:00:06	4.26×10^{6}	2018-08-24 21:48:05	9.77×10^{4}	1d 18h 47m 59s
12729	B 2.4	2018-12-09 05:23:53	7.36×10^{5}	2018-12-09 06:59:53	1.08×10^{5}	0d 1h 36m 0s
12732	C 1.6	2019-01-06 08:11:52	5.10×10^{6}	2019-01-06 10:35:52	2.69×10^{5}	0d 2h 24m 0s
12733	C 5.0	2019-01-23 03:11:52	1.98×10^{5}	2019-01-26 13:11:52	1.36×10^{5}	3d 10h 0m 0s
12734	C 1.3	2019-03-06 06:59:56	3.87×10^{5}	2019-03-08 03:11:56	7.55×10^{4}	1d 20h 12m 0s
12736	C 4.8	2019-03-18 14:59:58	4.46×10^{5}	2019-03-20 10:35:58	1.73×10^{5}	1d 19h 36m 0s
	C 5.6	2019-03-18 14:59:58	4.46×10^{5}	2019-03-21 03:11:58	2.67×10^{5}	2d 12h 12m 0s
12738	B 7.1	2019-04-10 01:24:01	3.78×10^{5}	2019-04-12 11:24:01	1.18×10^{5}	2d 10h 0m 0s
	B 8.1	2019-04-18 05:00:02	3.25×10^{6}	2019-04-20 00:24:02	2.19×10^{4}	1d 19h 24m 0s
12740	C 9.9	2019-05-04 05:12:04	1.29×10^{6}	2019-05-06 05:00:04	3.81×10^{5}	1d 23h 48m 0s
	C 6.7	2019-05-04 05:12:04	1.29×10^{6}	2019-05-09 05:36:05	1.48×10^{5}	5d 0h 24m 1s
12741	C 2.0	2019-05-08 00:12:05	1.67×10^{6}	2019-05-15 19:12:05	2.20×10^{5}	7d 19h 0m 0s

D. Appendix: Results for the 25% Resolution

Table D.1: Results of active regions analyzed for the SHARPs with 25% resolution. I can be seen the NOAA Active Region, the date-time of the maximum of the Weighted Horizontal Magnetic Gradient and its value WG_M previous the flare, the date-time of the flare and its value WG_M^{flare}, and in the last column the time range between the maximum of the WG_M an the flare occurrence.

NOAA AR	GOES Class	Date-time WG_M^{max}	WG_M^{max} [Wb/m]	Date-time Flare	WG_M^{flare} [Wb/m]	Time Range
11153	M 1.9	2011-02-07 20:59:53	2.02×10^6	2011-02-09 01:23:53	6.24×10^5	1d4h24m0s
11158	X 2.2	2011-02-13 07:11:54	5.81×10^5	2011-02-15 01:47:54	3.07×10^5	1d18h36m0s
11161	M 1.1	2011-02-15 21:59:54	3.62×10^5	2011-02-16 07:35:54	2.69×10^5	0d9h36m0s
11162	M 1.0	2011-02-15 21:59:54	3.62×10^5	2011-02-18 10:23:54	2.23×10^5	2d12h24m0s
	M 1.0	2011-02-15 21:59:54	3.62×10^5	2011-02-18 13:59:54	2.20×10^5	2d16h0m0s
	M 1.3	2011-02-15 21:59:54	3.62×10^5	2011-02-18 20:59:54	1.80×10^5	2d23h0m0s
11164	M 1.2	2011-03-06 15:59:56	7.29×10^5	2011-03-07 04:59:56	6.23×10^5	0d13h0m0s
	M 1.4	2011-03-06 15:59:56	7.29×10^5	2011-03-07 07:59:56	5.67×10^5	0d16h0m0s
	M 1.8	2011-03-06 15:59:56	7.29×10^5	2011-03-07 09:11:56	6.04×10^5	0d17h12m0s
	M 3.7	2011-03-06 15:59:56	7.29×10^5	2011-03-07 19:47:56	4.69×10^5	1d3h48m0s
11165	M 5.3	2011-03-06 04:23:56	1.60×10^6	2011-03-08 10:35:56	4.29×10^5	2d6h12m0s
	M 4.4	2011-03-06 04:23:56	1.60×10^6	2011-03-08 18:11:56	3.17×10^4	2d13h48m0s
11166	X 1.5	2011-03-07 17:11:56	4.14×10^5	2011-03-09 23:11:56	4.41×10^5	2d6h0m0s
11169	M 4.2	2011-03-14 17:59:57	1.21×10^6	2011-03-14 19:35:57	2.29×10^5	0d1h36m0s
	M 1.0	2011-03-14 17:59:57	1.21×10^6	2011-03-15 00:23:57	1.75×10^5	0d6h24m0s
11176	M 1.4	2011-03-21 20:59:58	8.37×10^5	2011-03-23 01:59:58	1.29×10^5	1d5h0m0s
	M 1.0	2011-03-21 20:59:58	8.37×10^5	2011-03-24 11:59:58	6.45×10^4	2d15h0m0s
11190	M 1.3	2011-04-12 08:24:01	4.40×10^6	2011-04-15 17:00:01	5.19×10^5	3d8h36m0s
11195	M 1.8	2011-04-19 19:00:02	5.51×10^5	2011-04-22 04:36:03	3.97×10^5	2d9h36m1s
	M 1.2	2011-04-19 19:00:02	5.51×10^5	2011-04-22 15:48:02	3.56×10^5	2d20h48m0s
11226	M 2.5	2011-06-07 03:48:07	4.44×10^5	2011-06-07 06:12:07	1.85×10^5	0d2h24m0s
11260	M 1.1	2011-07-25 22:48:08	3.50×10^5	2011-07-27 15:48:08	1.21×10^5	1d17h0m0s
11261	M 9.3	2011-07-27 00:48:08	7.88×10^5	2011-07-30 02:00:08	3.06×10^5	3d1h12m0s
	M 6.0	2011-08-01 00:12:07	2.79×10^6	2011-08-03 13:12:07	5.56×10^5	2d13h0m0s
	M 9.3	2011-08-01 00:12:07	2.79×10^6	2011-08-04 03:36:07	2.51×10^5	3d3h24m0s
11263	X 6.9	2011-08-05 18:12:07	7.74×10^5	2011-08-09 07:48:07	8.33×10^5	3d13h36m0s
11283	X 2.1	2011-09-06 07:48:04	9.80×10^5	2011-09-06 22:12:04	6.30×10^5	0d14h24m0s
	X 1.8	2011-09-07 05:12:04	1.02×10^6	2011-09-07 22:36:04	2.90×10^5	0d17h24m0s
11286	M 3.2	2011-09-01 20:24:04	2.70×10^5	2011-09-04 11:24:04	1.00×10^5	2d15h0m0s
	M 1.6	2011-09-01 20:24:04	2.70×10^5	2011-09-05 04:12:04	6.03×10^4	3d7h48m0s
	M 1.2	2011-09-01 20:24:04	2.70×10^5	2011-09-05 07:24:04	6.01×10^4	3d11h0m0s
11301	M 1.8	2011-09-18 22:36:02	4.91×10^5	2011-09-21 12:00:02	7.36×10^4	2d13h24m0s
11302	X 1.4	2011-09-22 10:00:02	1.74×10^6	2011-09-24 09:24:02	2.14×10^5	1d23h24m0s

11305	M 1.0	2011-09-30 17:00:01	1.38×10^{6}	2011-09-30 19:00:01	6.78×10^{5}	0d2h0m0s
	M 1.2	2011-09-30 17:00:01	1.38×10^{6}	2011-10-01 09:00:01	5.03×10^{5}	0d16h0m0s
	M 3.9	2011-09-30 17:00:01	1.38×10^{6}	2011-10-02 00:36:01	2.87×10^{5}	1d7h36m0s
11314	M 1.3	2011-10-21 20:11:58	3.11×10^{5}	2011-10-22 09:59:58	1.22×10^{4}	0d13h48m0s
11319	M 1.3	2011-10-18 14:23:58	3.40×10^{5}	2011-10-21 12:47:58	1.05×10^{5}	2d22h24m0s
11339	X 1.9	2011-11-01 15:59:56	3.39×10^{6}	2011-11-03 20:11:56	4.26×10^{5}	2d4h12m0s
11342	M 1.1	2011-11-06 00:35:56	3.73×10^{5}	2011-11-09 12:59:55	2.17×10^{5}	3d12h23m59s
11348	M 1.2	2011-11-14 03:11:55	9.88×10^{6}	2011-11-15 08:59:55	1.99×10^{5}	1d5h48m0s
	M 1.1	2011-11-14 03:11:55	9.88×10^{6}	2011-11-15 22:23:55	8.18×10^{4}	1d19h12m0s
11387	M 4.0	2011-12-25 17:11:52	1.36×10^{6}	2011-12-25 18:11:52	1.06×10^{6}	0d1h0m0s
	M 1.5	2011-12-25 17:11:52	1.36×10^{6}	2011-12-26 02:11:52	3.98×10^{5}	0d9h0m0s
	M 2.3	2011-12-25 17:11:52	1.36×10^{6}	2011-12-26 20:11:52	2.92×10^{5}	1d3h0m0s
11389	M 2.0	2011-12-29 02:59:52	1.01×10^{6}	2011-12-29 21:47:52	1.71×10^{5}	0d18h48m0s
	M 1.2	2011-12-29 02:59:52	1.01×10^{6}	2011-12-30 02:59:52	1.29×10^{5}	1d0h0m0s
	M 2.4	2011-12-29 02:59:52	1.01×10^{6}	2011-12-31 13:11:52	3.17×10^{5}	2d10h12m0s
	M 1.5	2011-12-29 02:59:52	1.01×10^{6}	2011-12-31 16:11:52	2.70×10^{5}	2d13h12m0s
11401	M 1.0	2012-01-16 04:23:52	8.64×10^{5}	2012-01-17 04:35:52	2.34×10^{5}	1d0h12m0s
	M 1.7	2012-01-16 04:23:52	8.64×10^{5}	2012-01-18 19:23:52	8.41×10^{4}	2d15h0m0s
11402	X 1.7	2012-01-26 20:47:52	1.75×10^{6}	2012-01-27 17:35:52	6.70×10^{4}	0d20h48m0s
11410	M 1.0	2012-02-04 09:11:53	4.63×10^{5}	2012-02-06 19:35:53	1.35×10^{5}	2d10h24m0s
11429	X 1.1	2012-03-03 15:59:56	5.15×10^{6}	2012-03-05 02:35:56	2.29×10^{6}	1d10h36m0s
	X 5.4	2012-03-05 14:47:56	1.23×10^{7}	2012-03-06 23:59:56	1.04×10^{6}	1d9h12m0s
11430	X 1.3	2012-03-05 14:47:56	1.23×10^{7}	2012-03-07 00:59:56	1.09×10^{6}	1d10h12m0s
11432	M 2.8	2012-03-13 01:59:57	5.08×10^{5}	2012-03-14 15:11:57	1.29×10^{5}	1d13h12m0s
	M 1.8	2012-03-13 01:59:57	5.08×10^{5}	2012-03-15 08:11:57	6.93×10^{4}	2d6h12m0s
11434	M 1.3	2012-03-12 02:47:56	1.94×10^{5}	2012-03-17 20:35:58	1.05×10^{5}	5d17h48m2s
11520	X 1.4	2012-07-11 06:00:08	3.79×10^{6}	2012-07-12 15:36:08	1.01×10^{6}	1d9h36m0s
11532	M 2.7	2012-07-27 02:00:08	2.98×10^{5}	2012-07-27 17:12:08	8.19×10^{4}	0d15h12m0s
	M 6.1	2012-07-27 02:00:08	2.98×10^{5}	2012-07-28 20:48:08	1.10×10^{5}	1d18h48m0s
	M 2.3	2012-07-27 02:00:08	2.98×10^{5}	2012-07-29 06:12:08	7.72×10^{4}	2d4h12m0s
11748	X 1.2	2013-05-14 01:24:05	4.01×10^{6}	2013-05-15 01:24:05	2.26×10^{5}	1d0h0m0s
11875	X 1.0	2013-10-27 16:59:57	9.02×10^{5}	2013-10-28 01:35:57	1.56×10^{5}	0d8h36m0s
	X 2.3	2013-10-28 05:11:57	2.49×10^{6}	2013-10-29 21:47:57	6.78×10^{4}	1d16h36m0s
11882	X 1.7	2013-10-24 07:35:57	4.35×10^{5}	2013-10-25 07:47:57	1.38×10^{5}	1d0h12m0s
11890	X 3.3	2013-11-02 08:47:56	1.53×10^{6}	2013-11-05 22:11:56	3.36×10^{5}	3d13h24m0s
	X 1.1	2013-11-02 08:47:56	1.53×10^{6}	2013-11-08 04:23:56	3.67×10^{5}	5d19h36m0s
	X 1.1	2013-11-02 08:47:56	1.53×10^{6}	2013-11-10 05:11:55	3.79×10^{5}	7d20h23m59s
11893	X 1.0	2013-11-16 01:11:54	4.25×10^{6}	2013-11-19 10:11:54	2.09×10^{6}	3d9h0m0s
11944	X 1.2	2014-01-02 12:11:51	1.09×10^{6}	2014-01-07 17:59:52	4.77×10^{5}	5d5h48m1s
11990	X 4.9	2014-02-24 19:59:55	1.70×10^{6}	2014-02-25 00:35:55	5.35×10^{4}	0d4h36m0s
12017	X 1.0	2014-03-26 10:35:59	1.77×10^{5}	2014-03-29 17:35:59	1.38×10^{5}	3d7h0m0s
12035	X 1.3	2014-04-22 08:12:03	7.03×10^{6}	2014-04-25 00:12:03	6.59×10^{4}	2d16h0m0s
12087	X 2.2	2014-06-09 20:48:07	8.87×10^{5}	2014-06-10 11:36:08	1.54×10^{4}	0d14h48m1s
	X 1.5	2014-06-09 20:48:07	8.87×10^{5}	2014-06-10 12:36:08	1.45×10^{4}	0d15h48m1s
	X 1.0	2014-06-09 20:48:07	8.87×10^{5}	2014-06-11 09:00:08	1.04×10^{5}	1d12h12m1s
12192	X 1.1	2014-10-16 18:35:58	4.80×10^{6}	2014-10-19 04:11:58	4.76×10^{5}	2d9h36m0s
	X 1.6	2014-10-16 18:35:58	4.80×10^{6}	2014-10-22 13:59:58	7.50×10^{5}	5d19h24m0s
	X 3.1	2014-10-16 18:35:58	4.80×10^{6}	2014-10-24 21:11:57	7.10×10^{5}	8d2h35m59s
	X 1.0	2014-10-16 18:35:58	4.80×10^{6}	2014-10-25 16:59:57	9.08×10^{5}	8d22h23m59s
12205	M 7.9	2014-11-05 00:47:56	2.67×10^{6}	2014-11-05 09:23:56	6.16×10^{4}	0d8h36m0s
	M 5.4	2014-11-05 20:23:56	1.52×10^{7}	2014-11-06 03:35:56	6.13×10^{4}	0d7h12m0s
	X 1.6	2014-11-05 20:23:56	1.52×10^{7}	2014-11-07 16:47:55	2.16×10^{5}	1d20h23m59s
12242	X 1.8	2014-12-17 06:23:52	2.16×10^{6}	2014-12-20 00:11:52	1.86×10^{5}	2d17h48m0s
12253	M 1.1	2015-01-02 17:23:52	4.05×10^{5}	2015-01-03 09:35:52	2.84×10^{5}	0d16h12m0s
	M 1.3	2015-01-02 17:23:52	4.05×10^{5}	2015-01-04 15:23:52	2.30×10^{5}	1d22h0m0s
12257	M 5.6	2015-01-13 02:47:52	1.72×10^{6}	2015-01-13 04:11:52	7.06×10^{4}	0d1h24m0s
	M 2.2	2015-01-14 12:11:52	8.51×10^{6}	2015-01-14 12:35:52	1.27×10^{6}	0d0h24m0s
12268	M 1.1	2015-01-24 08:35:52	6.52×10^{6}	2015-01-26 16:47:52	2.44×10^{5}	2d8h12m0s
	M 1.4	2015-01-24 08:35:52	6.52×10^{6}	2015-01-28 04:23:52	1.60×10^{5}	3d19h48m0s

	M 2.1	2015-01-24 08:35:52	6.52×10^{6}	2015-01-29 11:35:53	2.09×10^{5}	5d3h0m1s
	M 2.0	2015-01-24 08:35:52	6.52×10^{6}	2015-01-30 00:35:52	2.26×10^{5}	5d16h0m0s
12277	M 1.0	2015-01-28 11:47:52	9.36×10^{5}	2015-01-28 23:11:52	9.86×10^{4}	0d11h24m0s
	M 2.4	2015-01-29 04:47:53	2.22×10^{6}	2015-01-30 12:11:53	1.00×10^{5}	1d7h24m0s
12282	M 2.4	2015-02-09 18:47:53	5.83×10^{6}	2015-02-09 22:59:53	2.22×10^{4}	0d4h12m0s
12290	M 1.0	2015-03-01 15:23:55	1.60×10^{7}	2015-03-02 06:23:56	3.67×10^{4}	0d15h0m1s
	M 1.1	2015-03-01 15:23:55	1.60×10^{7}	2015-03-02 09:35:56	1.20×10^{5}	0d18h12m1s
	M 3.7	2015-03-01 15:23:55	1.60×10^{7}	2015-03-02 14:23:55	6.80×10^{4}	0d23h0m0s
12297	X 2.1	2015-03-10 05:23:57	1.57×10^{6}	2015-03-11 16:11:57	2.31×10^{6}	1d10h48m0s
12320	M 1.4	2015-04-05 03:48:00	3.98×10^{6}	2015-04-08 14:36:01	1.90×10^{5}	3d10h48m1s
12321	M 1.1	2015-04-12 03:12:01	3.53×10^{7}	2015-04-12 08:48:01	7.70×10^{4}	0d5h36m0s
12322	M 4.0	2015-04-21 04:12:02	2.72×10^{8}	2015-04-21 15:24:02	1.21×10^{4}	0d11h12m0s
12325	M 1.2	2015-04-20 00:12:02	4.14×10^{6}	2015-04-21 22:00:02	1.52×10^{5}	1d21h48m0s
12339	X 2.7	2015-05-04 22:24:04	3.40×10^{7}	2015-05-05 22:00:04	1.17×10^{5}	0d23h36m0s
12360	M 1.3	2015-06-12 23:12:08	1.01×10^{6}	2015-06-13 07:24:08	1.60×10^{5}	0d8h12m0s
	M 2.0	2015-06-13 17:24:08	2.02×10^{6}	2015-06-14 00:48:08	1.87×10^{4}	0d7h24m0s
12365	M 1.2	2015-06-17 18:48:08	1.90×10^{6}	2015-06-18 00:36:08	3.43×10^{5}	0d5h48m0s
12367	M 3.8	2015-06-20 22:36:08	2.95×10^{5}	2015-06-21 09:36:08	2.60×10^{5}	0d11h0m0s
12371	M 6.5	2015-06-20 10:36:08	6.58×10^{5}	2015-06-22 17:36:08	2.08×10^{5}	2d7h0m0s
	M 7.9	2015-06-20 10:36:08	6.58×10^{5}	2015-06-25 08:00:08	3.18×10^{5}	4d21h24m0s
12378	M 1.5	2015-07-02 22:24:08	3.82×10^{6}	2015-07-03 12:48:08	3.62×10^{4}	0d14h24m0s
12381	M 1.7	2015-07-04 02:00:08	2.70×10^{7}	2015-07-06 20:36:08	2.79×10^{5}	2d18h36m0s
12403	M 1.1	2015-08-20 01:12:06	7.69×10^{5}	2015-08-21 19:12:06	3.67×10^{5}	1d18h0m0s
	M 1.2	2015-08-20 01:12:06	7.69×10^{5}	2015-08-22 06:36:06	3.15×10^{5}	2d5h24m0s
	M 3.5	2015-08-20 01:12:06	7.69×10^{5}	2015-08-22 21:24:06	1.79×10^{5}	2d20h12m0s
	M 5.6	2015-08-20 01:12:06	7.69×10^{5}	2015-08-24 07:24:06	4.09×10^{5}	4d6h12m0s
12415	M 1.1	2015-09-16 10:36:03	7.12×10^{5}	2015-09-17 09:36:03	3.13×10^{5}	0d23h0m0s
	M 2.1	2015-09-18 15:12:02	7.67×10^{5}	2015-09-20 17:36:02	1.97×10^{5}	2d2h24m0s
12422	M 7.6	2015-09-25 21:00:01	4.73×10^{5}	2015-09-28 14:48:01	3.24×10^{5}	2d17h48m0s
12423	M 3.6	2015-09-27 06:12:01	1.76×10^{6}	2015-09-28 03:48:01	4.65×10^{5}	0d21h36m0s
	M 1.2	2015-09-27 06:12:01	1.76×10^{6}	2015-09-29 03:12:01	1.86×10^{5}	1d21h0m0s
	M 1.2	2015-09-27 06:12:01	1.76×10^{6}	2015-09-29 05:36:01	7.08×10^{4}	1d23h24m0s
	M 1.3	2015-09-27 06:12:01	1.76×10^{6}	2015-09-29 08:48:01	2.39×10^{5}	2d2h36m0s
12434	M 1.1	2015-10-13 06:47:59	8.08×10^{6}	2015-10-15 23:23:59	2.76×10^{5}	2d16h36m0s
	M 1.1	2015-10-13 06:47:59	8.08×10^{6}	2015-10-16 06:11:59	3.83×10^{4}	2d23h24m0s
12437	M 1.5	2015-10-17 16:23:58	7.35×10^{6}	2015-10-17 20:35:58	4.38×10^{5}	0d4h12m0s
12443	M 3.7	2015-10-31 22:23:56	3.68×10^{5}	2015-11-04 13:35:56	1.76×10^{5}	3d15h12m0s
12445	M 2.5	2015-11-04 01:23:56	1.05×10^{6}	2015-11-04 11:59:56	3.81×10^{5}	0d10h36m0s
12449	M 3.9	2015-11-08 13:59:55	8.49×10^{6}	2015-11-09 12:47:55	3.07×10^{4}	0d22h48m0s
12473	M 1.6	2015-12-21 08:47:52	1.84×10^{6}	2015-12-22 03:11:52	3.65×10^{4}	0d18h24m0s
	M 4.7	2015-12-21 08:47:52	1.84×10^{6}	2015-12-23 00:23:52	9.11×10^{4}	1d15h36m0s
	M 1.1	2015-12-21 08:47:52	1.84×10^{6}	2015-12-24 01:47:52	4.15×10^{5}	2d17h0m0s
12497	M 1.0	2016-02-12 09:11:54	4.32×10^{5}	2016-02-12 10:35:54	3.95×10^{5}	0d1h24m0s
	M 1.8	2016-02-13 04:47:54	1.11×10^{6}	2016-02-13 15:11:54	2.71×10^{6}	0d10h24m0s
	M 1.0	2016-02-14 03:35:54	1.90×10^{7}	2016-02-14 19:23:54	1.01×10^{6}	0d15h48m0s
	M 1.1	2016-02-14 03:35:54	1.90×10^{7}	2016-02-15 10:35:54	1.67×10^{6}	1d7h0m0s
12529	M 6.7	2016-04-15 04:48:02	6.75×10^{5}	2016-04-18 00:12:02	3.49×10^{5}	2d19h24m0s
12567	M 7.6	2016-07-22 15:12:08	5.36×10^{5}	2016-07-23 05:00:08	4.01×10^{5}	0d13h48m0s
12644	M 5.3	2017-04-02 05:59:00	2.36×10^{5}	2017-04-02 07:47:00	1.77×10^{5}	0d1h48m0s
	M 5.7	2017-04-02 16:35:00	2.52×10^{5}	2017-04-02 20:23:00	1.33×10^{5}	0d3h48m0s
	M 5.8	2017-04-03 01:23:00	7.11×10^{5}	2017-04-03 14:23:00	3.81×10^{5}	0d13h0m0s
12665	M 1.3	2017-07-06 15:36:08	2.60×10^{6}	2017-07-09 03:12:08	5.30×10^{5}	2d11h36m0s
12673	X 2.2	2017-09-05 21:12:04	2.50×10^{6}	2017-09-06 09:00:04	1.91×10^{6}	0d11h48m0s
	X 9.3	2017-09-05 21:12:04	2.50×10^{6}	2017-09-06 11:48:04	1.10×10^{6}	0d14h36m0s
	X 1.3	2017-09-05 21:12:04	2.50×10^{6}	2017-09-07 14:24:04	8.42×10^{5}	1d17h12m0s
	X 8.2	2017-09-10 01:24:04	3.27×10^{6}	2017-09-10 11:12:03	3.53×10^{5}	0d9h47m59s
12696	B 9.7	2018-01-16 10:11:52	3.34×10^{5}	2018-01-18 07:23:52	1.23×10^{5}	1d21h12m0s
	B 9.5	2018-01-16 10:11:52	3.34×10^{5}	2018-01-22 02:35:52	2.79×10^{4}	5d16h24m0s

12699	C 8.1	2018-02-04 11:47:53	1.09×10^{6}	2018-02-07 13:35:53	2.49×10^{5}	3d1h48m0s
12700	C 1.9	2018-02-28 22:35:55	3.45×10^{6}	2018-03-02 10:59:56	6.26×10^{4}	1d12h24m1s
12703	B 9.0	2018-03-29 18:23:00	1.01×10^{6}	2018-04-01 12:47:00	5.35×10^{4}	2d18h24m0s
12704	B 1.0	2018-04-12 18:48:01	1.98×10^{5}	2018-04-14 00:12:01	5.63×10^{4}	1d5h24m0s
12710	B 9.8	2018-05-21 07:00:06	2.40×10^{5}	2018-05-24 12:24:06	5.15×10^{4}	3d5h24m0s
12712	C 2.7	2018-05-24 20:00:06	1.16×10^{6}	2018-05-28 17:00:07	1.19×10^{5}	3d21h0m1s
12713	B 4.7	2018-06-23 13:00:08	5.98×10^{5}	2018-06-23 14:36:08	3.30×10^{5}	0d1h36m0s
12714	B 1.0	2018-06-19 01:48:08	1.49×10^{5}	2018-06-19 02:24:08	1.08×10^{5}	0d0h36m0s
	B 1.8	2018-06-19 15:24:08	2.71×10^{5}	2018-06-20 00:00:08	1.78×10^{5}	0d8h36m0s
12715	C 2.1	2018-06-20 04:12:08	3.72×10^{5}	2018-06-21 01:12:08	4.03×10^{5}	0d21h0m0s
12719	B 1.6	2018-08-23 03:12:06	1.94×10^{6}	2018-08-24 21:48:05	9.49×10^{4}	1d18h35m59s
12729	B 2.4	2018-12-09 03:47:53	1.06×10^{6}	2018-12-09 06:59:53	1.61×10^{5}	0d3h12m0s
12732	C 1.6	2019-01-06 06:11:52	6.85×10^{6}	2019-01-06 10:35:52	3.59×10^{5}	0d4h24m0s
12733	C 5.0	2019-01-24 01:47:52	2.61×10^{5}	2019-01-26 13:11:52	1.61×10^{5}	2d11h24m0s
12734	C 1.3	2019-03-06 10:23:56	4.98×10^{5}	2019-03-08 03:11:56	1.00×10^{5}	1d16h48m0s
12736	C 4.8	2019-03-19 19:23:58	6.27×10^{5}	2019-03-20 10:35:58	2.05×10^{5}	0d15h12m0s
	C 5.6	2019-03-19 19:23:58	6.27×10^{5}	2019-03-21 03:11:58	3.11×10^{5}	1d7h48m0s
12738	B 7.1	2019-04-10 19:00:01	4.20×10^{5}	2019-04-12 11:24:01	1.18×10^{5}	1d16h24m0s
	B 8.1	2019-04-18 04:48:02	7.54×10^{6}	2019-04-20 00:24:02	3.23×10^{4}	1d19h36m0s
12740	C 9.9	2019-05-04 04:36:04	3.36×10^{6}	2019-05-06 05:00:04	4.03×10^{5}	2d0h24m0s
	C 6.7	2019-05-04 04:36:04	3.36×10^{6}	2019-05-09 05:36:05	1.68×10^{5}	5d1h0m1s
12741	C 2.0	2019-05-07 15:12:04	6.29×10^{6}	2019-05-15 19:12:05	2.91×10^{5}	8d4h0m1s

References

Benz, A. O. (2002). *Plasma Astrophysics: Kinetic Processes in Solar and Stellar Coronae*. Astrophysics and Space Science Library. Springer Netherlands.

Benz, A. O. (2008). Flare observations. *Living Reviews in Solar Physics*, 5(1).

Chamberlin, P., Pesnell, W. D., and Thompson, B. (2012). *The Solar Dynamics Observatory*. Springer-Verlag New York.

Chaplin, W. J. . (2006). *The Music of the Sun : The Story of Helioseismology*. Oxford : Oneworld.

Collins Petersen, C. (2017). *Astronomy 101: from the sun and moon to wormholes and warp drive, key theories, discoveries, and facts about the universe*. Adams Media, Avon, MA, USA.

Cravens, T. E. (1997). *Physics of Solar System Plasmas*. Cambridge Atmospheric and Space Science Series. Cambridge University Press.

Dikpati, M., de Toma, G., and Gilman, P. A. (2006). Predicting the strength of solar cycle 24 using a flux-transport dynamo-based tool. *Geophysical Research Letters*, 33(5).

Erdelyi, R., Korsos, M. B., Huang, X., Yang, Y., Pizzey, D., Wrathmall, S. A., Hughes, I., Dyer, M., Dhillon, V. S., Belucz, B., Brajsa, R., Chatterjee, P., Cheng, X., Deng, Y., Dominguez, S. V., Joya, R., Gomory, P., Gyenge, N. G., Hanslmeier, A., Kucera, A., Kuridze, D., Li, F., Liu, Z., Long, X., Mathioudakis, M., Matthews, S., McAteer, J. R., Pevtsov, A. A., Potzi, W., Romano, P., Shen, J., Temesvary, J., Tlatov, A. G., Triana, C., Utz, D., Veronig, A. M., Wang, Y., Yan, Y., Zaqarashvili, T., and Zuccarello, F. (2021). The solar activity monitor network - samnet. *Journal of Space Weather and Space Climate*.

Garfinkle, D. and Garfinkle, R. (2008). *Three Steps to the Universe: From the Sun to Black Holes to the Mystery of Dark Matter*. University of Chicago Press.

Glogowski, K., Bobra, M. G., Choudhary, N., Amezcua, A. B., and Mumford, S. J. (2019). drms: A python package for accessing hmi and aia data. *Journal of Open Source Software*, 4(40):1614.

Granados Hernández, N. (2019). Análisis de centroides de polaridad magnética en regiones solares activas. Master's thesis, Universidad Nacional de Colombia, Bogotá,Colombia.

Granados-Hernández, N. and Vargas-Domínguez, S. (2020). Análisis de polaridades magnéticas en regiones activas para la predicción de fulguraciones solares. *Rev. Acad. Colomb. Cienc. Ex. Fis. Nat.*, 44(173):984–995.

Hanslmeier, A. (2008). *The Sun and Space Weather*. Astrophysics and Space Science Library. Springer, 2nd edition.

HARP (1997). Harps - hmi active region patches. http://jsoc.stanford.edu/HMI/HARPS.html.

Hill, F., Martens, P., Yoshimura, K., Gurman, J., Hourclé, J., Dimitoglou, G., Suárez-Solá, I., Wampler, S., Reardon, K., Davey, A., Richard, B., and Tian, K. (2009). The virtual solar observatory—a resource for international heliophysics research. *Earth, Moon, and Planets*, 104:315–330.

Howell, E. (2018). Solar dynamics observatory: Staring at the sun. https://www.space.com/22081-solar-dynamics-observatory.html.

Joya, R., Domínguez, S. V., Sánchez, C. T. J., and Calia, D. B. (2020). Nodo colombiano para la red internacional de monitoreo de actividad solar. *Revista Innovación y Ciencia.*, XXVII(4).

JSOC (1997). Joint science operations center. http://jsoc.stanford.edu/.

Karttunen, H., Kröger, P., Oja, H., Poutanen, M., and Donner, K. J. (2017). *Fundamental Astronomy*. Springer-Verlag Berlin Heidelberg, 6 edition.

Kenneth R, L. (2006). *Sun, Eart and Sky*. Springer, Medford, MA, USA.

Knipp, D. J., Fraser, B. J., Shea, M. A., and Smart, D. F. (2018). On the little-known consequences of the 4 august 1972 ultra-fast coronal mass ejecta: Facts, commentary, and call to action. *Space Weather*, 16(11):1635–1643.

Korsós, M. B., Baranyi, T., and Ludmány, A. (2014). PRE-FLARE DYNAMICS OF SUNSPOT GROUPS. *The Astrophysical Journal*, 789(2):107.

Korsós, M. B., Ludmány, A., Erdélyi, R., and Baranyi, T. (2015). ON FLARE PREDICTABILITY BASED ON SUNSPOT GROUP EVOLUTION. *The Astrophysical Journal*, 802(2):L21.

Korsós, M. B., Yang, S., and Erdelyi, R. (2019). Investigation of pre-flare dynamics using the weighted horizontal magnetic gradient method: From small to major flare classes. *Journal of Space Weather and Space Climate*.

Moore, P. (2005). *Philip's Encyclopedia of Astronomy*. Prentice Hall Inc., 1 edition.

Murdin, P. (2001). *Encyclopedia Of Astronomy & Astrophysics*. Nature Publishing Group.

Phillips, T. (2014). Near miss: The solar superstorm of july 2012. https://science.nasa.gov/science-news/science-at-nasa/2014/23jul_superstorm/.

Schrijver, C.J.and Zwaan, C. (2000). *Solar and Stellar Magnetic Activity*. Cambridge Astrophysics. Cambridge University Press.

Severino, G. (2017). *The Structure and Evolution of the Sun*. Undergraduate Lecture Notes in Physics. Springer International Publishing, 1 edition.

van Allen, J. A. (1983). *Origins of magnetospheric physics*.

Vaquero J.M., V. M. (2009). *The Sun Recorded Through History Authors*. Astrophysics and Space Science Library. Springer-Verlag New York.

Volker Bothmer, I. A. D. (2007). *Space Weather: Physics and Effects*. Environmental Sciences. Springer-Verlag Berlin Heidelberg.